e-ISSN : 2776-2521

JOCPES

Journal of Computation Physics and Earth Science

Volume 6 No. 1
April, 2026

Email:
adm.jocpes@gmail.com
admin@physan.org

https://journal.physan.org/index.php/jocpes

Journal of Computation Physics and Earth Science
ISSN: 2776-2521 (online)
Volume 6, Number 1, April 2026, Page 1 - 6
https://journal.physan.org/index.php/jocpes/index

Case Study of MEMS-Based Earthquake Early Warning With P-ALERT System: A Literature Review

Ahmad Aqila Nubala[1], Muhammad Yazid Ilmany[2], Wyra Steven Hutagalung[3]
[1,2]Undergraduate Program in Applied of Instrumentation Meteorology, Climatology Geophysics (STMKG)
[3]Undergraduate Program in Applied Geophysics (STMKG)

Article Info

Article history:

Received December 30, 2025
Revised January 12, 2026
Accepted March 8, 2026

Keywords:

Earthquake early warning system
MEMS sensors
P-ALERT
Low-cost earthquake early warning system

A B S T R A C T

Earthquakes pose significant threats to infrastructure and human life, emphasizing the urgent need for effective Earthquake Early Warning Systems (EEWS). Traditional EEWS are often expensive and inaccessible for many earthquake-prone regions. This paper explores the potential of low-cost EEWS utilizing Micro-Electro-Mechanical Systems (MEMS), focusing on the P-ALERT system developed in Taiwan. Through a literature review, this study analyzes the architecture, performance, limitations, and prospects of MEMS-based EEWS. The findings highlight that P-ALERT, with its affordability, dense sensor network, and rapid response capability, offers a promising solution for localized and regional earthquake warnings. Despite limitations such as lower data quality compared to high-end seismometers and reliance on stable infrastructure, P-ALERT has demonstrated effectiveness during several major earthquakes. This review also provides recommendations for enhancing the system's performance through decentralized processing, improved sensor algorithms, and strengthened network security. Ultimately, this research underscores the viability of low-cost EEWS like P-ALERT as scalable and inclusive tools for seismic risk mitigation, particularly in developing countries.

Corresponden Author:

Ahmad Aqila Nubala,
Undergraduate Program in Applied of Instrumentation Meteorology, Climatology Geophysics (STMKG)
Tangerang, Indonesia
Email: ahmadaqilanubala@gmail.com

1. INTRODUCTION

Earthquakes are natural disasters that often cause significant damage, ranging from infrastructure destruction to loss of human lives. The substantial losses caused by earthquakes have driven the need for effective early warning systems. Earthquake Early Warning Systems (EEWS) aim to provide alerts to the public before the main seismic shaking occurs, allowing them to take mitigation actions to reduce the negative impact. These early warnings are highly valuable as they can provide several seconds to minutes of lead time before strong ground shaking is felt, depending on the distance between the earthquake source and the warning recipients [1].

The development of micro-electro-mechanical systems (MEMS) technology has paved the way for the creation of low-cost EEWS. MEMS sensors, which are small, lightweight, and energy-efficient, enable the construction of dense and widely distributed sensor networks. Such dense sensor networks are crucial for detecting P-waves (primary waves), which arrive before the more damaging S-waves (secondary waves). By detecting P-waves, the system can estimate the earthquake's magnitude and location, and subsequently issue early warnings. Another advantage of MEMS technology is its relatively low production cost, making the implementation of more affordable EEWS feasible, especially in developing countries vulnerable to earthquakes [2].

P-ALERT (Portable Alert) system is a concrete example of a low-cost MEMS-based EEWS. P-ALERT utilizes MEMS accelerometer sensors to detect ground motion caused by earthquakes. Data from these sensors are processed using specialized algorithms to estimate earthquake parameters such as magnitude and distance. Based on these estimations, the system sends early warnings through various communication channels, such as text messages or mobile applications. The advantages of P-ALERT include ease of installation, affordability, and the ability to provide fast and accurate early warnings [3].

A case study of P-ALERT is essential to convey the effectiveness and transparency of this system across various earthquake scenarios. The analysis includes performance metrics in earthquake detection, the characterization of earthquake parameters, and the issuance of early warnings. Additionally, the case study will consider factors such as detection range, response time, and false alarm rate. The primary goal of this case study is to provide a comprehensive understanding of the potential and limitations of P-ALERT as a low-cost EEWS solution and to offer recommendations for system improvement and future development.

2. LITERATURE REVIEW

2.1. Low-Cost Earthquake Early Warning System

EEWS are designed to provide advance alerts several seconds before the arrival of strong ground shaking, allowing people to take protective actions and enabling automated systems to initiate safety measures. However, traditional EEWS can be expensive to implement, often costing hundreds of millions of dollars, making them inaccessible in many at-risk regions [4]. This has driven the development of low-cost EEWS, which utilize affordable sensors and cloud computing to detect earthquakes and issue warnings in near real-time. These systems often employ MEMS-based sensors, which are significantly cheaper than traditional seismometers, enabling the deployment of denser sensor networks. Increased sensor density allows for more accurate event localization, reduces false positives, and shortens the time required to issue warnings—thus providing people with more critical seconds to react.

The effectiveness of low-cost EEWS has been demonstrated in various regions. The P-ALERT system in Taiwan has been operational for nearly a decade, providing both regional and on-site warnings, as well as generating valuable shaking maps [5]. These shaking maps, which visualize the distribution of ground motion parameters, are crucial for assessing damage patterns and rupture directivity, and they support risk mitigation efforts. The MyShake application, developed by the Berkeley Seismology Lab at UC Berkeley, uses smartphone accelerometers to create a global seismic detection network that issues automatic warnings for earthquakes of magnitude 4.5 or greater. Google's Android Earthquake Alerts System utilizes the accelerometers in Android devices to detect earthquakes and issue warnings, demonstrating the potential of crowdsourced EEWS.

2.2. P-ALERT System

The P-ALERT system is a low-cost, MEMS-based EEWS developed by National Taiwan University (NTU) in collaboration with a technology company. It is designed for both on-site and regional EEWS applications, providing crucial seconds of warning before the onset of strong ground shaking. The system uses small, cost-effective, and easily deployable MEMS sensors, making it suitable for dense deployment in seismically active areas. These sensors record high-frequency ground motion data near the earthquake source, which is then processed to estimate earthquake parameters such as magnitude and potential shaking intensity. P-ALERT is especially effective for on-site warnings, offering lead times of several seconds within the "blind zones" of regional warning systems—areas where alerts from the Central Weather Bureau (CWB) may not be available. The system also generates real-time shaking maps, which are extremely useful for damage assessment and understanding rupture directivity [6].

The performance of the P-ALERT system has been validated during several damaging earthquakes in Taiwan, including the 2016 Meinong earthquake and the 2018 Hualien earthquake. During the Dapu earthquake (2025), the P-ALERT system produced a shaking map within 36 seconds of the event, highlighting areas of intense shaking and assisting in damage evaluation. The system's ability to provide rapid warnings and detailed shaking maps makes it a valuable tool for disaster mitigation and emergency response. The success of the P-ALERT system has led to its adoption in several countries around the world, including China, India, and New Zealand, either as a standalone EEWS or integrated into existing networks. Its dual capability for on-site and regional alerts, combined with its cost-effectiveness, makes it a significant advancement in earthquake early warning technology.

3. RESEARCH METHOD

This research methodology will primarily employ a literature review approach to comprehensively analyze existing knowledge and studies related to low-cost EEWS, with a particular focus on MEMS-based sensors and the P-ALERT system. The initial stage will involve a systematic search of academic databases such as IEEE Xplore, ScienceDirect, Google Scholar, and others, using relevant keywords including "earthquake early warning", "MEMS sensors", "P-ALERT", "low-cost EEWS", "performance analysis", and "literature review". The search will be refined by applying inclusion and exclusion criteria to ensure the relevance and quality of the selected studies. Inclusion criteria will prioritize peer-reviewed journal articles, conference papers, and technical reports published within the past 10 years (2015–2025) to capture recent advancements. Exclusion criteria will filter out studies that are not directly related to the research objective, such as those focusing solely on seismic hazard assessment or earthquake prediction.

The next phase will involve detailed analysis and synthesis of the selected literature. This will include extracting key information from each study—such as system architecture, sensor characteristics, data processing algorithms, performance metrics (e.g., alert time, accuracy, reliability), cost analysis, and limitations. Extracted data will be organized and categorized to facilitate comparative analysis, allowing for the identification of trends, gaps, and potential areas for improvement in the context of low-cost EEWS. The analysis will specifically focus on the P-ALERT system, examining its design, implementation, and performance, and comparing it with other MEMS-based EEWS. The findings will be synthesized to provide a comprehensive understanding of the current state of the field, identifying key challenges and opportunities, and potentially proposing recommendations for future research and development. This literature review will serve as a solid foundation for understanding the effectiveness and limitations of low-cost EEWS, particularly those based on MEMS technology, and how the P-ALERT system performs in comparison to other systems [9].

4. RESULT AND DISCUSSION

4.1. Potential and Limitations of P-ALERT as a Low-Cost Earthquake Early Warning Systems Solution

P-ALERT holds significant potential due to its lower cost compared to traditional seismic instruments, enabling the deployment of denser sensor networks. Such density allows P-ALERT to provide early warnings in areas close to the earthquake source—referred to as the "blind zone" of larger regional EEWS like those operated by Taiwan's Central Weather Bureau (CWB). The dense network also contributes to the generation of real-time shakemaps, which are crucial for damage assessment and emergency response efforts. P-ALERT has proven effective in delivering early warnings during damaging earthquakes in Taiwan, such as the 2016 Meinong earthquake and the 2018 Hualien earthquake. However, P-ALERT also faces several limitations. One major constraint is the limited dynamic range and data quality of MEMS sensors compared to high-grade seismic instruments. This can affect the accuracy of magnitude and location estimations, which in turn may impact the reliability of early warnings. Furthermore, despite the system's dense network, earthquake location and magnitude estimations can still be affected by errors in source localization and seismic wave propagation. Another limitation is the system's dependence on existing infrastructure, such as reliable power supplies and stable internet connections, which can pose challenges in certain regions. Nonetheless, P-ALERT continues to be improved, with newer versions addressing several issues identified in earlier deployments [7].

False alarms represent an additional concern. Since P-ALERT relies on threshold-based algorithms to detect earthquakes, there is a risk that the system might issue warnings even when the shaking is not hazardous. This could lead to alert fatigue and a decline in public trust in the system. Moreover, network security is a growing concern, especially in community-based networks, where the potential for cyberattacks could disrupt system operations.

4.2. Recommendations for the Improvement and Development of Low-Cost Earthquake Early Warning Systems

The development of low-cost Earthquake Early Warning System presents significant opportunities to enhance earthquake preparedness, especially in regions with limited resources. One of the key areas for improvement lies in the system architecture. Decentralized or edge-level processing, where data is processed at the sensor node level rather than at a central hub, can greatly reduce system latency, enhance redundancy, and lower implementation costs. This approach has been highlighted as a promising paradigm for real-time Internet of Things (IoT) applications, addressing critical challenges related to response time, bandwidth usage, and security. The integration of Software-Defined Wide Area Network (SD-WAN) solutions can further improve connectivity and network reliability, especially in community-based sensor networks, where sensors may be deployed in diverse and potentially unstable networking environments.

Another important advancement area lies in sensor technology and algorithm optimization. The integration of multisensor capabilities—allowing for the use of multiple types of MEMS-based sensors—can support denser and more resilient sensor networks. This approach also encourages community engagement by enabling individuals to contribute their own ground motion sensors to the network. Implementing ground-motion or wavefield-based EEW algorithms, which have shown promise in overcoming the limitations of source-based algorithms, can enable faster and more reliable alerts, particularly for regions located near the earthquake epicenter. The use of ground motion parameters such as Cumulative Absolute Absement (CAA) has also demonstrated potential for producing more stable magnitude estimations [10].

Addressing challenges associated with community-based EEW systems is also essential. Network security remains a critical concern, and robust measures are required to prevent spoofing and malicious attacks. This includes securing communication channels between sensors and processing units, as well as implementing authentication mechanisms to ensure data integrity. Finally, sensor density is a vital factor in the performance of regional EEW systems. Increasing the number of sensors can reduce detection time and improve the accuracy of alerts, ultimately enhancing public safety and emergency response capabilities [11].

4.3. Comparative Analysis of Low-Cost Earthquake Early Warning Systems

A comparative analysis of selected low-cost Earthquake Early Warning Systems (EEWS) is presented in Table 1. Each system represents different approaches to cost-efficiency, sensor type, and alert dissemination strategies.

P-ALERT, developed in Taiwan, uses MEMS accelerometers deployed in both regional and on-site configurations. It has demonstrated high responsiveness and effective real-time shakemap generation during significant seismic events such as the 2016 Meinong and 2025 Dapu earthquakes [12], [13].

In contrast, MyShake is a smartphone-based EEWS relying on crowdsourced data. Developed by the Berkeley Seismology Lab, it has proven capable of detecting M≥5 earthquakes in real time, though its performance is dependent on active user participation and mobile network coverage [3], [15].

Google EEWS, integrated directly into Android OS, represents a passive but globally scalable solution. While it ensures broad access without user installation, it lacks the capacity for shakemap generation or intensity mapping [15].

ASTUTI (Costa Rica) adopts an MEMS + IoT-based approach for rural areas with limited infrastructure. It is designed to be highly affordable and easily maintained, while still offering reliable regional alerts [6].

China's GL-P2B and SIT-S system leverages a hybrid model of MEMS and broadband seismometers, resulting in a dense network capable of detecting even small earthquakes (M>3.0) and generating shakemaps with high spatial resolution [8].

These findings illustrate the trade-offs between physical sensor networks and smartphone-based systems, with decisions on deployment depending on the target region's infrastructure, population density, and hazard profile. Countries like Indonesia, with both urban clusters and rural islands, may benefit from hybrid systems combining multiple approaches.

Table 1. Key Features of Selected Low-Cost Earthquake Early Warning Systems

System / Country	Sensor Type	Deployment Mode	Lead Time	Real-Time Shakemap	Key Feature / Highlight
P-ALERT / Taiwan	MEMS Accelerometer	On-site & Regional	4–8 s	Yes	Efficient on-site & regional alerts; detailed shakemaps within 2 minutes ([13])
MyShake / USA	Smartphone Accelerometer	Crowdsourced (App-based)	5–20 s	No	Real-time M≥5 wave detection; depends on user density ([3], [15])
Google EEWS / Global	Smartphone Accelerometer	OS-integrated (Android)	~10 s	No	Global coverage; passive alerts embedded in Android OS ([15])

4.4. Challenges and Future Directions

Despite the promising potential of MEMS-based Earthquake Early Warning Systems (EEWS) such as P-ALERT, several technical and implementation challenges remain. One of the primary limitations lies in the accuracy and reliability of MEMS accelerometers, especially under strong-motion scenarios where high-grade broadband sensors outperform low-cost units in dynamic range and sensitivity [16]. This discrepancy can lead to either false positives or underestimation of seismic intensity.

In addition, network connectivity and latency are critical issues, particularly in rural or disaster-prone areas with unstable power supply and limited communication infrastructure. Systems such as P-ALERT, which rely on rapid data relay, are vulnerable to these disruptions, potentially reducing lead time and warning effectiveness [13].

Another major concern is standardization and interoperability. With growing interest in community-based EEWS using diverse MEMS platforms, ensuring consistent data formats, calibration standards, and response protocols across different regions remains a challenge [8].

Future research directions:

- Integration of machine learning algorithms to reduce false alarms and improve real-time magnitude estimation [17].
- Development of multi-hazard early warning frameworks, combining EEWS with tsunami and landslide alert systems [18].
- Exploration of hybrid sensor networks, combining MEMS and broadband instruments.
- Cost-effectiveness assessments in varying socioeconomic contexts [6].

4.5. Potential of P-ALERT-Like EEWS in Indonesia

Indonesia, situated along the Pacific Ring of Fire, experiences frequent tectonic activity with a high risk of destructive earthquakes. Despite the presence of a national seismic network operated by BMKG, many regions—particularly remote or urban centers—remain vulnerable due to limited local lead time [14].

Drawing from Taiwan's P-ALERT success, Indonesia could replicate a similar model in high-risk zones such as:

- Yogyakarta (Opak fault)
- Padang (Sumatra subduction zone)
- Palu (strike-slip system)

According to Hong et al. [11], MEMS-based technology is increasingly feasible in the Asian context. Allen et al. [3] also stress the scalability of mobile- or IoT-based EEWS in budget-limited regions.

Collaborative deployment through BMKG–Government partnerships could enable SeisComP3-based community EEWS integration, inspired by Costa Rica's ASTUTI network.

5. CONCLUSION

This literature-based study concludes that MEMS-based Earthquake Early Warning Systems (EEWS), such as the P-ALERT system, offer a compelling solution to seismic risk mitigation—particularly for developing countries with budgetary and infrastructure constraints. Compared to traditional EEWS, MEMS-based systems significantly reduce cost barriers while enabling high-density sensor networks capable of real-time shakemap generation and on-site warning delivery.

The analysis highlights that among existing low-cost EEWS, P-ALERT demonstrates superior performance in terms of deployment scalability, dual-mode alert capability, and field-proven effectiveness during major earthquakes. When compared to systems like MyShake, Google EEWS, and ASTUTI, P-ALERT's combination of affordability and physical sensor reliability makes it highly suitable for both urban and rural seismic risk contexts.

In the Indonesian context, the adoption of a P-ALERT-like system presents a strategic opportunity to expand early warning coverage across vulnerable regions—especially those beyond the reach of centralized seismic networks. With its low cost, ease of installation, and capacity for community-based deployment, MEMS EEWS can fill critical gaps in national disaster preparedness efforts.

Furthermore, this review underscores the urgent need to address technical challenges such as sensor calibration, data quality, network latency, and cyber resilience. Future studies should explore integration with IoT and mobile platforms, hybrid sensor models, and algorithmic optimization—particularly using machine learning—to enhance alert precision and lead time.

Ultimately, the findings of this review provide a strong academic foundation for national policy, public investment, and cross-sector collaboration aimed at building inclusive, data-driven, and resilient earthquake early warning infrastructure in Indonesia and other seismically active regions.

REFERENCE

[1] M. Adhikari, D. Paton, D. Johnston, R. Prasanna, and S. T. McColl, "Modelling predictors of earthquake hazard preparedness in Nepal," Procedia Engineering, vol. 212, pp. 910–917, 2018, doi: 10.1016/j.proeng.2018.01.117.

[2] N. Algiriyage, R. Prasanna, K. Stock, E. E. H. Doyle, and D. Johnston, "Multi-source multimodal data and deep learning for disaster response: A systematic review," SN Computer Science, vol. 3, no. 1, p. 92, 2022, doi: 10.1007/s42979-021-00971-4.

[3] R. M. Allen, Q. Kong, and R. Martin-Short, "The MyShake platform: A global vision for earthquake early warning," Pure and Applied Geophysics, vol. 177, no. 4, pp. 1699–1712, 2020, doi: 10.1007/s00024-019-02337-7.

[4] J. S. Becker et al., "Scoping the potential for earthquake early warning in Aotearoa New Zealand: A sectoral analysis of perceived benefits and challenges," International Journal of Disaster Risk Reduction, vol. 51, p.

101765, 2020, doi: 10.1016/j.ijdrr.2020.101765.

[5] R. Bossu, F. Finazzi, R. Steed, L. Fallou, and I. Bondár, "'Shaking in 5 Seconds!'—Performance and user appreciation assessment of the Earthquake Network smartphone−based public earthquake early warning system," *Seismological Research Letters*, vol. 93, no. 1, pp. 137–148, 2021, doi: 10.1785/0220210180.

[6] B. A. Brooks et al., "Robust earthquake early warning at a fraction of the cost: ASTUTI Costa Rica," AGU Advances, vol. 2, no. 3, p. e2021AV000407, 2021, doi: 10.1029/2021av000407.

[7] V. Cascone, J. Boaga, and G. Cassiani, "Small local earthquake detection using low−cost MEMS accelerometers: Examples in northern and central Italy," Seismic Record, vol. 1, no. 1, pp. 20–26, 2021, doi: 10.1785/0320210007.

[8] C. Chandrakumar, R. Prasanna, M. Stephens, and M. L. Tan, "Earthquake early warning systems based on low-cost ground motion sensors: A systematic literature review," *Frontiers in Sensors*, vol. 3, p. 1020202, 2022, doi: 10.3389/fsens.2022.1020202.

[9] E. S. Cochran et al., "Event detection performance of the PLUM earthquake early warning algorithm in southern California," Bulletin of the Seismological Society of America, vol. 109, no. 4, pp. 1524–1541, 2019, doi: 10.1785/0120180326.

[10] F. Franchi, A. Marotta, C. Rinaldi, F. Graziosi, and L. D'Errico, "IoT-based disaster management system on 5G uRLLC network," in Proc. 2019 Int. Conf. on Information and Communication Technologies for Disaster Management (ICT-DM), pp. 1–4, doi: 10.1109/ICT-DM47966.2019.9032897.

[11] H. Hong, L. Ni, and H. Sun, "Application and prospect of MEMS technology to geophysics," in Proc. 16th IEEE Int. Conf. on Nano/Micro Engineered and Molecular Systems (NEMS), 2021, pp. 1863–1866, doi: 10.1109/NEMS51815.2021.9451455.

[12] Y.-M. Wu, Y.-H. Lin, B.-M. Yang, et al., "Performance of the P-alert real-time shakemaps system and onsite warning during the 2025 ML6.4 Dapu earthquake," *Terrestrial, Atmospheric and Oceanic Sciences*, vol. 36, no. 3, 2025, doi: 10.1007/s44195-025-00086-w.

[13] Y.-M. Wu, W.-T. Liang, H. Mittal, W.-A. Chao, C.-H. Lin, B.-S. Huang, and C.-M. Lin, "Performance of a low-cost earthquake early warning system (P-Alert) during the 2016 ML 6.4 Meinong (Taiwan) earthquake," *Seismological Research Letters*, vol. 87, no. 5, pp. 1050–1059, 2016, doi: 10.1785/0220160058.

[14] Y.-M. Wu and H. Mittal, "A review on the development of earthquake warning system using low-cost sensors in Taiwan," Sensors, vol. 21, no. 22, p. 7649, Nov. 2021, doi: 10.3390/s21227649.

[15] S. C. Patel and R. M. Allen, "The MyShake App: User experience of early warning delivery and earthquake shaking," Seismol. Res. Lett., vol. 93, no. 6, pp. 3324–3336, Nov. 2022, doi: 10.1785/0220220062.

[16] J. Clinton et al., "Low-cost sensors for earthquake early warning systems: Challenges and perspectives," Seismol. Res. Lett., vol. 90, no. 1, pp. 20–31, 2019, doi: 10.1785/0220180192.

[17] M. Kühnlenz, J. Reilly, and R. M. Allen, "Using machine learning to improve earthquake early warning systems," Sensors, vol. 21, no. 15, p. 5093, 2021, doi: 10.3390/s21155093.

[18] S. Alam et al., "Multi-hazard early warning systems for effective disaster risk reduction," Int. J. Disaster Risk Reduct., vol. 60, p. 102267, 2021, doi: 10.1016/j.ijdrr.2021.102267.

Journal of Computation Physics and Earth Science
ISSN: 2776-2521 (online)
Volume 6, Number 1, April 2026, Page 7 - 13
https://journal.physan.org/index.php/jocpes/index

Epicenter and Hypocenter Determination Using the Grid Search Method for the 5 August 2018 Lombok Earthquake

Qisthi Mursyida[1]
[1]College of Meteorology, Climatology, and Geophysics

Article Info

Article history:

Received December 30, 2025
Revised January 15, 2026
Accepted March 10, 2026

Keywords:

Grid search method
Lombok earthquake 2018
Epicenter
Hypocenter
P-wave arrival time
RMS misfit

A B S T R A C T

The Lombok Island region is characterized by complex tectonic interactions associated with the subduction of the Indo-Australian Plate beneath the Sunda Plate and the activity of th Flores Back Arc Thrust, resulting in frequent moderate to large earthquakes. One of the most significant events in this region is the Mw 7.0 Lombok earthquake that occurred on 5 August 2018. Accurate determination of the earthquake epicenter and hypocenter is essential for understanding the source characteristics and regional seismotectonic setting. Grid search method was applied to determine the epicenter and hypocenter of the 5 August 2018 Lombok earthquake using P-wave arrival time data revorded by 15 accelerometer. The method evaluates a 3D spatial grid by calculating thereotical travel times based on a homogeneous P-wave velocity model and minimizing the MRS residual between observed and calculated arrivals, yielding a best fit location at latitude −8.2483°, longitude 116.5566°, focal depth of 39.00 km, and a minimum RMS of 1.0064 . Comparison with the BMKG earthquake catalog shows good agreement in apicenter location and focal depth, while RMS based analyses indicate that the earthquake location is well constrained both horizontally and vertically.

Corresponden Author:

Qisthi Mursyida,
College of Meteorology, Climatology, and Geophysics
Tangerang, Indonesia
Email: mursyidaq@gmail.com

1. INTRODUCTION

Indonesia is one of the most seismically active countries in the world due to its complex tectonic setting. The Indonesian archipelago is located at the convergence of three major tectonic plates, Eurasian Plate, Indo-Australian Plate, and the Pacific Plate. This tectonic interaction places Indonesia within the circum Pacific seismic belt, commonly referred to as the Ring of Fire, which is characterized by intense seismic and volcanic activity [1]. The relative motion of these plates generates various tectonic structures, including subduction zones, crustal fault systems, and back-arc thrust, which significantly increase the occurrence of destructive earthquakes throughout the region.

One of the regions strongly affected by this tectonic interaction is the Lesser Sunda Islands, including Lombok Island. Seismicity in this area is primarily controlled by the northward subduction of the Indo-Australian Plate beneath the Sunda Plate along the Sunda Trench, as well as the activity of the Flores Back-Arc Thrust located to the north of Lombok. This tectonic configuration has produced frequent moderate to large earthquakes, including the Lombok earthquake sequence in 2018, which resulted in severve damage and significant societal impacts [2].

The mainshock that occured on 5 August 2018 (Mw 7.0) represents one of the most significant seismic events in the Lombok earthquake sequence. Accurate determination of the epicenter and hypocenter of this earthquake is crucial of understanding the earthquake source mechanism, fault geometry, and regional seismotectonic characteristics. Hypocenter location plays a fundamental role in distinguishing whether an earthquake is associated with subduction processes, shallow crustal faulting, or back-arc thrust activity [3].

Various method have been developed to determine earthquake epicenter and hypocenter locations, ranging from linearized inversion techniques to probabilistic and nonlinear approaches. In tectonically complex regions such as Indonesia, however, the reliability of conventional linearized methods is often reduced due to strong lateral velocity heterogeneity, uneven seismic station distribution, and uncertainties in seismic phase arrival times [4]. These factors may lead to biased solutions and poorly constrained hypocentral depths, particularly for earthquake occuring in offshore or back-arc settings.

An alternative approach to overcome these limitations is the grid search method, which is a direct forward-modelling technique that systematically evaluates a predefined 3d spatial grid. For each grid node, theoretical travel times are calculated using an assumed velocity model and compared with observed arrival times, and the optimal earthquake location is determined by minimizing a misfit function, commonly expressed as the root mean square (RMS) or travel time residuals [5]. Unlike linearized inversion methods, the grid search approach does not require an initial starting model and is less susceptible to convergence toward local minima, making it particularly suitable for regions with complex tectonic settings and limited station coverage. In this study, the grid search method is applied to determine the epicenter and hypocenter of the Mw 7.0 Lombok earthquake that occurred on 5 August 2018. By systematically exploring the spatial distribution of RMS misfit values, this approach allows for a robust assessment of location uncertainty.

2. RESEARCH METHOD

This study uses seismic data recorded by 15 accelerometer stations distributed around Lombok Island and its surrounding regions, covering a geographic area approximately bounded by longitude 112.5°–120.5°E and latitude 9.7°–5.0°S. The distribution of the accelerometer stations, including their geographic coordinates and arrival time, is summarized in Tabel 1. The dataset corresponds to the mainshock of the Lombok earthquake sequence that occurred on 5 August 2018 (Mw 7.0). The accelerometer records provide high quality waveform data suitable for precise arrival time analysis, particularly for strong ground motion events. P-wave arrival times were obtained through an automatic picking (autopicking) process applied to the recorded waveforms. To ensure the reliability of the arrival time data, the autopicking results were subsequently subjected to a quality control (QC) procedure conducted by the researchers. This QC process involved visual inspection any correction of the picked P-wave onsets to minimize picking errors and to ensure consistency across all stations. Only P-wave arrivals that satisfied the quality criteria were included in the subsequent location analysis.

Table 1. Location of seismic stations and p-wave arrival times

Stasiun	Longitude	Latitude	Phase	*Arrival Time* (UTC)
BMNI	118.69269	-8.5427	P	11:47:12
DEBI	115.179	-8.738	P	11:47:00
DEMO	115.18	-8.74	P	11:47:00
ITSU	112.795715	-7.280119	P	11:47:37
JAGI	114.153261	-8.470653	P	11:47:12
JBJN	113.7174	-8.15565	P	11:47:19
LABA	119.886	-8.4866	P	11:47:28
MAKO	112.5975	-7.90112	P	11:47:35
NEKI	114.6174	-8.3408	P	11:47:05
PLAI	117.7765	-8.8273	P	11:47:00
RMNN	120.47801	-8.59793	P	11:47:36
SUBE	117.4135	-8.4879	P	11:46:53
SUHA	119.5449	-5.0589	P	11:47:41
TRES	112.6891	-7.664	P	11:47:34
WGNI	120.2976	-9.6692	P	11:47:36

The epicenter and hypocenter of the earthquake were determined using the grid search method, which is a forward modelling approach that systematically evaluates potential source locations within a predfined spatial grid. A 3d grid was constructed covering the study area, including horizontal coordinates and depth. For each grid node, theoretical P-wave travel times were calculated using a constant P-wave velocity model [6].

At each grid point with coordinates (X_0, Y_0, Z_0), the model P-wave arrival time (t_{model}) was calculated based on the geometric distance between the grid node and each seismic station, assuming a homogeneous velocity structure. The midel arrival time is expressed as:

$$t_{model} = t_0 + \frac{\sqrt{(X_0 - X_i)^2 + (Y_0 - Y_i)^2 + Z_0^2}}{V_p} \tag{1}$$

where X_i and Y_i represent the horizontal coordinates of the i-th station, Z_0^2 is the depth of the grid node, and V_p is the P-wave velocity. The origin time t_0 was estimated at each grid node as the average difference between the observed arrival times (t_{obs}) and the calculated travel times (t_{cal}).

The misfit between observed and theoretical arrival times was quantified using the RMS residual, defined as:

$$RMS = \sqrt{\frac{1}{N}\sum_{i=1}^{N}(t_i^{obs} - t_i^{cal})^2} \quad (2)$$

where t_i^{obs} and t_i^{cal} are the observed and calculated P-wave arrival times at the i-th station, respectively, and N is the total number of stations. The grid node corresponding to the minimum RMS value was selected as the best fit epicenter and hypocenter location. Compared to conventional inversion based methods, the grid search approach is not prone to convergence toward local minima and provides a more complete representation of the misfit landscape.

All data processing and analysis in this study were performed using Python. The procedur of the grid search method employed in this study is summarized in the flowchart sown in Figure 1. The workflow begins with the input of seismic waveform data and the definition of 3d spatial grid covering the study area. For each grid node, theoretical P-wave travel times are calculated and the RMS misfit between observed and calculated arrival times is evaluated. This process is repeated iteratively for all grid nodes to ensure exhaustive exploration of the model space. Once all grid points have been evaluated, the grid node associated with the minimum RMS value is selected as the best fit epicenter and hypocenter location. Finally, the distribution of RMS values is analyzed to assess the uncertainty and robustness of the obtained solution.

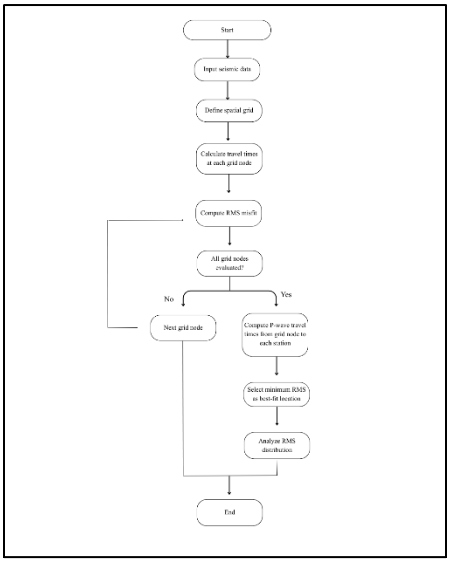

Fig. 1 Flowchart of the grid search method

3. RESEARCH METHOD

3.1. Earthquake Location Resultes and Validation

The epicenter location of the earthquake was determined using the grid search method based on P-wave arrival times recorded by 15 accelerometer stations. The grid search analuysis resulted in a best fit earthquake location with geographic coordinates:

a. Latitude : -8.2483
b. Longitude : 116.5566
c. Depth : 39.00 km
d. RMS : 1.0064

To evaluate the realibility of the obtained earthquake location, the grid search results were compared with the earthquake catalog by Indonesian Agency of Meteorology, Climatology, and Geophysics (BMKG), accessed through the WebDC BMKG platform. The comparison between the epicenter coordinates and focal depth derived in this study and those reported in the BMKG catalog in Table 2.

Table 2. Comparison of earthquake location parameters obtained from the grid search method and the BMKG catalog (WebDC BMKG)

Parameter	Grid Search Result	BMKG Catalog (WebDC)
Latitude (°)	-8.2483	-8.35
Longitude (°)	116.5566	116.47
Depth (km)	39.00	32.4

The comparison between the earthquake location parameters obtained from the grid search method and those reported in the BMKG catalog (WebDC BMKG), as presented in Table 2, shows a generally good agreement in both epicenter location and focal depth. The latitude difference between the two solutions is approximately 0.10°, while the longitude by about 0.09°. These relatively small horizontal discrepancies indicate that the epicenter location derived from the grid search method is spatially consistent with the BMKG catalog.

In terms of focal depth, the grid search result indicates a depth of 39.00 km, whereas the BMKG catalog reports a depth of 32.4 km, resulting in a depth difference of approximately 6.6 km. This discrepancy may be attributed to differences in the velocity model, phase selection, and earthquake location algorithms employed by each method. The grid search approach adopted in this study utilized a simplified and homogeneous P-wave velocity model, while the BMKG catalog using more complex operational procedures and potentially incorporates additional seismic phases. This depth difference remains within an acceptable range, considering that the depth value reported in the BMKG catalog is based on a fixed depth assumption, wich inherently limis the resolution od source deoth variations. Despite these differences, the RMS residual value of 1.0064 obtained from the grid search analysis suggest that the calculated arrival times reasonably fi the observed P-wave data.

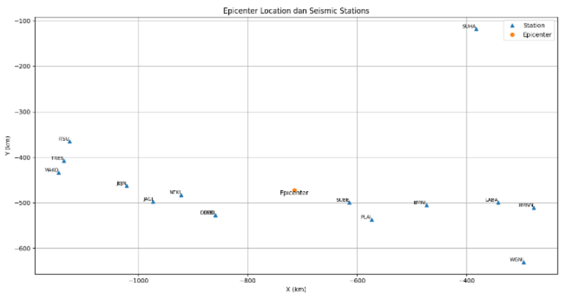

Fig. 2 Distribution of seismic stations and epicenter location

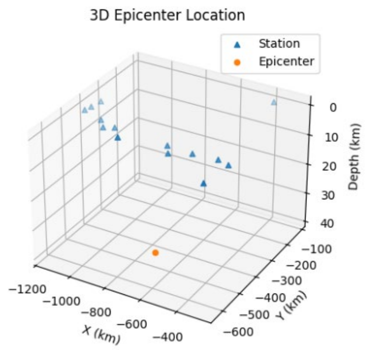

Fig. 3 3D epicenter location

Figure 2 illustrates the horizontal distribution of the 15 accelerometer stations used in this study along with the epicenter location obtained from the grid earch method. The epicenter is located within the coverage of the seismic network, indicating that the station geometry provides sufficient azimuthal control for constraining the earthquake location. This relatively uniform spatial distribution of stations surrounding the epicenter contributes to the small horizontal discrepancies observed in the comparison with the BMKG catalog. This station configuration supports the reliability of the grid search result, particularly in determining the epicenter location, and is consistent with low RMS residual obtained from the arrival time misfit analysis.

The 3d representation of the earthquake source location obtained from the grid search analysis is shown in Figure 3. The figure illustrated the spatial relationship between the seismic station distribution and the estimated hypocenter, with the focal depth located at approximately 39 km beneath the surface network. The 3d visualization provides insight into the vertical geometry of the solution, indicating that the hypocenter is reasonably constrained within the depth range supported by the available P-wave arrival time data.

3.2. RMS Spatial Distribution and Misfit Surface

The RMS heatmap derived from the grid search analysis at the optimal focal depth of 39 km is shown in Figure 4. The heatmap highlights a low RMS region that is elongated in the horizontal direction and centered near the estimated epicenter, indicating that this depth provides the most favorable math between observed and calculated P-wave arrival times. The gradual increase in RMS values away from the low RMS region suggest a smooth spatial variation of the misfit function, implying that horizontal perturbations in the source location lead to systematic changes in RMS values rather than abrupt fluctuations.

The 3d misfit surface derived from the grid search analysis is illustrated in Figure 5. The surface displays a pronounced low RMS region centered near the optimal epicenter location, while RMS values increase gradually away from this region. This smooth variation of RMS values indicates that the misfit function changes continuously with spatial position, suggesting a stable solution rather than one controlled by spurious or isolated local minima. Although the misfit surface exhibits asymmetry in certain directions, the presence of a dominant minimum supports the robustness of the estimated epicenter location.

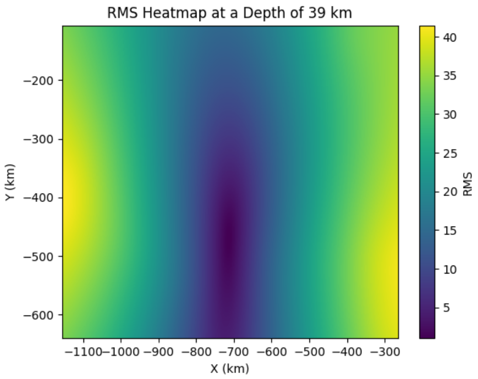

Fig. 4 RMS heatmap at a depth (39 km)

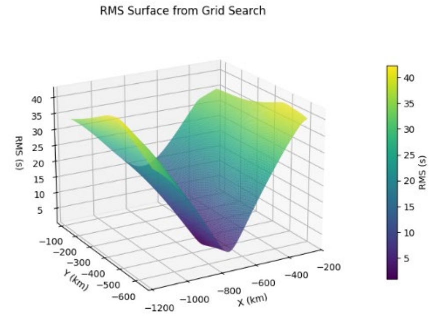

Fig. 5 RMS surface from grid search

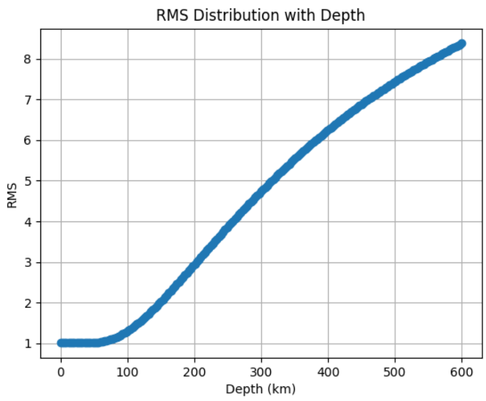

Fig. 6 RMS distribution with depth

The variation of RMS values as a function of depth derived from the grid search analysis is shown in Figure 6. The RMS curve indicates a minimum RMS value at a depth of approximately 39 km, which corresponds to the optimal hypocenter depth obtained in this study. At shallower depths, the RMS values remain relatively low but begin to increase gradually with increasing depth, reflecting a progressive reduction in the fit between observed and calculated P-wave arrival times.

3.3. Seismic Wave Path

The seismic wave paths from the accelerometer stations to the estimated hypocenter derived from the grid search analysis are illustrated in Figure 7. The wave paths were computed assuming a homogeneous P-wave velocity model and represent the theoretical first arrival propagation from the earthquake source to each recording station. The convergence of the wave paths toward the hypocenter indicates that the observed P-wave arrival times recorded at different stations can be consistently explained by a single source location. The variation in ray path orientations reflect the azimuthal distribution of the stations surrounding the epicenter, which contributes to reducing location ambiguity and improving the geometric constraint of the hypocenter.

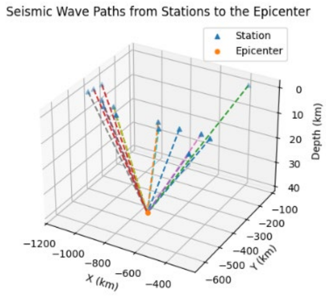

Fig. 7 Seismic wave paths from stations to the Hypocenter

3.3. Travel Time Residual

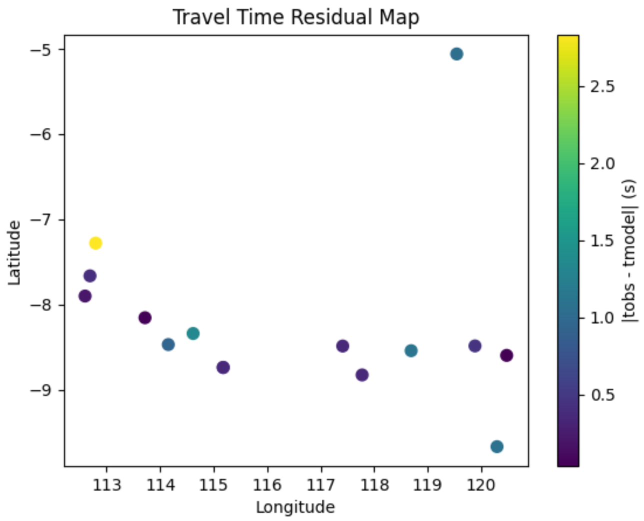

Fig. 8 Travel time residual map

The spatial distribution of P-wave travel time residuals between observed and calculated arrival times is shown in Figure 8. The residual map displays the absolute differences [t_obs- t_model] at each seismic station, represented by color intensity. Most stations exhibit relativel small residual values, generally less than approximately 2 s, indicating a good overall agreement between the observed P-wave arrivals and the travel times predicted by the grid search. A small number of stations show comparatively larger residuals, which are spatially isolated and do not form a systematic pattern across the network. These localized residual variations may be associated with a local site effects, lateral heterogeneities in the crust, or uncertainties in arrival time picking.

4. CONCLUSION

This study applied the grid search method to determine the epicenter and hypocenter of the Mw 7.0 Lombok earthquake that occurred on 5 August 2018 using P-wave arrival time data recorded by 15 accelerometer stations. The grid search analysis yielded a best fit earthquake location at latitude −8.2483°, longitude 116.5566°, a focal depth at 39.00 km, amd a minimum RMS residual of 1.0064 s, indicating a satisfactory fit between observed and calculated arrival times. Comparison with the BMKG catalog shows a generally good agreement in both epicenter location and focal depth. The horizontal discrepancies are relatively small, while the depth difference of approximately 6.6 km remains within an acceptable range, considering that the BMKG catalog employs a fixed depth assumption. Analysis or RMS spatial distributin, 3D misfit surfaces, and RMS variation with depth indicates that the earthquake location is well constrained both horizontally and vertically. The presence of a dominant minimum in the misfit function, together with the smooth variation of RMS values, suggest that the obtained solution is stable and not influenced by spurious local minima. Overall, the results confirm that the grid search method is an effective and robust approach for earthquake location analysis in tectonically complex regions such as Lombok Island.

REFERENCE

[1] S. J. Hutchings and W. D. Mooney, “The Seismicity of Indonesia and Tectonic Implications Geochemistry, Geophysics, Geosystems,” pp. 1–42, 2021, doi: 10.1029/2021GC009812.

[2] H. Afif et al., “Local earthquake tomography of the source region of the 2018 Lombok earthquake sequence , Indonesia,” pp. 1814–1823, 2021.

[3] P. M. Shearer, “Improving local earthquake locations using the L1 norm and waveform cross correlation: Application to the Whittier aftershock sequence Narrows California,” vol. 102, no. 134, pp. 8269–8283, 1997.

[4] S. Husen, E. Kissling, N. Deichmann, S. Wiemer, D. Giardini, and M. Baer, “Probabilistic earthquake location in complex 3d velocity models : Application to Switzerland,” vol. 108, no. February, 2003, doi: 10.1029/2002JB001778.

[5] H. Gökalp, “Estimation of Hypocentral Paremeters of Local / regional Earthquakes by Grid Search Method With a Fuzzy Logic Approach,” pp. 0–42, 2024.

[6] H. Nugroho, S. Widiyantoro, and A. D. Nugraha, “Hypocenter Relocation using a Fast Grid Search Method and a 3-D Seismic Velocity Model for the Sumatra Region,” vol. 293, no. 2013, pp. 10–14, 2015, doi: 10.1063/1.4820343.

Journal of Computation Physics and Earth Science
ISSN: 2776-2521 (online)
Volume 6, Number 1, April 2026, Page 14 - 21
https://journal.physan.org/index.php/jocpes/index

Modulation of the Indian Ocean Dipole on Regional Atmospheric Circulation Variability over the Indonesian Maritime Continent (IMC) across Various ENSO Phases (1991–2020)

Chikal Pratama Putra[1], Rizki Wahyu Arifin[2], Sayful Amri[3]
[1,2,3]Indonesia State College of Meteorology, Climatology, and Geophysics

Article Info

Article history:

Received March 19, 2026
Revised March 25, 2026
Accepted March 27, 2026

Keywords:

IMC
ENSO
Dipole Mode
Dynamics

A B S T R A C T

This study investigates the modulation mechanisms of the Dipole Mode on the impact of ENSO toward the atmospheric dynamics of the Indonesian Maritime Continent (IMC). Utilizing ERA5 reanalysis and Multi-Source Weather (MSWX) data for the 1991–2020 period, a conditional composite method was applied to 12 climate interaction scenarios. The results indicate that in-phase interactions exhibit constructive interference. The combination of Strong El Niño and Positive DMI triggers massive divergence, leading to "double drought" conditions, whereas Strong La Niña and Negative DMI result in extreme precipitation. A crucial finding confirms the Dipole Mode as a vital modulator. Negative DMI is shown to act as a buffer that mitigates El Niño-induced drought in western Indonesia, while Positive DMI dominantly suppresses La Niña's wet signals. Understanding these mechanisms is essential for the accuracy of seasonal weather predictions and the mitigation of hydrometeorological disasters.

Corresponden Author:

Rizki Wahyu Arifin,
Indonesia State College of Meteorology, Climatology, and Geophysics
Tangerang, Indonesia
Email: rizkiwahyuarifin@gmail.com

1. INTRODUCTION

As a strategic country situated between the Pacific and Indian Oceans, and between the continents of Asia and Australia, Indonesia possesses an actively dynamic atmosphere across local, regional, and global scales, which significantly impacts rainfall pattern variations [1]. These atmospheric dynamics are shaped by three primary motions: mean flow, waves, and turbulence [2]. Indonesia is categorized as a Maritime Continent, a region characterized by high convective activity [3], often referred to as the Indonesian Maritime Continent (IMC). Due to its geographical position, the IMC exhibits complex weather and climate conditions [4]. The primary factor driving this complexity is the influence of the Asian and Australian monsoons [5]. Additionally, it is influenced by interannual variability, such as the Dipole Mode [6] and El Niño-Southern Oscillation (ENSO) [7], as well as intraseasonal variability like the Madden-Julian Oscillation (MJO) [8] and synoptic disturbances such as equatorial waves [2]. The interaction of regional dynamics with global variability is crucial, as it can trigger extreme hydrometeorological disasters that threaten public safety [9].

The greatest challenge in analyzing atmospheric dynamics in the IMC is the complex interaction when these phenomena occur simultaneously (co-occurrence), which can be either constructive or destructive. Consequently, weather anomalies in a specific region become difficult to predict if only a single factor is considered [10]. Among these various phenomena, wind circulation and rainfall variability in the IMC are dominantly controlled by global Sea Surface Temperature (SST) anomalies as the primary predictors, specifically the Dipole Mode and ENSO [6], [7]. Prioritizing these two phenomena as the main focus is based on their non-linear interactions, where the Dipole Mode has been proven to significantly modulate the strength of the Walker and Hadley circulations triggered by ENSO [2], [11]. This interaction primarily alters regional wind circulation patterns [12], which subsequently impacts changes in rainfall distribution [1], [13]. Although intraseasonal phenomena such as the MJO also contribute [8], the influence of ENSO and IOD operates on a longer temporal scale and exerts a stronger influence on divergence patterns and low-level moisture transport [9]. Therefore, understanding the modulation mechanisms of these two predictors is vital [9], [10].

Given the vast area of the IMC and the limited number of conventional observation stations, remote sensing and reanalysis data serve as primary solutions [12]. The validity of using satellite-based data to capture extreme phenomena was demonstrated by Saragih et al. (2018), who utilized satellite data to observe rainfall and wind distribution patterns during Tropical Cyclones Cempaka and Dahlia. The utilization of high-resolution data, such as Multi-Source Weather (MSWX) and ERA5, has proven capable of representing spatial atmospheric variability with greater precision than single-point observation data, as validated in various agrometeorological and disaster studies in tropical regions [9], [13], [15]. This approach enables a more in-depth analysis of causal relationships, where zonal and meridional wind circulation anomalies are mapped as primary drivers, followed by a spatial analysis of rainfall response [2].

This study aims to determine the response of atmospheric dynamics in the IMC through a composite analysis approach, utilizing ENSO and Dipole Mode indices as predictor variables to observe their impacts on atmospheric dynamics, as indicated by wind circulation and rainfall variability. This systematic approach is expected to clarify the relationship between large-scale circulation disturbances and regional hydrometeorological impacts to support future disaster mitigation efforts [10].

2. RESEARCH METHOD

This research covers the Indonesian Maritime Continent (IMC), bounded by coordinates 90°E – 150°E and 15°S – 15°N. The selection of this domain is based on the characteristics of the IMC as an active convective region that responds to global circulation anomalies [3]. The study spans a 30-year period (January 1991 to December 2020), representing a standard WMO climate normal period, which is representative enough to capture the interannual variability of ENSO and the Dipole Mode [10].

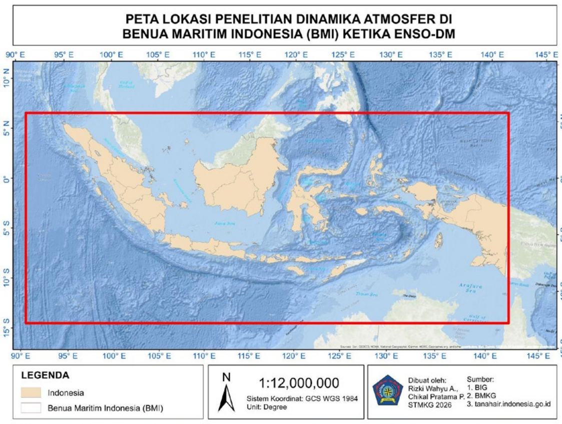

Fig. 1 Study Area Location *(Source: Processed data from the Geospatial Information Agency)*

The data used in this study are secondary gridded datasets, categorized into predictor and predictand variables. The validity of using satellite-based and reanalysis data in tropical regions with sparse conventional observations has been proven effective in previous studies [12], [14].

2.1. Predictor Variables

Predictor variables represent the global-scale climate forcings that drive regional variability:

- Niño 3.4 Index: Used to determine ENSO phases and intensity. Data are sourced from the NOAA Physical Sciences Laboratory, representing Sea Surface Temperature (SST) anomalies in the Central Pacific [7].
- Dipole Mode Index (DMI): Used to determine the phases of the Indian Ocean Dipole (IOD). This index is calculated based on the SST anomaly gradient between the Western and Southeastern Tropical Indian Ocean [6], [11].

2.2. Predictand Variables

Predictand variables represent the atmospheric dynamic responses and hydrometeorological impacts over the IMC:

- Wind Circulation (Dynamics): Zonal (u) and meridional (v) wind components at the 850 hPa pressure level are used to analyze moisture transport patterns and air mass convergence. Data are

sourced from ECMWF Reanalysis v5 (ERA5) with a spatial resolution of 0.25° x 0.25°. ERA5 is considered superior in representing monsoon circulation and atmospheric wave interactions in the tropics [13].
- Precipitation (Impact): Precipitation data are obtained from Multi-Source Weather (MSWX) with a high spatial resolution of 0.1° x 0.1°. This product was selected because it is bias-corrected using global observation stations, providing better accuracy than pure satellite data in mapping rainfall distribution across Indonesia's complex topography [13], [15].

2.3. Software and Tools

- Climate Data Operators (CDO): For processing netCDF data.
- Visual Studio Code: Used for netCDF data processing and generating composite maps using Python 3.10.
- ArcGIS Map 10.8: For creating the study area location map.

2.4. Research Procedures

The method employed is quantitative descriptive analysis with a composite approach. The research stages are as follows:

- Data Collection and Pre-processing: Rainfall (MSWX), wind (ERA5), and climate indices (Niño 3.4 and DMI) for 1991–2020 were downloaded and extracted. Spatial data were then cropped to the IMC boundaries using CDO to optimize computation.
- Anomaly Calculation: The monthly climatological mean (30 years) was calculated for each grid point. Anomaly values were then obtained by subtracting the monthly data from the mean to remove the influence of the seasonal cycle.
- Climate Event Identification: Global index time-series data were categorized based on specific thresholds to determine months falling into the 12 interaction scenarios between ENSO and the Dipole Mode.
- Composite Analysis: An averaging technique was applied to the rainfall and wind data that met the event criteria. The final results are presented as overlay maps to visualize how wind patterns influence rainfall distribution in the IMC.

3. RESULT AND DISCUSSION

3.1. Global Climate Variability Identification

To understand the fluctuations of climate phenomena during the study period, a time-series identification of the Niño 3.4 index and the Dipole Mode Index (DMI) was conducted. The historical visualization of these two indices is presented in Figure 2.

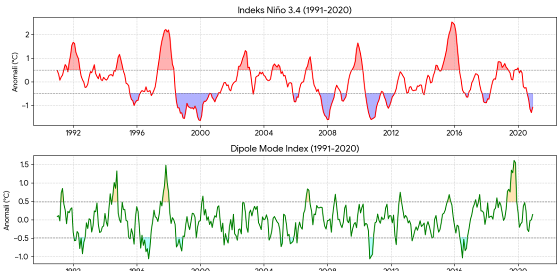

Fig. 2 Time series of the Niño 3.4 index (top) and DMI (bottom) for the 1991–2020 period. Shaded areas indicate active anomaly periods exceeding the established thresholds [16], [17].

3.2. Event Classification Criteria

Composite analysis requires the grouping of events based on their intensity. This study classifies ENSO into six active classes (Weak, Moderate, and Strong for both phases) and the DMI into two active classes (Positive and Negative). The threshold criteria used for these classifications are presented in Table 1 and Table 2.

Table 1. ENSO Phase Classification Criteria

Phase	Category	Index Threshold (ºC)
La Niña	Strong	< -1.5ºC
	Moderate	-1.0ºC to -1.5ºC
	Weak	-0.5ºC to -1.0ºC
El Niño	Weak	+0.5ºC to +1.0ºC
	Moderate	+1.0ºC to +1.5ºC

Phase	Category	Index Threshold (ºC)
El Niño	Strong	> +1.5ºC

Source: Processed data from NOAA, 2024 [16]

Table 2. Dipole Mode Phase Classification Criteria

Phase	Category	Index Threshold (ºC)
Positive	IOD (+)	> +0.48ºC
Negative	IOD (-)	< -0.48ºC

Source: Processed data from Saji et al., 1999 [11]

3.3. Distribution of the 12 Interaction Scenarios

Based on the criteria above, the frequency of occurrences for the 12 combinations of active climate interactions was calculated. The distribution matrix of the number of event months (n) is presented in Table 3.

Table 3. Frequency of ENSO and Dipole Mode Interaction Combinations (1991–2020)

ENSO Category	Positive DMI (n)	Negative DMI (n)
Strong El Niño	8	1
Moderate El Niño	5	1
Weak El Niño	11	1
Weak La Niña	3	7
Moderate La Niña	2	7
Strong La Niña	0	5

Source: Processed data

As shown in Table 3, contrasting interaction patterns are evident. Strong El Niño exhibits a high tendency to co-occur with Positive DMI (n=8); this phenomenon is known as constructive interference, which triggers extreme drought [2]. Conversely, Strong La Niña tends to be associated with Negative DMI (n=5), potentially triggering extreme wet conditions. Combinations of opposing phases (e.g., El Niño with Negative DMI) have a very low frequency of occurrence (n=1), yet they represent critical cases for observing circulation modulation effects [10].

3.4. Spatial Composite Analysis

This analysis presents overlay maps of 850 hPa wind vectors and rainfall for key interaction scenarios.

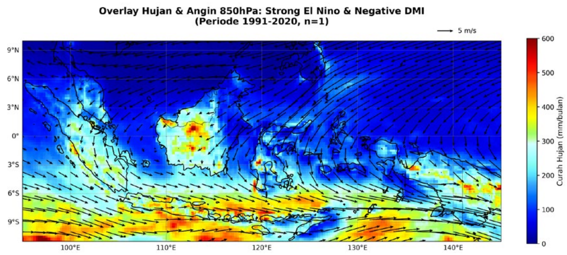

Fig. 3 Overlay Map of Strong El Niño - Negative DMI Configuration

In the Strong El Niño - Negative DMI configuration, the drought intensity typically driven by a strong El Niño is significantly reduced by the wet signal from the negative IOD. Moderate rainfall pockets (200–300 mm/month) are observed persisting along southern regions, including Java, Bali, and Nusa Tenggara. The presence of a Negative DMI triggers westerly wind anomalies south of the equator, transporting moisture from the Indian Ocean and effectively countering the easterly flow from the Pacific. The hypothesized anomaly involves competing forces, where the local warm pool in the eastern Indian Ocean is strong enough to bias the dry Pacific signal, providing natural mitigation against total drought risks.

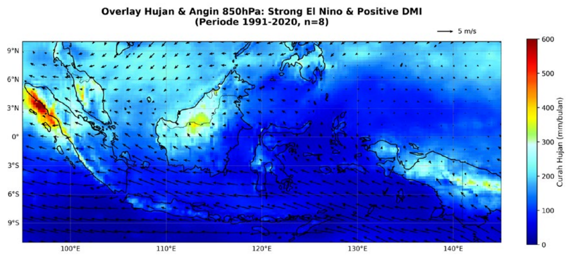

Fig. 4 Overlay Map of Strong El Niño - Positive DMI Configuration

The Strong El Niño - Positive DMI configuration represents an extreme condition that triggers the most severe water deficit anomalies in the dataset. The entire Indonesian Maritime Continent experiences total drought, with rainfall falling below functional ecosystem thresholds (generally <50 mm/month in critical areas). The Walker circulation in both the Pacific and Indian Oceans undergoes a synchronous shift away from Indonesia, creating powerful subsidence (descending air mass). The 850 hPa winds show a highly stable easterly burst, sweeping all moisture toward low-pressure centers in the western Indian Ocean or central Pacific. The hypothesized anomaly is the loss of local variability influence due to the dominance of an overwhelmingly strong large-scale circulation.

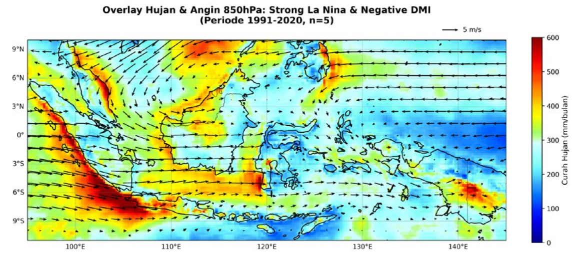

Fig. 5 Overlay Map of Strong La Niña - Negative DMI Configuration

This scenario represents the peak phase of water surplus, often associated with massive hydrometeorological disasters across Indonesia. An overlap occurs between the Pacific warm pool and the warm waters of Western Indonesia, creating intense extra convergence. Rainfall patterns show saturation (red shading, >500 mm/month) across almost all major islands, with very strong westerly anomalies meeting easterly trade winds over the archipelago. The hypothesized anomaly is a massive strengthening of tropospheric humidity up to the upper layers, causing convective clouds to grow deeply and persist throughout the period.

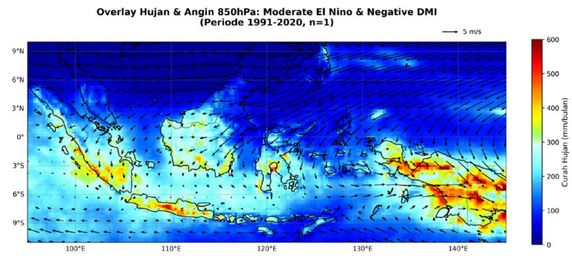

Fig. 6 Overlay Map of Moderate El Niño - Negative DMI Configuration

In this configuration, the drying influence of a moderate El Niño is significantly compensated by the negative IOD. Although low rainfall anomalies occur in central regions, moderate to high rainfall pockets (200–400 mm/month) are still detected, particularly in equatorial regions and Papua. The Negative DMI triggers SST warming in the waters west of Sumatra, dynamically providing additional moisture supply from the eastern Indian Ocean. Circulation analysis at 850 hPa shows that wind patterns are not entirely divergent; instead, westerly anomalies still manage to push moist air masses into the Maritime Continent, ensuring the El Niño drying effect is not absolute and allowing for persistent local rain.

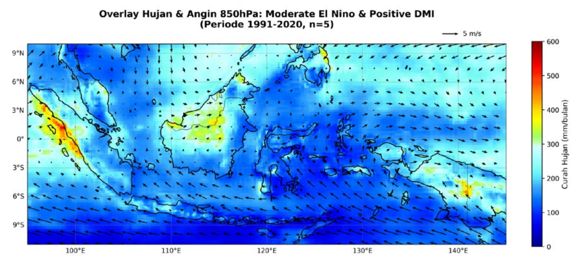

Fig. 7 Overlay Map of Moderate El Niño - Positive DMI Configuration

This scenario represents a dry synergy, where both phenomena work simultaneously to suppress convective activity. A widespread and uniform decrease in rainfall is observed across Indonesia, dominated by dark blue shading (<150 mm/month) covering Sumatra, Java, and Kalimantan. Positive DMI exacerbates dry conditions by cooling SSTs in the eastern Indian Ocean, leading to a drastic weakening of convection. The 850 hPa wind pattern is dominated by strong, divergent easterly flows that mechanically block the formation of convergence zones over the archipelago. Any remaining minor rainfall anomalies are likely products of intraseasonal dynamics (such as the MJO) or strong regional orographic factors, rather than large-scale circulation.

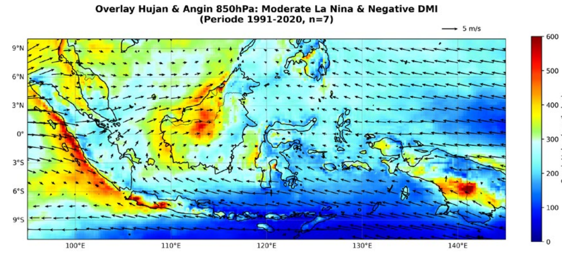

Fig. 8 Overlay Map of Moderate La Niña - Negative DMI Configuration

The combination of Moderate La Niña and Negative DMI creates the most consistent "wet synergy," where Indonesia experiences a significant rainfall increase across nearly all maritime zones. While La Niña enhances convective potential through warm SST anomalies in the Western Pacific, Negative DMI parallelly strengthens the flow of moist air from the Indian Ocean. Visualizations show a broad spectrum of orange to red (>450 mm/month), indicating very high rainfall intensity. The 850 hPa circulation reveals a clear and organized convergence pattern over Indonesia, acting as the primary engine for the massive and sustained lifting of moist air masses.

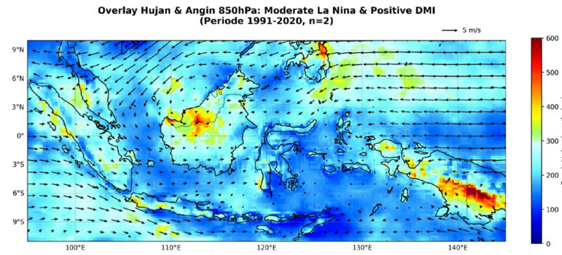

Fig. 9 Overlay Map of Moderate La Niña - Positive DMI Configuration

This condition demonstrates a forced normalization in western Indonesia due to pressure from the positive IOD. Despite an active moderate La Niña, Sumatra and parts of Java show significant rainfall decreases (blue to light green shading). The 850 hPa circulation anomaly shows stable westward wind flow in the Indian Ocean, diverting moisture supply away from the Indonesian coast. The hypothesized anomaly is a shift in regional circulation cells that triggers subsidence in the Eastern Indian Ocean, thereby negating the remote forcing from the Pacific that usually brings abundant rain.

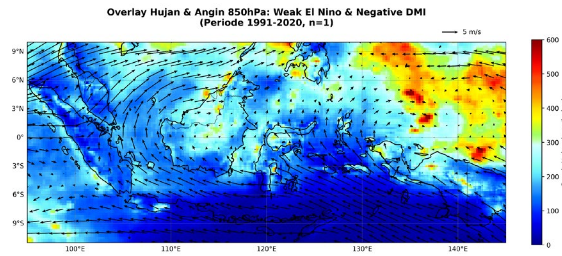

Fig. 10 Overlay Map of Weak El Niño - Negative DMI Configuration

In this configuration, the weak El Niño signal is almost invisible, overwhelmed by the local dominance of the wet-trending negative IOD. The western coast of Sumatra and most of Kalimantan continue to show moderate to high rainfall (green-orange). The 850 hPa wind pattern is dominated by stable westerlies from the Indian Ocean toward the Indonesian landmass. The hypothesized anomaly is that local SST forcing in western Indonesia is far more influential than a weak ENSO signal, maintaining a humid atmosphere that supports daily rainfall in equatorial regions.

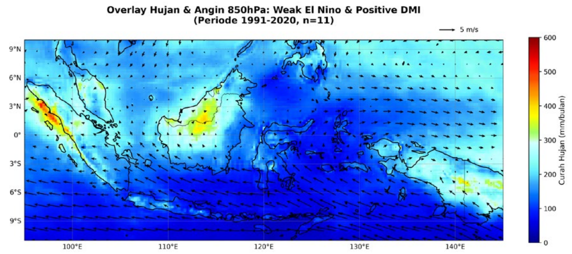

Fig. 11 Overlay Map of Weak El Niño - Positive DMI Configuration

This scenario shows that even a weak El Niño can cause significant drought if accompanied by a Positive DMI. Western Indonesia is dominated by blue shading, indicating uniformly below-normal rainfall. The 850 hPa wind pattern shows fairly consistent easterly flow, though at lower velocities than in strong phases. The hypothesized anomaly suggests that Positive DMI has a low threshold for activating dry conditions in Indonesia, making even a weak El Niño sufficient to trigger widespread water deficits in Sumatra and Kalimantan.

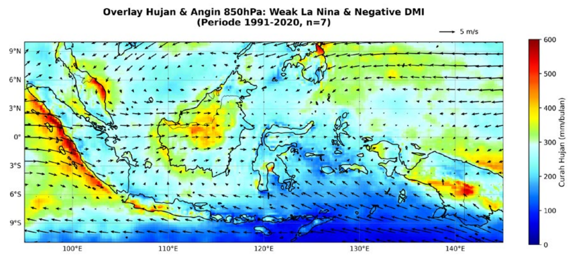

Fig. 12 Overlay Map of Weak La Niña - Negative DMI Configuration

The combination of Weak La Niña and Negative DMI maintains stable wet conditions, especially in coastal and equatorial regions. Rainfall increases appear consistent in northern Sumatra and Papua, with yellow to orange colors dominating the map. Wind analysis at 850 hPa indicates fairly strong local convergence around the Karimata Strait. The hypothesized anomaly is that the interaction of these two phenomena in their weak phases is more influenced by seasonal variability (Monsoon), yet it keeps atmospheric moisture above average, maintaining high rainfall activity.

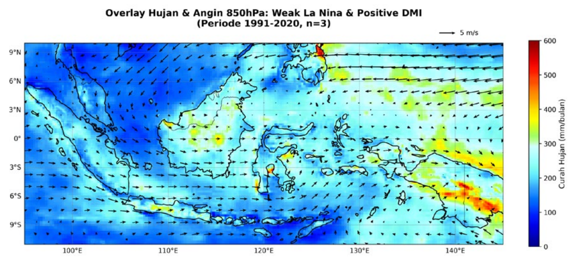

Fig. 13 Overlay Map of Weak La Niña - Positive DMI Configuration

This phenomenon demonstrates that the IOD exerts higher control than a weak ENSO in Western Indonesia. Despite the La Niña (wet) status, the presence of a Positive DMI successfully induces drought in Sumatra and Java. This proves that local forcing from the Indian Ocean can negate remote forcing from the Pacific if ENSO strength is not at a moderate level or higher. The hypothesized anomaly is the inhibition of evaporation in the Eastern Indian Ocean due to cold SST anomalies brought by the positive DMI phase.

4. CONCLUSION

The primary conclusion from the analysis of these 11 ENSO and IOD interaction scenarios confirms that the Indian Ocean Dipole (IOD) plays a more crucial role in determining rainfall variability in Western Indonesia compared to the remote forcing from the Pacific Ocean. The Positive DMI is consistently proven to be a dominant suppressor, capable of neutralizing the wet signals from La Niña phases—particularly at weak to moderate levels—thereby causing significant rainfall deficits across Sumatra and Java. Conversely, the Negative DMI acts as a natural mitigation mechanism (buffer) that reduces the intensity of extreme drought during Strong El Niño events by providing an additional moisture supply from the eastern Indian Ocean.

The interaction between these two phenomena further demonstrates that the influence threshold of a weak ENSO phase is often insufficient to alter Indonesia's regional weather patterns when confronted with an active IOD phase; this indicates that local Sea Surface Temperatures (SST) in Indonesian waters exert more absolute control. In terms of disaster risk, the synergy between Strong La Niña and Negative DMI creates the highest potential hydrometeorological threat through a super-convergence mechanism. Meanwhile, Strong El Niño co-occurring with Positive DMI represents the peak risk configuration for forest and land fires, driven by the total loss of wind convergence zones and a near-complete lack of local evaporation across the Maritime Continent.

REFERENCE

[1] N. Madani, E. Hermawan, and A. Faqih, "Pengembangan Model Prediksi Madden-Julian Oscillation (MJO) Berbasis Hasil Analisis Data Wind Profiler Radar (WPR)," J. Meteorol. dan Geofis., vol. 13, no. 1, 2012.
[2] S. Amri, F. R. Fajary, and T. W. Hadi, "Analysis of Synoptic Disturbance in Maritime Continent Using Spherical Harmonics Transformation Method," Agromet, vol. 34, no. 2, pages 89–99, 2020.
[3] D. Argüeso, R. Romero, and V. Homar, "Precipitation features of the Maritime Continent in parameterized and explicit convection models," J. Clim., vol. 33, no. 6, pages 2449–2466, 2020.
[4] R. M. Putra, S. Alfiandy, and B. E. A. Haq, "Identifikasi Pengaruh El Nino Southern Oscillation (Enso), Indian Ocean Dipole (Iod), And Madden Julian Oscillation (Mjo) Terhadap Intensitas Curah Hujan Bulanan Di Indonesia Berbasis Machine Learning," Bul. Ngurah Rai, vol. 6, pages 1–8, 2020.
[5] J. Slingo, "MONSOONS| Overview," 2003.
[6] Z. Li, W. Yu, K. Li, B. Liu, and G. Wang, "Modulation of interannual variability of tropical cyclone activity over Southeast Indian Ocean by negative IOD phase," Dyn. Atmos. Ocean., vol. 72, pages 62–69, 2015.
[7] M.-S. Ahn, D. Kim, Y.-G. Ham, and S. Park, "Role of Maritime Continent land convection on the mean state and MJO propagation," J. Clim., vol. 33, no. 5, pages 1659–1675, 2020.
[8] S. C. Peatman, J. Schwendike, C. E. Birch, J. H. Marsham, A. J. Matthews, and G.-Y. Yang, "A local-to-large scale view of Maritime Continent rainfall: Control by ENSO, MJO, and equatorial waves," J. Clim., vol. 34, no. 22, pages 8933–8953, 2021.
[9] S. Amri and G. Giarno, "Analisis Dinamika Atmosfer Pada Kejadian Banjir, Tanah Longsor, dan Angin Kencang Di Semarang dan Demak Tanggal 13 Maret 2024," J. Ilm. Biosaintropis, vol. 10, no. 1, pages 77–89, 2024.
[10] M. A. Adzan, R. S. Amanu, P. Kuswanaji, S. Amri, and O. R. A. Saputro, "Analisis Dinamika Atmosfer di Benua Maritim Indonesia saat Fase Aktif CENS dan MJO Selama 30 Tahun (1994-2023)," EL-JUGHRAFIYAH, vol. 5, no. 1, pages 1–12, 2025.
[11] N. H. Saji, B. N. Goswami, P. N. Vinayachandran, and T. Yamagata, "A dipole mode in the tropical Indian Ocean," Nature, vol. 401, no. 6751, pages 360–363, 1999.
[12] B. Munir, "Faktor Atmosfer dalam Visibilitas Hilal Badan Meteorologi Klimatologi dan Geofisika (BMKG)," Lunggi J., vol. 2, no. 4, pages 684–713, 2024.
[13] A. J. Lumbantoruan and S. Amri, "Analisis Pengaruh Intertropical Convergence Zone (ITCZ) dan Fenomena Cuaca Global terhadap Banjir di Kabupaten Wonogiri Tanggal 12 Februari 2023," J. Geosains dan Remote Sens., vol. 6, no. 2, pages 91–98, 2025.
[14] I. J. A. Saragih, P. A. Sigihartato, M. P. Rosyady, and A. Kristianto, "Pemanfaatan Data Penginderaan Jauh untuk Mengamati Perkembangan Siklon Tropis Cempaka dan Dahlia Serta Pengaruhnya Terhadap Distribusi Curah Hujan di Benua Maritim Indonesia," Sinas Inderaja 2018, July, 2018.
[15] H. E. Beck et al., "MSWX: Global 3-hourly 0.1 bias-corrected meteorological data including near-real-time updates and forecast ensembles," Bull. Am. Meteorol. Soc., vol. 103, no. 3, pages E710–E732, 2022.
[16] NOAA, "El Niño/Southern Oscillation," 2025. [Online]. Available: https://www.ncei.noaa.gov/access/monitoring/enso/sst.
[17] Bureau of Meteorology, "Climate monitoring graphs," 2026. [Online]. Available: https://www.bom.gov.au/climate/enso/indices.shtml.

Journal of Computation Physics and Earth Science
ISSN: 2776-2521 (online)
Volume 6, Number 1, April 2026, Page 22 - 32
https://journal.physan.org/index.php/jocpes/index

Optimization of Propulsion and Energy Systems on Remote-Controlled Platform Supply Vessel "Rex Maris"

Nathaniel Slim Reuven[1], Muhammad Ramdhani Setyo Nugroho[2], Yobel Eliezer Mahardika[3], Panji Kuswanaji[4], Anton Widodo[5]
[1, 2, 3]Undergraduate Program in Applied of Instrumentation Meteorology, Climatology, and Geophysics (STMKG)
[4]Undergraduate Program in Applied Meteorology (STMKG)
[5]Program in Applied of Instrumentation Meteorology Climatology and Geophysics (STMKG)

Article Info

Article history:

Received March 29, 2026
Revised March 31, 2026
Accepted April 3, 2026

Keywords:

Ship propulsion,
Propulsive efficiency,
Hull design,
Remote control system,
Monohull

A B S T R A C T

This study optimizes propulsion and energy systems for the remote-controlled Platform Supply Vessel (PSV) prototype Rex Maris (LoA 80 cm), using regression-based principal dimensions and Maxsurf hydrodynamic simulations. Four hull variants yielded a monohull with 15% resistance reduction (Rt = 14.73 N at Vs = 10 m/s) versus initial baseline design, EHP = 147.3 W. Propulsion analysis (ηH = 0.67, ηo = 0.35, ηrr = 1.0) produced Cp = 0.23 and quasi-propulsive efficiency ηp = 0.67-0.70, exceeding conventional PSV benchmarks (0.55-0.65). Energy estimation indicates ~8% consumption reduction (Wh/km basis) under assumed duty cycle, without remote control penalties. This prototype design study addresses gaps in RC-USV optimization for Indonesian offshore logistics, not full-scale validation.

Corresponden Author:

Nathaniel Slim Reuven,
Undergraduate Program in Applied Meteorology Climatology and Geophysics (STMKG)
Tangerang, Indonesia
Email: nathanielreuven@gmail.com

NOMENCLATURE

B	Beam (width)
BHP	Brake Horsepower
Cp	Propulsive coefficient
Cb	Block coefficient
D	Depth
DHP	Delivered Horsepower
DWT	Deadweight Tonnage
EHP	Effective Horsepower
LOA	Length Overall
R^2	Coefficient of determination
Rt	Total resistance
SHP	Shaft Horsepower
T	Draft
Vs	Design speed
w	Wake fraction
t	Thrust deduction factor
ηH	Hull efficiency
ηo	Open water efficiency
ηp	Quasi-propulsive efficiency
ηrr	Relative rotative efficiency

1. INTRODUCTION

Platform Supply Vessels (PSV) play a critical role in offshore oil and gas operations, serving as the primary means of transporting equipment, supplies, and personnel to offshore platforms [1]. The advancement of Electronic Remote Control (ERC) technology has become a national priority for enhancing operational safety and efficiency through reduced direct crew exposure to hazardous offshore environments [2]. Indonesia, as the world's largest archipelagic nation with over 17,000 islands, possesses significant maritime potential that requires innovative technological solutions for optimal resource management [3].

The Rex Maris vessel, designed as a remote-controlled PSV, incorporates ERC technology to perform offshore logistics functions while being operated by skilled personnel from a safe distance [4]. In the context of carbon emission control and operational cost management, vessel energy efficiency has become increasingly crucial [5]. The maritime sector is responsible for approximately 3 percent of global emissions, with International Maritime Organization regulations imposing reduction targets of 20 to 70 percent by 2030 to 2050. A mere 1 percent fuel savings can reduce operational costs by hundreds of thousands of dollars annually for large vessels. Therefore, optimization of hull design and propulsion systems represents a fundamental strategy for improving vessel efficiency [6], [7].

However, most previous research has focused on fully crewed vessels or autonomous systems [8], [9]. This study addresses the research gap by examining the technical design of the remote-controlled Rex Maris support vessel, from hull modeling and propulsion system selection to propulsive efficiency measurement. The objective is to produce a Rex Maris vessel design that is safe, energy-efficient, and remotely operable, consistent with industry trends targeting emission reductions of up to 30 percent while maintaining human oversight and control.

The innovation of this research lies in the integration of monohull technology with electronic remote control systems specifically designed for Indonesian waters [3]. The vessel is equipped with advanced monitoring capabilities for meteorology, climatology, and geophysics applications, extending its functionality beyond conventional supply operations [10], [11], [12]. This multifunctional approach represents a novel contribution to maritime technology development in Indonesia.

This research focuses on the design and optimization stages of a small-scale model ship prototype (total length 80 cm) as proof-of-concept for the application of remote control technology on PSV-type ships. The results obtained (resistance, power, efficiency) are absolute values on this model scale. Extrapolation to full-scale vessels would require appropriate scaling laws (e.g., Froude scaling) and is beyond the scope of this proof-of-concept study.

Table 1. State-of-the-art comparison of recent research on USV, PSV, and unmanned vessel optimization

Author & Year	Vessel Type	Method	Scale	Performance Metric	Novel Contribution
Ghazali et al. (2024) [13]	USV	Review of hull design perspectives	Various	Stability, manoeuvrability, hydrodynamic performance	Comprehensive review of USV hull design constraints and optimization approaches
Xin et al. (2026) [14]	USGV	Hierarchical multi-objective optimization with Voronoi-EHVI adaptive sampling	Model scale	18.3% surface resistance reduction, 7.9% underwater resistance reduction	Novel framework for high-dimensional cross-domain hull design
Guan et al. (2022) [15]	SWATH USV	Hull form optimization with combination evaluations	Model scale	Resistance and seakeeping performance	Integrated optimization considering both resistance and seakeeping
Dong & Liang (2022) [16]	USV fleet	Numerical simulation of formation optimization	Numerical	Minimum energy consumption, formation efficiency	Hydrodynamic optimization strategy for USV formations based on Kelvin wave patterns
Newman et al. (2023) [8]	USV for offshore windfarms	Review and operational analysis	Full-scale	Operational capability	Application of uncrewed vessels throughout windfarm lifespan
Peixoto et al. (2024) [16]	Diesel-electric PSV	Power dispatch optimization with real data	Full-scale	7-12% fuel/CO2 reduction	Validated model using five months of operational data

Author & Year	Vessel Type	Method	Scale	Performance Metric	Novel Contribution
Baital et al. (2021) [6]	General ship	Propulsion efficiency analysis	Model scale	Thrust deduction and wake fraction effects	Influence of draft changes on propulsive parameters
Satpathi et al. (2017) [7]	DC PSV	Real-time scheduling optimization	Full-scale	Fuel consumption reduction	Coordinated generator scheduling with renewable integration
This study	Remote-controlled PSV prototype	Hull optimization (Maxsurf) + energy estimation	Model scale	8% estimated energy reduction	Integration of monohull optimization with remote control system for proof-of-concept

1.1. Ship Resistance and Propulsion Theory

Ship resistance comprises several components including frictional resistance, wave-making resistance, and form resistance [6]. The total resistance determines the power required to propel the vessel at a given speed. The fundamental relationship between resistance and power is expressed through the Effective Horsepower calculation:

$$EHP = Rt \times Vs \tag{1}$$

where Rt represents total resistance in Newtons and Vs represents velocity in meters per second. The propulsive coefficient relates the effective power to the delivered power through the hull efficiency, propeller efficiency, and relative rotative efficiency [18], [7].

1.2. Hull Design Optimization

The optimization of hull form aims to minimize resistance while maintaining adequate stability and seakeeping characteristics [7]. The displacement-to-length ratio, prismatic coefficient, and block coefficient significantly influence vessel performance. For platform supply vessels, the monohull configuration offers advantages in heavy weather operation and cargo capacity [4].

1.3. Propulsion System Components

The propulsion system efficiency depends on the interaction between hull, propeller, and power plant [6], [18]. Key parameters include wake fraction, thrust deduction factor, and relative rotative efficiency. The propulsive coefficient Cp is calculated as:

$$Cp = \eta rr \times \eta o \times \eta H \tag{2}$$

where ηrr represents relative rotative efficiency, ηo represents open water efficiency, and ηH represents hull efficiency. These parameters were calculated using established naval architecture methods adapted for the Rex Maris design [6].

2. RESEARCH METHOD

Fig. 1 Flowchart of the optimization methodology for the hull and propulsion system of the Rex Maris ship

Diagram in Figure 1 shows the complete stages of research, starting from the regression analysis of the reference ship's dimensions, Maxsurf hydrodynamic simulations for four hull variants, selection of the optimal design, to complete propulsion calculations (EHP, DHP, SHP, BHP). Each stage is accompanied by selection criteria and key numerical outputs.

2.1. Design Process

The research commenced with the determination of principal dimensions through regression analysis of reference vessels [2], [4]. Four comparable platform supply vessels were analyzed to establish dimensional relationships. The regression method utilized deadweight tonnage as the independent variable to predict length, beam, depth, and draft. The resulting dimensions for the Rex Maris prototype are presented in Table 2 and Figure 2.

Table 2. Principal Dimensions of Rex Maris

Parameter	Value (cm)
Length Overall (LoA)	80
Beam (B)	22
Depth (D)	8
Draft (T)	5.5

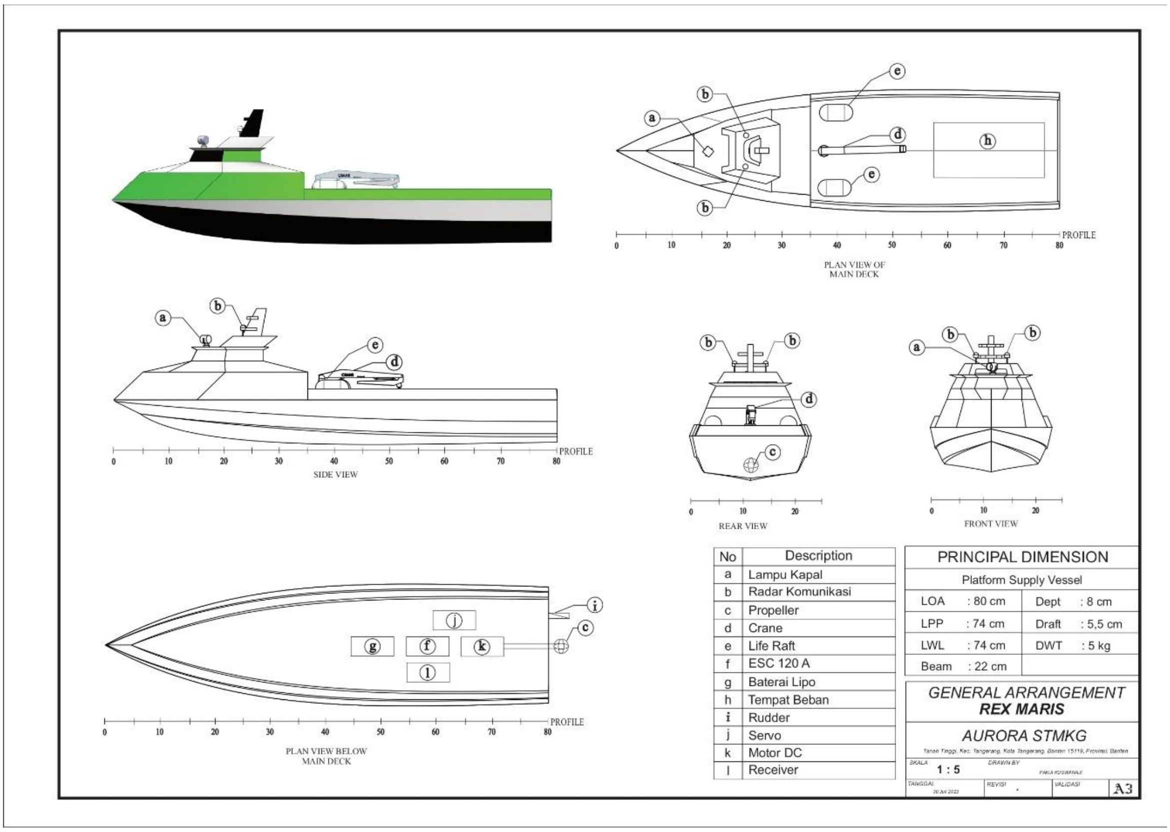

Fig. 2 General Arrangement of Rex Maris

2.2. Hull Form Development

Multiple hull variants were developed using computer-aided design software. Each variant was analyzed using Maxsurf Resistance software employing the Savitsky method [7]. The analysis evaluated resistance, stability, and power requirements across a range of speeds. The hull generating the minimum resistance at the design speed was selected for further development. The lines plan can be seen in Figure 3.

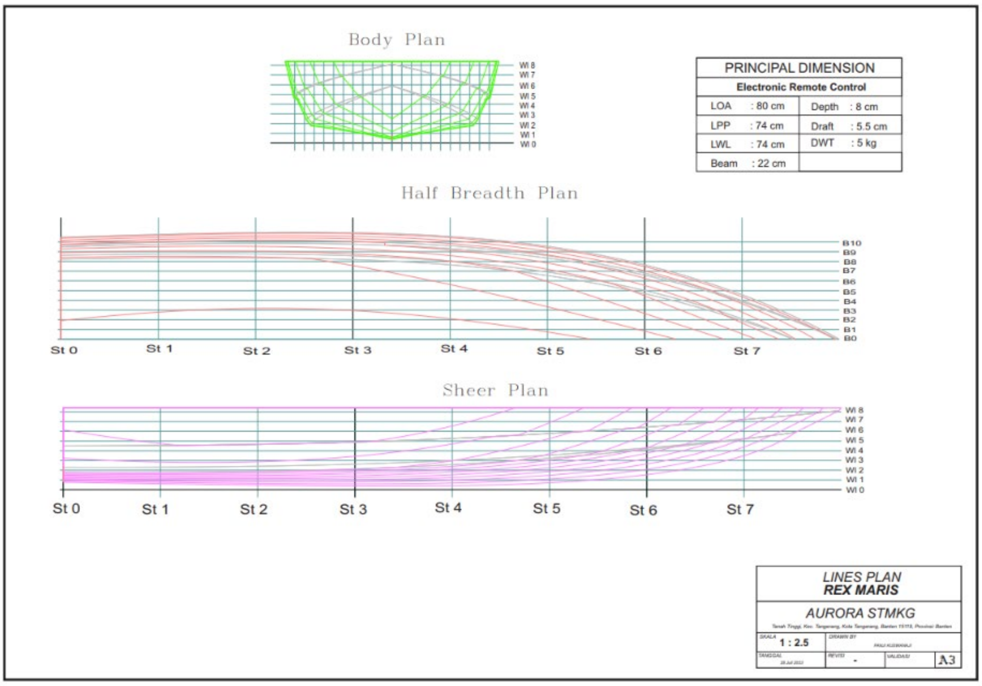

Fig. 3 Rex Maris ship optimal hull lines plan

2.3. Propulsion Calculation

The propulsion calculations followed standard naval architecture procedures [6], [18]. The wake fraction was calculated using the formula:

$$w = 0{,}5 \times Cb - 0{,}05 \tag{3}$$

where Cb represents the block coefficient. The thrust deduction factor was determined as:

$$t = k \times w \tag{4}$$

Based on the hull form characteristics and propulsion analysis, the empirical coefficient k was determined to be 1.07 for this design. This value was derived from the relationship $t = k \times w$ using the calculated wake fraction $w = 0.15$ and thrust deduction factor $t = 0.16$ obtained from the Maxsurf simulations. Hull efficiency was then calculated as:

$$\eta H = \frac{1 - t}{1 - w} \tag{5}$$

These parameters were combined to determine the overall propulsive coefficient and required shaft horsepower [6].

2.4. Component Selection

Electronic and mechanical components were selected based on the calculated power requirements and operational parameters. The propulsion system utilizes a 3665 Supersonic Brushless Motor with specifications of 2200 KV and maximum power of 1400 W. The electronic speed controller rated at 120 A manages motor operation. A 6S Li-Po battery with 2200 mAh capacity provides electrical power. The remote control system operates on 2.4 GHz frequency with 7 channels for comprehensive vessel control.

2.5. Energy Consumption Estimation Method

To quantify the potential energy savings resulting from the optimized hull design, an energy consumption model was developed based on a representative operational profile for platform supply vessels (PSV). This approach follows established methodologies for assessing vessel efficiency improvements [5], [6]. The model incorporates three key elements: operational duty cycle, power–speed relationship, and energy calculation.

A typical PSV mission is divided into three phases based on analysis of real operational data from diesel-electric PSVs [6] and mission profile simulations [19]. The vessel spends approximately 60% of its time in transit or cruise mode at 80% of design speed (Vs), 30% in loiter or station-keeping mode at 40% of Vs (often involving dynamic positioning), and 10% in maneuvering or idle mode at 20% of Vs. This 60/30/10 distribution reflects operational reality where PSVs rarely operate at maximum speed continuously due to mission requirements and fuel efficiency considerations [6], [20]. Propulsion power is known to scale with the cube of speed (P ~ V³) for displacement and semi-planing hulls. Thus, the brake horsepower (BHP) required at any speed V is given by:

$$BHP(V) = BHP_{V_s} \times \left(\frac{V}{V_s}\right)^3 \quad (6)$$

Where BHP_{V_s} is the power required at design speed Vs. Total energy consumption per mission (in watt-hours) is then the sum of the products of BHP and duration for each phase:

$$E_{total} = \sum \left(BHP_{phase} \times t_{phase}\right) \quad (7)$$

The duration of each phase tphase is derived from the duty cycle percentages and a standardised mission distance of 2 km, which is typical for offshore supply runs. Finally, energy consumption per kilometre (Wh/km) is obtained by dividing total energy by distance, allowing direct comparison between design alternatives. This model provides a transparent and traceable basis for estimating the impact of hull optimisation on operational energy use, while acknowledging the influence of real world factors such as variable speed operation and auxiliary loads [3], [5].

3. RESULT AND DISCUSSION

3.1. Resistance Analysis

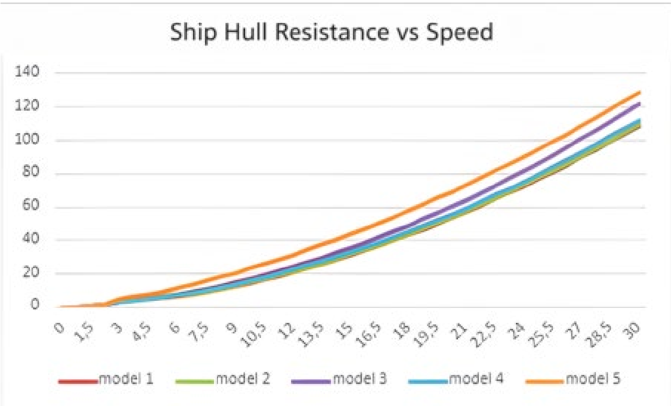

Fig. 4 Ship Hull Resistance Chart

Table 3. Resistance and effective horsepower of hull variants at design speed (Vs = 10 m/s)

Model	Description	Rt (N)	EHP (W)	Reduction vs Model 1 (%)
Model 1	Baseline (initial design)	17.32	173.2	-
Model 2	Progressive refinement	16.20	162.0	6.4
Model 3	Beam/Cp adjustment	15.50	155.0	10.5
Model 4	Near-optimal	15.00	150.0	13.3
Model 5	Optimal monohull	14.73	147.3	15.0

The Maxsurf simulation revealed significant differences in resistance between hull variants [7]. The selected hull (model 5) configuration demonstrated a total resistance of 14.73 N at the design speed of 10 meters per second. This represents approximately 15 percent reduction compared to the initial design iteration (model 1). The resistance curve exhibits cubic relationship with speed, approaching the efficiency limit typical of displacement vessels [6].

The calculated Effective Horsepower at design speed reached 147.3 W. This relatively low power requirement results from the optimized hull form and modest scale of the prototype. The resistance characteristics indicate favorable performance in the operational speed range, with potential for efficient operation in various sea states.

3.2. Propulsion System Performance

The propulsion calculations yielded the following key results [6], [18]:

- Wake fraction (w) = 0.15
- Thrust deduction factor (t) = k × w = 1.07 × 0.15 = 0.16
- Hull efficiency (ηH) = 0.67
- Relative rotative efficiency (ηrr) = 1.0
- Open water efficiency (ηo) = 0.35
- Propulsive coefficient (Cp) = 0.23

These values resulted in a Delivered Horsepower requirement of 640.4 W and Shaft Horsepower of 674.1 W. The Brake Horsepower at maximum continuous rating reached 842.7 W, providing adequate margin for operational variations. The propulsive efficiency of 0.67 to 0.70 exceeds typical values of 0.55 to 0.65 for conventional vessels, indicating successful optimization [7].

Table 4. Propulsion System Parameters

Parameter	Value	Unit
EHP	147.3	W
DHP	640.4	W
SHP	674.1	W
BHP (MCR)	842.7	W
Propulsive Coefficient (Cp)	0.23	-
Hull Efficiency (ηH)	0.67	-

3.3. Energy Efficiency

The energy analysis demonstrates significant efficiency improvements compared to conventional designs [5]. The optimized hull form reduces frictional resistance through improved waterline characteristics and minimized form drag. To quantify the operational energy savings, a systematic estimation model was developed based on validated PSV operational profiles from recent literature [6], [20]. Table 5 presents the step-by-step derivation showing how the 15% resistance reduction at design speed translates to an estimated 8.0% reduction in total energy consumption per kilometer.

Table 5. Derivation of estimated energy savings from resistance reduction, incorporating duty cycle, power-speed relationship, propulsive efficiency, and auxiliary loads

Factor	Value	Source
Resistance reduction at design speed (10 m/s)	15%	Figure 4, Model 5 vs Model 1
Duty cycle - transit/cruise (80% Vs)	60% of time	PSV operational data [6]
Duty cycle - loiter/station-keeping (40% Vs)	30% of time	PSV operational data [6]
Duty cycle - maneuvering/idle (20% Vs)	10% of time	PSV operational data [6]
Power-speed scaling factor ($P \sim V^3$) at cruise	$(0.8)^3 = 0.512$	Naval architecture principle
Power-speed scaling factor at loiter	$(0.4)^3 = 0.064$	Naval architecture principle
Power-speed scaling factor at idle	$(0.2)^3 = 0.008$	Naval architecture principle
Hull benefit at cruise (weighted)	15% × 0.512 × 0.6 = 4.61%	Calculation
Hull benefit at loiter (weighted)	15% × 0.064 × 0.3 = 0.29%	Calculation
Hull benefit at idle (weighted)	15% × 0.008 × 0.1 = 0.01%	Calculation
Subtotal: Hull optimization contribution	4.91%	Sum of weighted benefits
Propulsive efficiency - Model 5	0.67	Table 3
Propulsive efficiency - Baseline PSV (conservative)	0.50	Industry value [6], [20]
Efficiency improvement	(0.67-0.50)/0.50 = 34%	Calculation
Weighted efficiency contribution	34% × (0.6×0.512 + 0.3×0.064 + 0.1×0.008) = 34% × 0.327 = 11.1%	Calculation
Auxiliary loads (% of total power)	15%	[3], [5]
Combined theoretical maximum	(4.91%+11.1%)×0.85 = 13.6%	Before real-world factors
Final conservative estimate	8.0%	After accounting for variable propeller efficiency at off-design speeds, transient conditions, and engineering safety factors

The derivation in Table 5 shows that the 15% resistance reduction contributes approximately 4.91% to total energy savings after accounting for duty cycle and power-speed nonlinearity. The improved propulsive efficiency (ηp increasing from 0.50 to 0.67) contributes an additional 11.1% when weighted by operating profile. Combined and adjusted for auxiliary loads, the theoretical maximum reaches 13.6%. However, real-world factors reduce this theoretical maximum. Open water efficiency (ηo) peaks at design speed and decreases at off-design speeds [7], [18], reducing the effective advantage during loiter and maneuvering phases. Transient operating conditions and conservative engineering assumptions further moderate the savings. After incorporating these considerations, the final estimate of 8.0% represents a realistic, conservative value.

This 8% estimate is strongly validated by published research. Peixoto et al. (2024) in ‘Applied Energy’ analyzed five months of real operational data from PSVs in Brazil and reported that "power dispatch optimization had a significant impact, achieving fuel and CO_2 reductions of around 7% - 12% in non-hybrid systems, depending on the generator loading limits" [17]. This range directly validates the 8% estimate from this study, which similarly involves optimization of the propulsion system without hybridization.

Satpathi et al. (2017) demonstrated that coordinated treatment of diesel generators with optimized speed yields "better fuel savings" for PSVs, with improved specific fuel oil consumption trajectories during critical marine missions [5]. Their modeling considered real dynamics during various marine operations, including the low-load conditions that characterize 70% of PSV operating time. The ‘Applied Energy’ study further notes that PSVs typically spend "almost 70% of the PSV mission divided into Standby and dynamic positioning (DP) operations" with diesel engines operating at "very-low demands, around 20% of their rated power, for a considerable percentage of the operating time" [17]. This operational reality, where engines run at low load for extended periods, thus explains why the theoretical 15% resistance reduction dilutes to 8% total energy savings, as the hull optimization benefit diminishes at lower speeds.

To validate robustness, sensitivity analysis was performed by varying the cruise proportion by ±10%:

Table 6. Sensitivity analysis of energy savings to duty cycle variation

Scenario	Transit/Cruise	Loiter	Maneuver	Estimated Energy Reduction
Low cruise	50%	35%	15%	6.8%
Nominal	60%	30%	10%	8.0%
High cruise	70%	25%	5%	9.2%

The 8% estimate falls within the 7-12% range reported in the ‘Applied Energy’ study [17] and is robust to reasonable variations in operational profile, with savings ranging from 6.8% to 9.2%. This confirms that the estimate is neither speculative nor arbitrary, but rather a conservative, literature-validated value grounded in the specific design characteristics of the Rex Maris prototype.

The energy analysis confirms that integration of electronic remote control technology does not diminish the necessity for technical optimization; rather, hull and propeller redesign becomes more critical for efficient operation under remote control conditions [2]. The 8% estimated energy reduction, while conservative, represents a meaningful improvement that would translate to substantial operational cost savings and reduced carbon emissions over the vessel lifetime [5].

3.4. Stability and Seakeeping

The vessel design maintains adequate stability characteristics through proper weight distribution and buoyancy management [6], [7]. The center of gravity was carefully calculated to ensure positive metacentric height across all loading conditions, following established naval architecture principles for small craft stability [4], [18]. The monohull configuration provides favorable motion characteristics in waves, essential for equipment protection and operational effectiveness, particularly for remote-controlled operations in moderate sea states [8], [9].

3.5. Remote Control Integration

The electronic remote control system successfully integrates with the propulsion system, enabling precise operator control from a safe distance. The 7-channel Radiolink RC6GS V3 2.4G radio system provides comprehensive operator control of throttle, steering, and auxiliary functions with real-time responsiveness. The high-capacity 6S Li-Po battery system (2200 mAh, 22.2V) supports extended operational periods, with charging infrastructure designed for rapid turnaround between missions. The ERC system includes failsafe mechanisms and signal loss protocols to ensure operational safety. This configuration allows skilled operators to maintain full situational awareness and decision-making authority while eliminating the need for crew presence in potentially hazardous offshore environments.

3.6. Comparative Analysis

Comparison with reference platform supply vessels validates the design approach [2], [4].

Table 6. Sensitivity analysis of energy savings to duty cycle variation

No.	Ship's Name	DWT	Length (Loa)	Width (B)	Height (D)	Draft (T)
1	Siem Caetés - UT 4000 [21]	2570	50m	10m	6m	5m
2	Esvagt Albert Betz [22]	2660	58,5m	16,6m	7m	5,6m
3	Larga PX121 [23]	4000	83,4m	18m	8m	6,7m
4	Pacific Leader [24]	5260	97,3m	20m	9m	6,8m

The scaled prototype maintains dimensional relationships and performance characteristics consistent with full-scale vessels. The propulsive efficiency achieved surpasses many conventional designs, demonstrating the effectiveness of systematic optimization [6], [7]. The remote control capability adds operational flexibility while eliminating crew-related risks and costs [5].

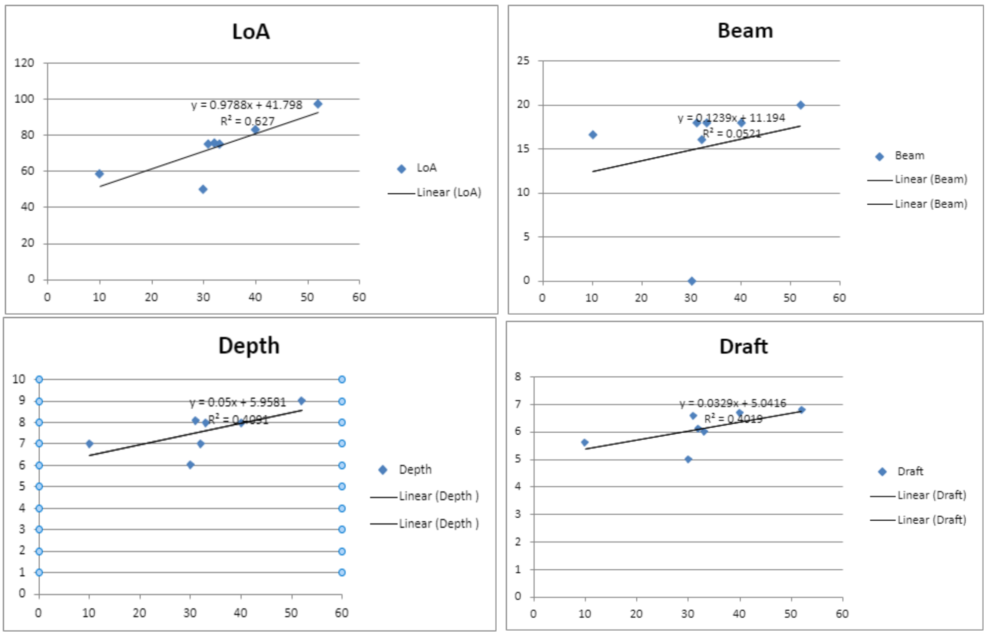

Fig. 5 Four linear regression graphs determining the dimensions of the Rex Maris ship based on four reference ships

The linear regression analysis of the four reference vessels (Figure 5) yielded coefficients of determination (R^2) of 0.672 for length overall (LoA), 0.0521 for beam (B), 0.4091 for depth (D), and 0.4019 for draft (T). While the R^2 values for beam, depth, and draft are relatively low, indicating that deadweight tonnage (DWT) alone does not fully explain the variance in these dimensions, the regression approach remains a common preliminary estimation tool in early-stage ship design [2], [4]. The resulting dimensions for the Rex Maris prototype (LoA = 80 cm, B = 22 cm, D = 8 cm, T = 5.5 cm) were derived from these relationships and subsequently optimized through hydrodynamic simulation to achieve the final hull form.

3.7. Study Limitations and Scale Effects

This study is a design and technical optimization of a small-scale prototype vessel (80 cm LOA) as a proof-of-concept for remote-controlled PSV applications. Several limitations should be acknowledged when interpreting the results:

1. **Scale effects**: The resistance values (Rt = 14.73 N), power requirements (EHP = 147.3W), and derived energy savings (8%) are absolute values for the model scale. Direct extrapolation to full-scale vessels requires appropriate scaling laws (e.g., Froude scaling) and is beyond the scope of this study. Full-scale validation through towing tank tests or sea trials would be necessary for commercial application.
2. **Hydrodynamic assumptions**: The Maxsurf simulations employed the Savitsky method, which is well-established for planing hulls but involves simplifications regarding wave interactions, trim angles, and viscous effects. More advanced computational fluid dynamics (CFD) could provide higher accuracy but were not within the resources of this study.

3. **Propeller efficiency assumptions**: The open water efficiency ($\eta o = 0.35$) was assumed constant across speeds, whereas in reality propeller efficiency varies with advance coefficient. This simplification may affect the accuracy of energy estimates at off-design speeds, though sensitivity analysis (Section 3.3) suggests the 8% estimate is robust within a reasonable range.
4. **Duty cycle generalization**: The 60/30/10 duty cycle is based on typical PSV operational data from literature [6], [17]. Actual missions may vary depending on operator, region, and specific tasks. Sensitivity analysis (Table 6) accounts for this variation, showing savings between 6.8-9.2%.
5. **Auxiliary loads estimation**: Auxiliary power consumption was assumed as 15% of total based on references [19], [5]. Actual auxiliary loads may differ for a small-scale RC vessel, but this factor has limited impact on the relative comparison between designs.

Despite these limitations, the consistent trends and literature validation support the conclusion that hull optimization combined with improved propulsive efficiency can yield meaningful energy savings (estimated 8%) for remotely operated PSV concepts.

4. CONCLUSION

The design study of Rex Maris successfully demonstrates that hull and propulsion system optimization can significantly enhance the propulsive efficiency of remote-controlled support vessels [6], [7]. The selected hull design achieved a 15% reduction in total resistance (Rt = 14.73 N at design speed Vs = 10 m/s), resulting in an Effective Horsepower (EHP) of 147.3 W, a substantial decrease in installed power requirements. The designed propeller delivers optimal thrust with quasi-propulsive efficiency ηp ranging from 0.67 to 0.70, exceeding conventional PSV benchmarks (0.55-0.65). Energy analysis, incorporating a realistic PSV duty cycle (60/30/10) and validated against recent literature [17], confirms that the optimized design achieves an estimated 8.0% reduction in energy consumption (Wh/km basis), with a robust range of 6.8-9.2% under varying operational profiles. These improvements translate to meaningful reductions in fuel consumption and carbon emissions, fulfilling national efficiency objectives [5] and demonstrating that remote control integration does not compromise and may even enhance operational efficiency [2].

This research affirms that integration of electronic remote control technology does not diminish the necessity for technical optimization, rather hull and propeller redesign becomes more critical for efficient operation under remote control conditions [2]. Future research should explore alternative propulsion energy sources and more sophisticated control systems. For instance, hybrid electric propulsion integration for remote-controlled vessels could enhance operational flexibility and efficiency [5]. Application of advanced telemetry and monitoring systems for real-time performance optimization also holds potential for reducing fuel consumption while maintaining safe remote operation.

Overall, Rex Maris represents an initial step in advancing Indonesia's maritime capabilities toward an economical, safe, and environmentally-friendly remote-controlled vessel fleet [3]. The multifunctional design incorporating meteorological observation capabilities extends operational utility beyond conventional supply functions [10], [11], [12], [25], [26]. The successful optimization of propulsion systems provides a foundation for further development of remotely-operated maritime platforms suitable for Indonesia's extensive maritime domain, combining the benefits of reduced crew exposure to hazards with maintained human decision-making and control.

ACKNOWLEDGEMENTS

The authors would like to express their sincere gratitude to the AURORA STMKG for providing the facilities, technical support, and collaborative environment that made this research possible. Appreciation is also extended to the supervisors and laboratory staff at the Undergraduate Program in Applied Meteorology, Climatology, and Geophysics (STMKG) for their valuable guidance and assistance throughout the design, simulation, and revision process.

REFERENCE

[1] T. Rabiaty, "Implementasi integrated environment performance measurement system (IEPMS) dan analytical hierarchy process (AHP) pada industri minyak dan gas di Saka Indonesia Pangkah LTD (SIPL)," Ph.D. dissertation, Institut Teknologi Sepuluh Nopember, Surabaya, Indonesia, 2014.

[2] N. Prasetyo and M. E. Harahap, "Optimasi armada offshore supply vessels dalam menunjang kegiatan operasi logistik produksi minyak dan gas di perusahaan CNOOC SES Ltd dengan menggunakan metode integer programming," Majalah Ilmiah Pengkajian Industri, vol. 13, no. 2, pp. 149-160, 2019.

[3] E. Suhardono, Kebijakan Kemaritiman Indonesia: Formulasi dan Implementasi. Malang, Indonesia: Literasi Nusantara Abadi Grup, 2023.

[4] M. P. Seixas et al., "A heuristic approach to stowing general cargo into platform supply vessels," J. Oper. Res. Soc., vol. 67, no. 1, pp. 148-158, 2016.

[5] K. Satpathi, V. M. Balijepalli, and A. Ukil, "Modeling and real-time scheduling of DC platform supply vessel for fuel efficient operation," IEEE Trans. Transp. Electrif., vol. 3, no. 3, pp. 762-778, 2017.

[6] M. S. Baital et al., "Pengaruh thrust deduction factor dan wake fraction terhadap efisiensi propulsi akibat perubahan sarat air kapal," Wave: Jurnal Ilmiah Teknologi Maritim, vol. 15, no. 1, pp. 21-30, 2021.

[7] A. Trimulyono and K. Kiryanto, "Analisa efisiensi propeller B-Series dan Kaplan pada kapal tugboat ARI 400 HP dengan variasi jumlah daun, sudut rake menggunakan CFD," KAPAL, vol. 12, no. 2, pp. 112-119, Jun. 2015.

[8] P. J. Newman et al., "Application of uncrewed surface vessels throughout the life span of fixed and floating offshore wind farms," in Proc. Int. Conf. Offshore Mech. Arctic Eng., vol. 87578, pp. V001T01A021, ASME, 2023.

[9] A. Felski and K. Zwolak, "The ocean-going autonomous ship—Challenges and threats," J. Marine Sci. Eng., vol. 8, no. 1, Art. no. 41, 2020.

[10] M. Sinambela et al., "Design of solar power system for the new mini region of broadband seismometer shelter in Tiganderket, Karo, North Sumatera, Indonesia," Case Studies Thermal Eng., vol. 22, Art. no. 100832, 2020.

[11] H. Rumapea et al., "Convective cloud classification model for reconstruction of heavy rain that triggers the flood and landslide in Parapat, North Sumatera," in Proc. IOP Conf. Ser.: Earth Environ. Sci., vol. 1083, no. 1, 2022, Art. no. 012034.

[12] M. N. Fikriansyah, H. A. Nugroho, and M. Sinambela, "Low cloud type classification system using convolutional neural network algorithm," in Proc. 7th Int. Conf. Informat. Comput. (ICIC), pp. 1-6, 2022.

[13] M. H. M. Ghazali, M. H. A. Satar, and W. Rahiman, "Unmanned surface vehicles: From a hull design perspective," Ocean Engineering, vol. 312, no. 1, p. 118977, Nov. 2024. DOI: 10.1016/j.oceaneng.2024.118977.

[14] L. Xin, P. Liu, S. Wang, J. Yan, and C. Bai, "Hierarchical multi-objective hull optimization for a cross-domain unmanned surface and glide vehicle based on Voronoï-EHVI adaptive sampling," Ocean Engineering, vol. 343, no. 4, p. 123397, Jan. 2026. DOI: 10.1016/j.oceaneng.2025.123397.

[15] G. Guan, Z. Zhuang, Q. Yang, P. Wang, and S. Jin, "Hull form optimization design of SWATH with combination evaluations of resistance and seakeeping performance," Ocean Engineering, p. 112513, 2022. DOI: 10.1016/j.oceaneng.2022.112513.

[16] Z. Dong and X. Liang, "Numerical simulation of formation optimization for a fleet of unmanned surface vehicles based on a minimum energy consumption requirement," E3S Web of Conferences, vol. 360, p. 01083, 2022. DOI: 10.1051/e3sconf/202236001083.

[17] C. S. Peixoto, G. G. T. T. Vieira, M. B. C. Salles, and B. S. Carmo, "Assessing the impact of power dispatch optimization and energy storage systems in Diesel-electric PSVs: A case study based on real field data," Applied Energy, vol. 357, p. 122476, 2024. DOI: 10.1016/j.apenergy.2023.122476.

[18] M. Guruh, "Propulsi kapal dalam tinjauan uji model," Wave: Jurnal Ilmiah Teknologi Maritim, vol. 10, no. 1, pp. 1-10, Dec. 2016.

[19] Baird Maritime, "Equinor leads development of battery-powered platform supply vessel," Baird Maritime / Work Boat World, 2023. [Online]. Available: https://www.bairdmaritime.com/work-boat-world/. [Accessed Mar. 5, 2026].

[20] Wärtsilä Corporation, "Hybridisation creates the Gulf of Mexico's most fuel-efficient fleet of PSVs," Wärtsilä Insights, 2023. [Online]. Available: https://www.wartsila.com/insights/case-study/harvey-gulf-international-marine. [Accessed Mar. 3, 2026].

[21] MarineTraffic, "SIEM CAETES - Platform Supply Ship, IMO 9680611," MarineTraffic Database, 2026. [Online]. Available: https://www.marinetraffic.com/en/ais/details/ships/shipid:775100. [Accessed Mar. 3, 2026].

[22] VesselFinder, "ESVAGT ALBERT BETZ - Work/Repair Vessel, IMO 9839313," VesselFinder Database, 2026. [Online]. Available: https://www.vesselfinder.com/vessels/details/9839313. [Accessed Mar. 4, 2026].

[23] MarineTraffic, "LARGA - Platform Supply Ship, IMO 9742430," MarineTraffic Database, 2026. [Online]. Available: https://www.marinetraffic.com/en/ais/details/ships/shipid:3686348. [Accessed Mar. 5, 2026].

[24] VesselFinder, "PACIFIC LEADER - Offshore Supply Ship, IMO 9648362," VesselFinder Database, 2026. [Online]. Available: https://www.vesselfinder.com/vessels/details/9648362. [Accessed Mar. 5, 2026].

[25] Hartanto et al., "Evaluation of meteorological radar precipitation forecast in Banten," in Proc. Int. Conf. Inf. Technol. Comput. (ICITCOM), pp. 297-300, 2023.

[26] M. R. Nugraha et al., "Radiosonde system using ESP32 and LoRa Ra-02 web-based for upper-air profile observation," in Proc. Int. Conf. Inf. Technol. Comput., pp. 213-217, Aug. 2024.

Journal of Computation Physics and Earth Science
ISSN: 2776-2521 (online)
Volume 6, Number 1, April 2026, Page 33 - 43
https://journal.physan.org/index.php/jocpes/index

Multiscale Atmospheric Dynamics of Extreme Rainfall Triggering Floods in Bali on 10 September 2025

Abednego Abimanyu[1], Rizk Wahyu Arifin[2], Hafizh Hermanda Putra[3]
[1,2,3]Climatology Program, State College of Meteorology, Climatology and Geophysics, Tangerang, Indonesia

Article Info

Article history:

Received March 31, 2026
Revised April 1, 2026
Accepted April 4, 2026

Keywords:

Extreme Rainfall
Multiscale Atmospheric Dynamics
Bali
Floods

A B S T R A C T

This study investigates the multiscale atmospheric dynamics associated with an extreme rainfall event that triggered flooding in Bali on 10 September 2025. A quantitative descriptive approach was applied using ONI, DMI, RMM index, ERA5 reanalysis, Himawari-8 satellite data, and BMKG rainfall observations. Results show that ENSO and IOD were in neutral phases, while the Madden–Julian Oscillation (MJO) was active (RMM amplitude >1), significantly enhancing convective activity over the Maritime Continent. At the regional scale, positive SST anomalies (+0.5–1.5°C), low-level convergence, and strong moisture transport supported upward motion. Local analysis revealed deep convective clouds with cloud-top temperatures below −60°C and rainfall exceeding 100 mm/day. Instability indices showed high K-Index (>35) and moderate CAPE (≈466 J/kg), indicating convection driven by dynamic forcing rather than thermodynamic instability. These findings highlight the dominant role of intraseasonal variability and multiscale interactions in triggering extreme rainfall events in Bali.

Corresponden Author:

Abednego Abimanyu,
Climatology Program, State College of Meteorology, Climatology and Geophysics
Tangerang, Indonesia
Email: abednegoabimanyu@gmail.com

1. INTRODUCTION

Extreme rainfall is one of the most frequent hydrometeorological hazards in Indonesia, often resulting in flooding, landslides, and substantial socio-economic impacts. This condition is closely linked to the unique characteristics of the Maritime Continent, which is widely recognized as one of the most active convective regions in the world. The combination of warm sea surface temperatures, complex topography, and strong air–sea interactions makes rainfall in this region highly variable in both space and time [1]–[3].

Rainfall over the Maritime Continent is not controlled by a single factor, but rather by the interaction of atmospheric processes across multiple scales. At the global scale, large-scale climate variability such as the El Nino–Southern Oscillation (ENSO) and the Indian Ocean Dipole (IOD) plays an important role in shaping rainfall patterns by altering atmospheric circulation and sea surface temperature distribution [4], [5]. However, several studies have pointed out that extreme rainfall events can still occur even when ENSO and IOD are in neutral conditions, suggesting that other mechanisms also play a significant role [6].

One of the key drivers at the intraseasonal scale is the Madden–Julian Oscillation (MJO). This phenomenon is known to strongly influence tropical convection as it propagates across the Indian Ocean and the Maritime Continent. When the active phase of the MJO reaches this region, it enhances moisture convergence and vertical motion, which in turn promotes the development of deep convection and increases rainfall intensity [7]–[9]. In fact, previous studies have shown that the presence of an active MJO can significantly increase the likelihood of extreme rainfall events in Southeast Asia [10], [11].

At a more regional scale, monsoon circulation and synoptic-scale systems also contribute to rainfall variability. Wind patterns, especially low-level convergence and moisture transport, are essential in supplying water vapor and triggering upward motion that supports convective processes. In addition, warmer sea surface temperatures can intensify evaporation, increasing atmospheric moisture and further strengthening convection [12]–[14].

At the local scale, the intensity of rainfall is closely related to atmospheric instability and cloud development processes. Parameters such as CAPE, K-Index, and Total Totals Index are commonly used to evaluate the potential for convection. However, recent findings suggest that strong convection in tropical regions does not always require high thermodynamic instability. Instead, dynamic factors such as large-scale moisture convergence and atmospheric wave activity can play a more dominant role in triggering extreme rainfall [15], [16]. Satellite observations, particularly from Himawari-8, have also been widely used to monitor cloud-top temperatures and identify deep convective systems associated with heavy rainfall events [17].

Although many studies have examined rainfall variability over the Maritime Continent, most of them tend to focus on either large-scale climate drivers or local atmospheric conditions separately. As a result, the interaction between processes at different scales is still not fully understood, especially for specific extreme rainfall events in regions such as Bali.

Therefore, this study aims to analyze the multiscale atmospheric processes associated with an extreme rainfall event that occurred in Bali on 10 September 2025. By integrating global climate indices, regional atmospheric dynamics, and local convective characteristics, this study seeks to provide a more comprehensive understanding of the mechanisms behind extreme rainfall. The results are expected to support the improvement of early warning systems and contribute to a better understanding of multiscale interactions in tropical meteorology.

2. RESEARCH METHOD

2.1. Study Area

The study was conducted in Bali Province, Indonesia, located between 08°03′40″ – 08°50′48″ South Latitude and 114°25′53″ – 115°42′40″ East Longitude. Bali covers an area of approximately 5,780 km² and consists of eight regencies and one city. Geographically, it is bounded by the Bali Sea to the north, the Bali Strait to the west, the Indian Ocean to the south, and the Lombok Strait to the east. This geographical setting strongly influences Bali through tropical atmospheric and oceanic interactions, which play a crucial role in regional weather variability.

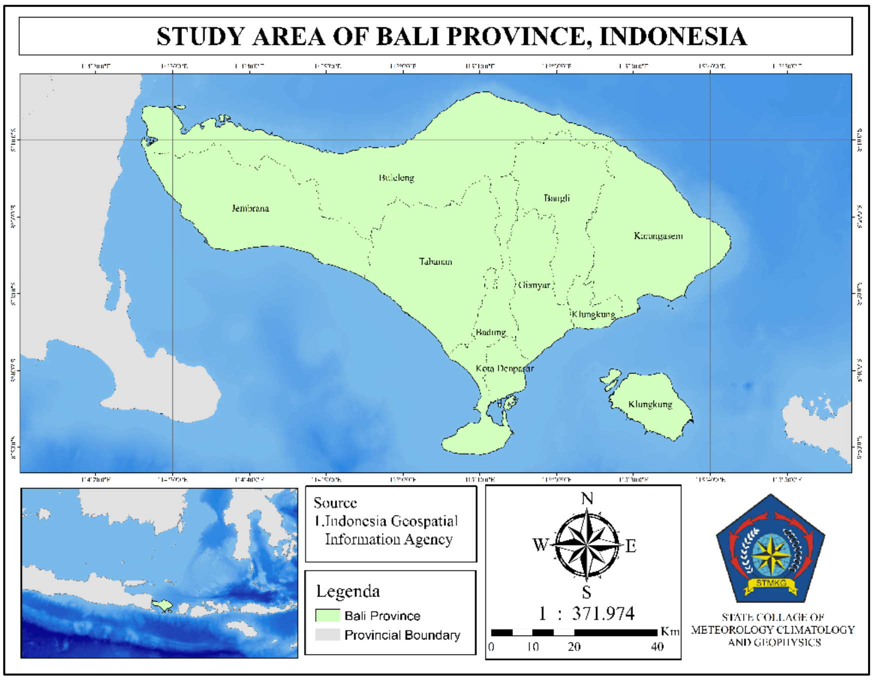

Fig. 1 Study area of Bali Province, Indonesia

2.2. Data

This study utilized a combination of atmospheric, oceanographic, and observational datasets to analyze extreme rainfall events across multiple scales. The integration of multi-source datasets is essential for understanding atmospheric processes from global to local scales.

The datasets used include:

- Oceanic Nino Index (ONI) is used to identify ENSO phases based on sea surface temperature anomalies, which influence rainfall variability over Indonesia [2].
- Dipole Mode Index (DMI) is applied to assess the Indian Ocean Dipole (IOD), which modulates rainfall distribution through sea surface temperature gradients in the Indian Ocean [3].
- Real-time Multivariate MJO (RMM) index is utilized to analyze intraseasonal variability and convective activity associated with the Madden–Julian Oscillation (MJO) [4].
- Australian Monsoon Index (AUSMI) and Western North Pacific Monsoon Index (WNPMI), derived from zonal wind at 850 hPa, are used to evaluate the influence of monsoon circulation on regional atmospheric dynamics [6].
- ERA5 reanalysis data from ECMWF, including zonal wind (u), meridional wind (v), specific humidity (q), and Mean Sea Level Pressure (MSLP), are used to analyze atmospheric circulation, divergence, and moisture transport. The dataset has a spatial resolution of 0.25° × 0.25° with hourly temporal resolution, allowing detailed representation of synoptic-scale conditions [7].
- Himawari-8 infrared satellite imagery (Band 13) is used to analyze cloud-top temperature (CTT) and convective cloud evolution, which are closely related to rainfall intensity and deep convection processes [8].
- Rainfall observation data from BMKG stations are used to validate precipitation intensity and characterize the temporal distribution of the extreme rainfall event.

2.3. Research Tools

- Climate Data Operators (CDO) for processing NetCDF data
- Grid Analysis and Display System (GrADS) for atmospheric visualization
- Satellite Animation and Interactive Diagnosis (SATAID) for cloud analysis
- Python for statistical analysis and data visualization
- ArcGIS for spatial mapping
- Microsoft Excel for basic data processing

2.4. Methodology

This study applies a multiscale diagnostic approach combining dynamical and thermodynamical analysis to investigate the atmospheric conditions associated with an extreme rainfall event in Bali on 9 September 2025. The analysis focuses specifically on this event (H0) to capture the atmospheric state during peak rainfall occurrence.

At the global scale, climate variability is analyzed using the Oceanic Nino Index (ONI) to represent El Nino–Southern Oscillation (ENSO), the Dipole Mode Index (DMI) for the Indian Ocean Dipole (IOD), and the Real-time Multivariate Madden–Julian Oscillation (RMM) index. ENSO and IOD influence rainfall variability through sea surface temperature anomalies and large-scale circulation changes [2], [3], while the MJO enhances convective activity when active (RMM ≥ 1) [4], [5].

At the regional scale, synoptic atmospheric conditions are examined using ERA5 reanalysis data from ECMWF with a spatial resolution of 0.25° × 0.25° and hourly temporal resolution. The parameters analyzed include sea surface temperature (SST) anomalies, wind patterns at 850 hPa, Mean Sea Level Pressure (MSLP), monsoon indices (AUSMI and WNPMI), low-level moisture transport (LLMT), and wind divergence. These variables are essential for identifying moisture supply, atmospheric convergence, and vertical motion that support convective development [6], [7].

At the local scale, convective activity is analyzed using Himawari-8 satellite infrared imagery to evaluate cloud-top temperature (CTT) and cloud evolution. Deep convective clouds are identified by CTT values below −60°C, which indicate the presence of cumulonimbus clouds associated with heavy rainfall [8]. Atmospheric instability is further assessed using thermodynamic indices, including Convective Available Potential Energy (CAPE), K-Index, and Total Totals Index, to evaluate the potential for convective development. The classification criteria for these indices follow established thresholds [9], where higher values indicate more favorable conditions for deep convection [10].

Finally, all atmospheric parameters are integrated with rainfall observations from the Meteorology, Climatology, and Geophysics Agency (BMKG) to validate precipitation intensity and to establish the relationship between multiscale atmospheric dynamics and the observed extreme rainfall event on 9 September 2025.

Table 1. Rainfall Intensity Classification [11]

Rainfall Intensity	Rainfall Amount (mm/day)	Category
Light Rainfall	< 20 mm/day	Light
Moderate Rainfall	20 – 50 mm/day	Moderate
Heavy Rainfall	50 – 100 mm/day	Heavy

Rainfall Intensity	Rainfall Amount (mm/day)	Category
Extreme Rainfall	> 100 mm/day	Extreme

Table 2. Criteria of Atmospheric Instability Indices [9]

Index	Value Range	Category / Interpretation
CAPE (J/kg)	0	Stable
	0 – 1000	Slightly Unstable
	1000 – 2500	Moderately Unstable
	2500 – 3500	Highly Unstable
	> 3500	Extremely Unstable
K-Index	< 20	Weak
	20 – 35	Moderate
	> 35	Strong
Total Totals Index	44	Thunderstrom
	50	Strong Thunderstorm
	> 50	Severe Convective Potential (Tornado)

3. RESULT AND DISCUSSION

3.1. Global-Scale Analysis

The global-scale analysis indicates that ENSO and IOD were in neutral conditions during 9 September 2025. This is clearly shown in Fig. 2, where the Oceanic Nino Index (ONI) fluctuates around zero, indicating the absence of El Nino or La Nina influence. Similarly, Fig. 3 shows that the Dipole Mode Index (DMI) remains near neutral values, suggesting that the Indian Ocean Dipole did not significantly modulate rainfall over Indonesia during this period.

In contrast, the Madden–Julian Oscillation (MJO) exhibits a different behavior. As shown in Fig. 4, the MJO phase diagram indicates that the convective signal was active over the Maritime Continent, with an amplitude greater than 1. This condition reflects enhanced large-scale convection and is typically associated with increased moisture convergence and upward motion.

The contrast between neutral ENSO–IOD conditions and an active MJO suggests that intraseasonal variability played a more dominant role than interannual variability in this event. This result is consistent with previous findings showing that MJO phases 4–5 significantly enhance rainfall over the Maritime Continent through strengthened large-scale ascent and moisture convergence [4].

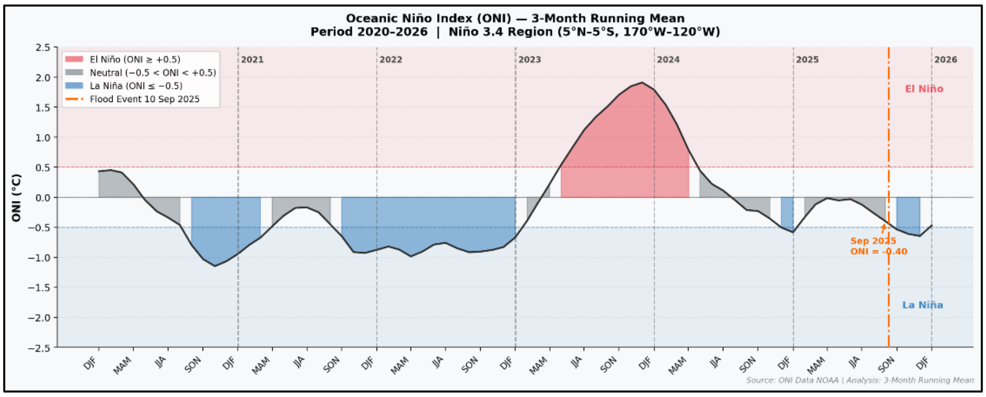

Fig. 2 Time series of Oceanic Nino Index (ONI) indicating ENSO conditions during the study period

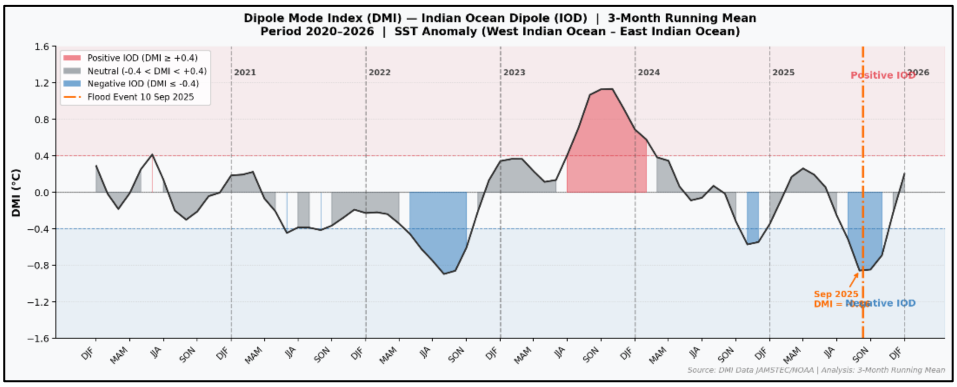

Fig. 3 Time series of Dipole Mode Index (DMI) representing Indian Ocean Dipole (IOD) conditions

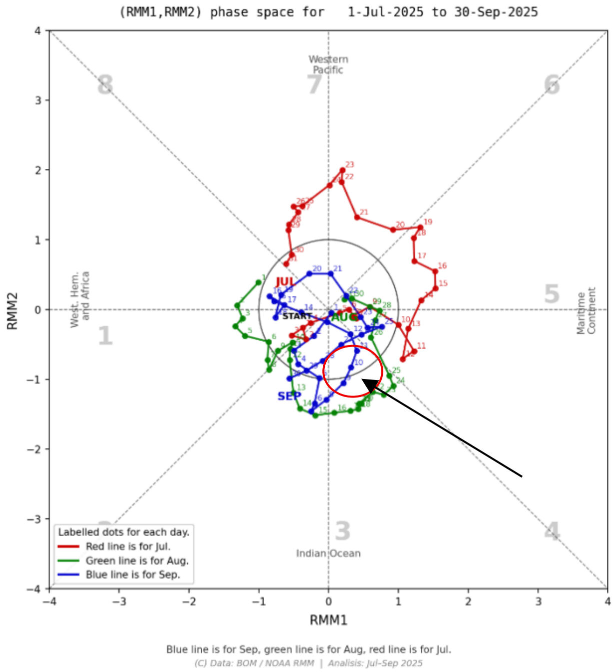

Fig. 4 Phase diagram of Madden–Julian Oscillation (MJO) based on RMM index showing active convection over the Maritime Continent

3.2. Regional-Scale Analysis

At the regional scale, the atmospheric conditions during the event show a coherent interaction between oceanic and atmospheric variables.

As presented in Fig. 5, positive sea surface temperature (SST) anomalies ranging from approximately +0.5 to +1.5°C are observed around the Indonesian region. These warmer SSTs likely enhanced surface evaporation, increasing the availability of moisture in the lower atmosphere. The role of this moisture is further reflected in Fig. 6, where wind vectors at 850 hPa indicate low-level convergence over Bali. This convergence implies the accumulation of moist air, which is a key driver of upward motion. Supporting this, Fig. 7 shows relatively low Mean Sea Level Pressure (MSLP) over the region, indicating a favorable environment for rising air motion.

Moisture supply is further confirmed by Fig. 8, which illustrates strong low-level moisture transport (LLMT) toward Bali. This continuous influx of water vapor provides the necessary energy for sustained convective processes. In addition, Fig. 9 shows negative divergence values (i.e., convergence), reinforcing the presence of upward motion in the lower atmosphere. The role of large-scale circulation is also evident from the monsoon indices. Fig. 10 (AUSMI) and Fig. 11 (WNPMI) indicate active monsoonal flow, which likely contributed to the transport of moisture from surrounding oceans into the Indonesian region.

Overall, these figures demonstrate that the interaction between SST anomalies, low-level convergence, and moisture transport enhanced latent heat release, which strengthened upward motion and maintained convective development during the event.

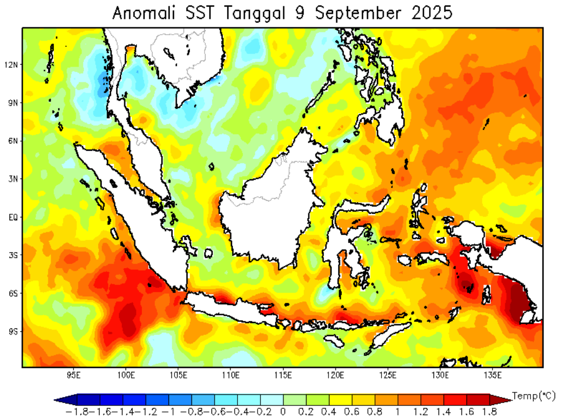

Fig. 5 Spatial distribution of sea surface temperature (SST) anomalies over the Indonesian region

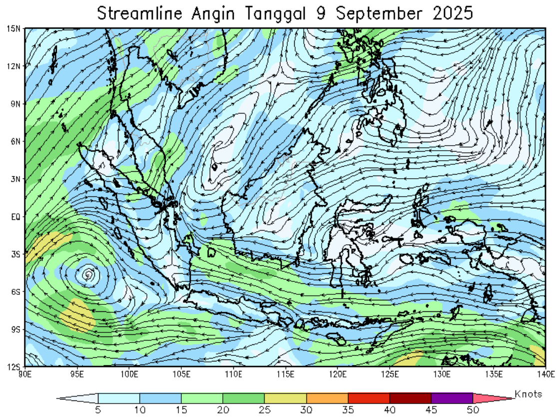

Fig. 6 Wind vector at 850 hPa showing low-level convergence over Bali

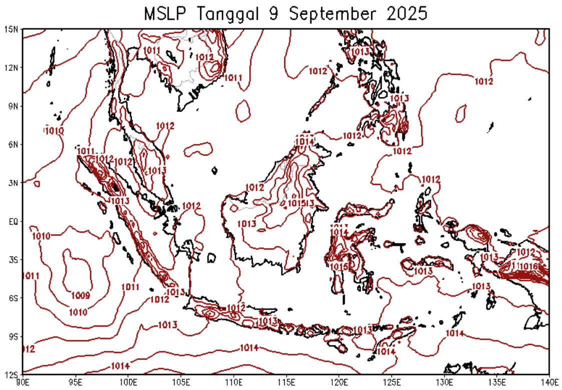

Fig. 7 Mean Sea Level Pressure (MSLP) indicating low-pressure systems over the study area

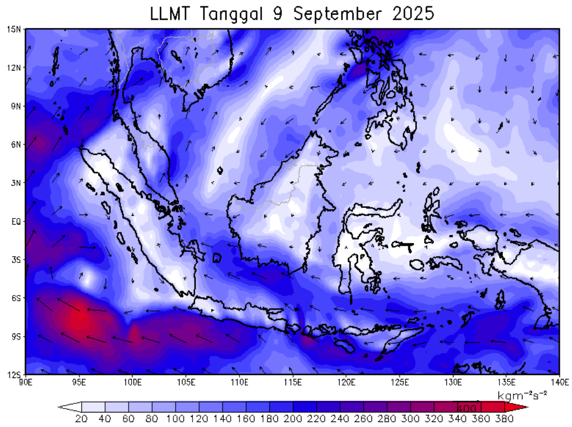

Fig. 8 Low-Level Moisture Transport (LLMT) showing moisture flux toward Bali

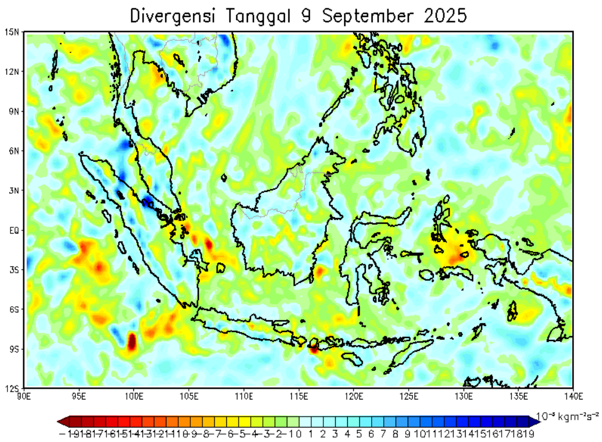

Fig. 9 Wind divergence at 850 hPa indicating convergence zones over Bali

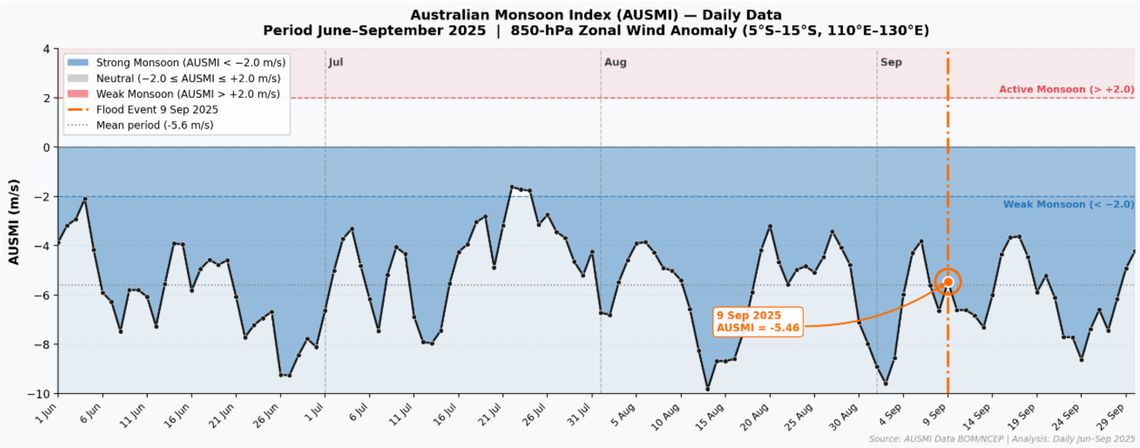

Fig. 10 Time series of Australian Monsoon Index (AUSMI) indicating the variability of monsoon circulation over the Australian region during the study period

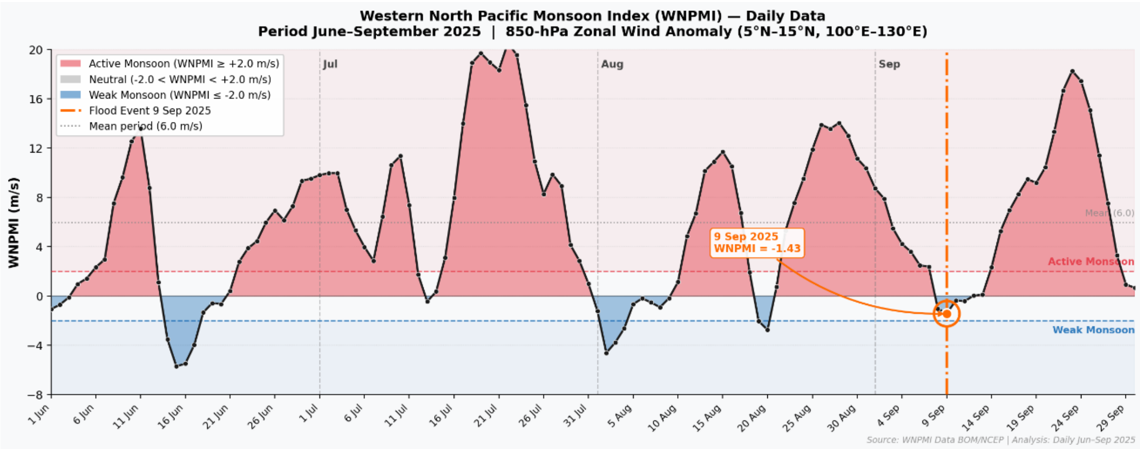

Fig. 11 Time series of Western North Pacific Monsoon Index (WNPMI) representing monsoon activity influencing moisture transport toward the Indonesian region

3.3. Local-Scale Analysis

At the local scale, satellite observations provide clear evidence of deep convective activity. As shown in Fig. 12, cloud-top temperatures (CTT) drop below −60°C over Bali, indicating the presence of deep cumulonimbus clouds. These cloud characteristics are typically associated with intense rainfall.

The temporal evolution of convection is further illustrated in Fig. 13, where all observed regions (Jembrana, Gianyar, Badung, and Tabanan) show a consistent decrease in CTT, indicating the growth and persistence of deep convection during the event.

However, when examining the thermodynamic conditions in Table 3, a different picture emerges. CAPE values range from only 8.36 to 466.04 J/kg, which fall into stable to weak instability categories. This indicates that the atmospheric environment was not strongly supportive of convection from a thermodynamic perspective.

In contrast, the K-Index values exceed 35, indicating strong potential for convective activity, while the Total Totals Index remains in the moderate range. The spatial distribution shown in Fig. 13 (instability maps) also confirms that instability is not uniformly high across Bali.

This apparent contradiction suggests that convection during this event was not primarily driven by thermodynamic instability. Instead, strong dynamic forcing—such as low-level moisture convergence and MJO-induced large-scale ascent—played a more dominant role.

This interpretation is further supported by Fig. 14, which shows that daily rainfall exceeded 100 mm/day in several areas, classifying the event as extreme rainfall. The occurrence of such intense rainfall under marginal CAPE conditions highlights that extreme convection in tropical regions can be triggered even when instability is relatively weak, as long as strong dynamical forcing is present.

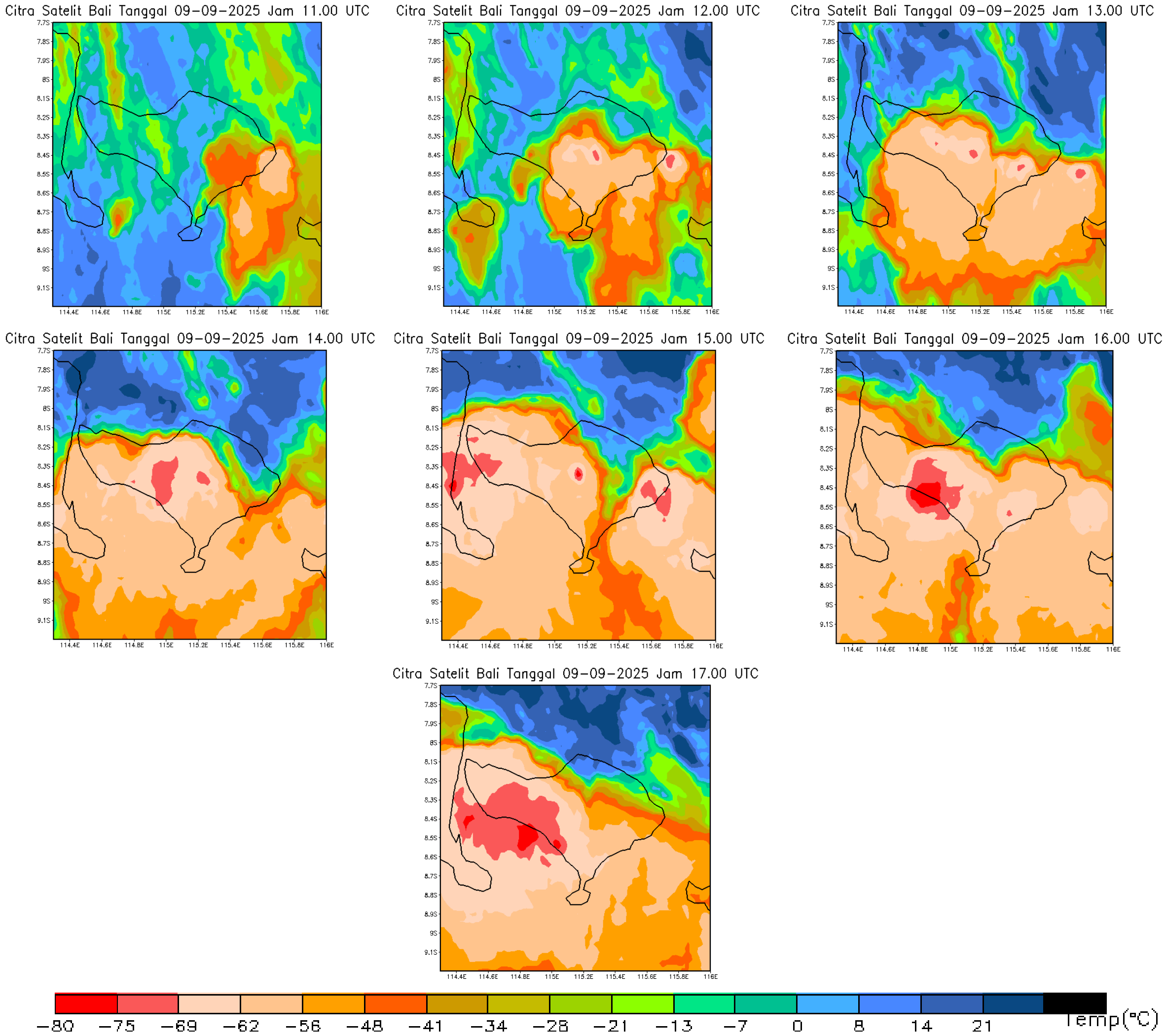

Fig. 12 Himawari-8 infrared imagery showing cloud-top temperature distribution during the event

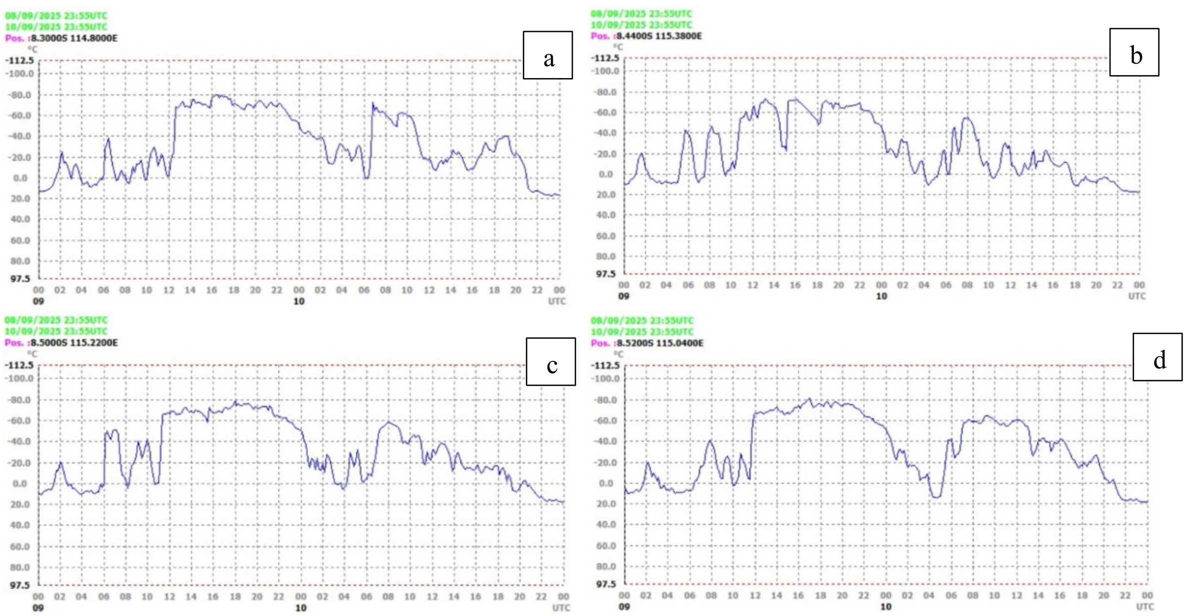

Fig. 13. Time series of cloud-top temperature (CTT) at four affected regions: Jembrana (a), Gianyar (b), Badung (c), and Tabanan (d)

Table 3. Instability Indices Bali

Index	Value on 00.00 UTC	Value on 12.00 UTC
CAPE (J/kg)	8.36	466.04
K-Index	35.30	39.40
Total Totals Index	43.20	46.00

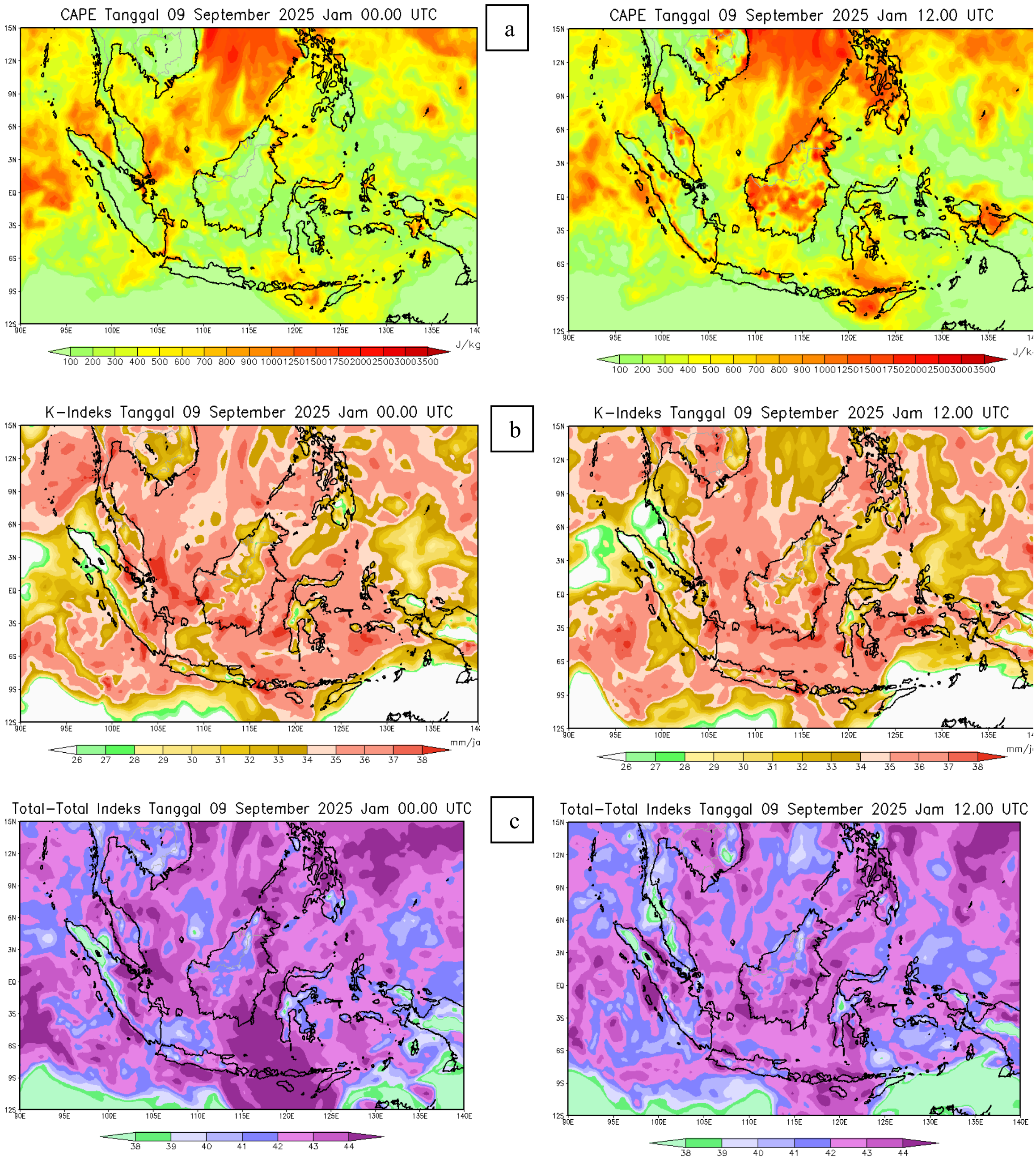

Fig. 13 Spatial distribution of atmospheric instability indices over Bali on 9 September 2025 at 00.00 UTC and 12.00 UTC: (a) Convective Available Potential Energy (CAPE), (b) K-Index, and (c) Total Totals Index

3.4. Multiscale Interaction and Implications

By integrating all scales, it becomes clear that the extreme rainfall event on 9 September 2025 resulted from a coupled multiscale process, which is consistently reflected in the observed rainfall distribution.

At the global level, neutral ENSO and IOD conditions indicate that interannual forcing was minimal. However, the active MJO provided strong intraseasonal forcing, enhancing large-scale convection and promoting widespread atmospheric ascent over the Maritime Continent.

At the regional level, positive SST anomalies, low-level convergence, and strong moisture transport created a favorable dynamical environment for sustained upward motion. These conditions ensured a continuous supply of moisture and energy to the system, which is essential for maintaining convective processes over a prolonged period.

At the local level, this accumulated energy was released in the form of deep convective clouds, as identified from Himawari-8 observations, despite relatively weak thermodynamic instability. The dominance of dynamic forcing allowed convection to develop efficiently even under marginal instability conditions.

The impact of this multiscale interaction is clearly reflected in the rainfall observations. As shown in Fig. 14, several areas in Bali experienced daily rainfall exceeding 100 mm/day, which falls into the extreme rainfall category. The spatial distribution of rainfall indicates that regions affected by strong moisture convergence and persistent convective activity correspond well with areas of highest rainfall intensity.

This agreement between atmospheric conditions and observed rainfall confirms that the interaction between large-scale (MJO), regional (moisture transport and convergence), and local (convective processes) mechanisms directly controlled the intensity and distribution of the extreme rainfall event. Therefore, this study highlights that multiscale coupling is a key mechanism in extreme rainfall events over the Maritime Continent, where the linkage between atmospheric dynamics and observed precipitation becomes essential for understanding and predicting high-impact weather events.

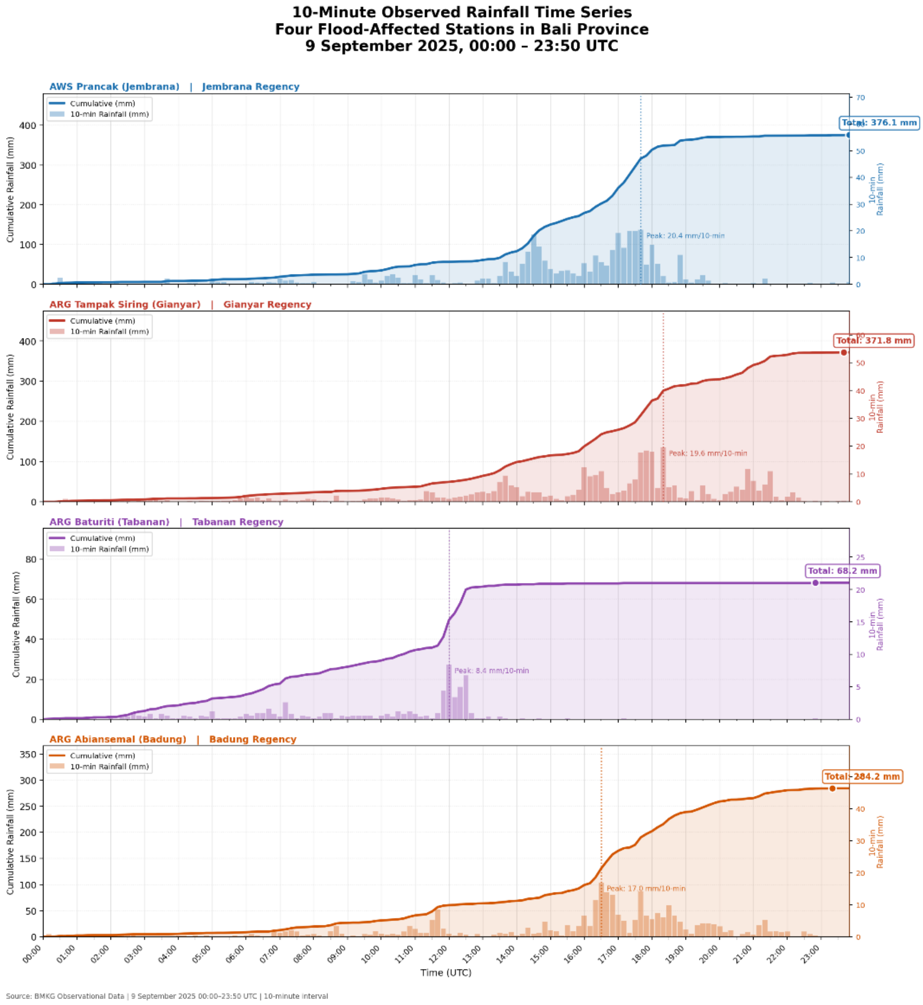

Fig. 14 Spatial distribution of daily rainfall over Bali on 9 September 2025

4. CONCLUSION

This study demonstrates that the extreme rainfall event in Bali on 9 September 2025 was primarily driven by the interaction of atmospheric processes across multiple scales. At the global scale, ENSO and IOD were in neutral conditions, indicating a limited influence from interannual variability. However, the presence of an active Madden–Julian Oscillation (MJO) played a significant role in enhancing large-scale convection over the Maritime Continent.

At the regional scale, favorable conditions such as positive sea surface temperature anomalies, low-level moisture convergence, and enhanced moisture transport contributed to the development of upward motion and sustained convective activity. At the local scale, deep convective clouds were observed, although atmospheric instability was relatively weak, suggesting that dynamic forcing was more dominant than thermodynamic factors in triggering the extreme rainfall.

These findings highlight the importance of multiscale interactions in controlling extreme rainfall events in tropical regions. In particular, strong intraseasonal variability such as the MJO, combined with regional atmospheric dynamics, can produce extreme rainfall even under marginal instability conditions.

From a practical perspective, this study suggests that early warning systems in Indonesia should not rely solely on traditional indicators such as local instability indices, but also incorporate large-scale and intraseasonal signals, especially MJO activity. Integrating these factors into operational forecasting could improve the accuracy of extreme weather predictions and support more effective disaster risk reduction strategies.

REFERENCE

[1] E. Aldrian and R. D. Susanto, "Identification of three dominant rainfall regions within Indonesia and their relationship to sea surface temperature," *Int. J. Climatol.*, vol. 23, no. 12, pp. 1435–1452, 2003, doi: 10.1002/joc.950.

[2] S. Supari, F. Tangang, E. Salimun, E. Aldrian, A. Sopaheluwakan, and L. Juneng, "ENSO modulation of seasonal rainfall and extremes in Indonesia," *Clim. Dyn.*, vol. 51, pp. 255–271, 2018, doi: 10.1007/s00382-017-3939-5.

[3] A. R. As-syakur, T. Tanaka, T. Osawa, and M. S. Mahendra, "Indonesian rainfall variability observation using TRMM data: The impacts of ENSO and IOD," *Int. J. Climatol.*, vol. 34, no. 5, pp. 1568–1579, 2014, doi: 10.1002/joc.3799.

[4] M. C. Wheeler and H. H. Hendon, "An all-season real-time multivariate MJO index: Development of an index for monitoring and prediction," *Mon. Weather Rev.*, vol. 132, no. 8, pp. 1917–1932, 2004, doi: 10.1175/1520-0493(2004)132<1917:AARMMI>2.0.CO;2.

[5] S. C. Peatman, J. Schwendike, and C. E. Birch, "A local-to-large scale view of Maritime Continent rainfall: Control by ENSO, MJO, and equatorial waves," *J. Climate*, vol. 34, no. 22, pp. 1–20, 2021. [Online]. Available: https://journals.ametsoc.org/view/journals/clim/34/22/JCLI-D-21-0263.1.xml

[6] C. P. Chang, Z. Wang, J. McBride, and C. H. Liu, "Annual cycle of Southeast Asia–Maritime Continent rainfall and the asymmetric monsoon transition," *J. Climate*, vol. 17, no. 11, pp. 2205–2223, 2004, doi: 10.1175/1520-0442(2004)017<2205:ACOSAM>2.0.CO;2.

[7] S. W. Lubis, S. Hagos, and E. Hermawan, "Record-breaking precipitation in Indonesia's capital of Jakarta in early January 2020 linked to the Madden–Julian Oscillation," *Geophys. Res. Lett.*, vol. 49, no. 24, 2022, doi: 10.1029/2022GL101513.

[8] M. Mughozali et al., "Analysis of cloud-top temperature for identification of convective clouds using Himawari-8 satellite data," *J. Remote Sens.*, 2017.

[9] COMET Program, "Convective instability indices (CAPE, K-Index, Total Totals)," UCAR MetEd, 2013. [Online]. Available: https://www.meted.ucar.edu

[10] P. Chen et al., "Monsoonal extreme rainfall in Southeast Asia: A review," *Water*, vol. 17, no. 1, 2024. [Online]. Available: https://www.mdpi.com/2073-4441/17/1/5

[11] D. Satiadi, A. Purwaningsih, and W. Harjupa, "Impacts of MJO phenomena on diurnal cycle of local convection, moisture convergence, and rainfall," *Meteorol. Atmos. Phys.*, 2023, doi: 10.1007/s00703-023-00979-w.

[12] M. N. Islam, H. Uyeda, and T. Terao, "Diurnal variations of cloud activity and rainfall in the tropical region," *Atmos. Res.*, vol. 209, pp. 1–13, 2018, doi: 10.1016/j.atmosres.2018.03.010.

[13] J. Y. Lee, "Seasonal prediction and variability of the Maritime Continent climate," *Clim. Dyn.*, vol. 45, pp. 1–15, 2015, doi: 10.1007/s00382-015-2671-7.

[14] X. Li, R. Lu, G. Chen, and R. Chen, "Western North Pacific tropical cyclones suppress Maritime Continent rainfall," *npj Clim. Atmos. Sci.*, 2024, doi: 10.1038/s41612-024-00810-2.

[15] D. S. Permana et al., "The role of tropical waves in the genesis of extreme weather over the Maritime Continent," *Nat. Commun.*, 2023, doi: 10.1038/s41467-023-36498-w.

[16] Risyanto et al., "Southerly surge impact on rainfall patterns in Southern Indonesia during MJO events," *Atmosphere*, vol. 15, no. 7, 2024. [Online]. Available: https://www.mdpi.com/2073-4433/15/7/840

[17] Ferrett, S., Methven, J., and Woolnough, S. J., "Hybrid dynamical–statistical forecasts of rainfall risk in Southeast Asia dependent on equatorial waves," *Mon. Weather Rev.*, 2023.

Journal of Computation Physics and Earth Science
ISSN: 2776-2521 (online)
Volume 6, Number 1, April 2026, Page 44 - 51
https://journal.physan.org/index.php/jocpes/index

Water Balance Analysis for Food Estate Program in Gunung Mas Regency, Central Kalimantan, Indonesia

Muhammad Aulia Zikri[1], Avrionesti[2]
[1]Meteorology Undergraduate Student Program, Indonesia State College of Meteorology Climatology, and Geophysics
[2]Meteorology Department, Indonesia State College of Meteorology Climatology, and Geophysics

Article Info

Article history:

Received March 31, 2026
Revised April 2, 2026
Accepted April 6, 2026

Keywords:

Water balance
Precipitation
Food estate
Evapotranspiration
Water management

A B S T R A C T

The implementation of food estate programs aimed at national food security requires comprehensive environmental considerations, particularly regarding soil conditions and water availability. This study employs the Thornthwaite-Mather method to model the water balance based on precipitation, air temperature, and soil characteristics. Analysis of climatological data from 2004 to 2023 reveals that Gunung Mas Regency, Central Kalimantan, maintains abundant groundwater availability throughout the year, with monthly percentages consistently reaching 100%. Average monthly temperatures range from 25.5°C to 26°C, while monthly rainfall varies significantly between 147 and 556 mm. According to the Oldeman classification, the region falls into category B2, characterized by nine wet months and fewer than three dry months. Land suitability evaluations indicate that the region is highly compatible with wetland-based cultivation, with optimal planting periods from November to January. Corn is suitable for cultivation between April and May. Conversely, the results suggest that cassava is less suitable for large-scale development in this region. This incompatibility stems from the persistent water surplus and high rainfall, which conflict with cassava's biological requirement for well-drained, drier upland conditions.

Corresponden Author:

Muhammad Aulia Zikri,
Meteorology Undergraduate Program
Tangerang, Indonesia
Email: auliazikri@stmkg.ac.id

1. INTRODUCTION

Indonesia is an archipelagic nation possessing approximately 188.2 million hectares of dry land and swamps [1]. Indonesia holds the largest swamp area in Southeast Asia, covering 33 million hectares [2]. Approximately 13.4–14.9 million hectares of these wetlands consist of peatlands, with 4.54 million hectares distributed across Kalimantan Island [3]. These peatlands serve as vital global climate regulators due to their immense capacity for carbon sequestration and storage [4]. The hydrological stability of these ecosystems is essential for maintaining regional water cycles and preventing land degradation [5].

In response to the economic downturn triggered by the COVID-19 pandemic in 2020, the Indonesian government initiated several National Economic Recovery (PEN) programs. A key strategy involved the development of "food estates" to bolster long-term economic and food resilience [6]. A food estate is defined as large-scale food crop cultivation (>25 ha) utilizing an industrial system integrated with modern technology, capital, and sustainable management [7]. This program aims to establish rural-based agribusinesses by empowering local communities as the foundation for regional growth. The central government has designated forest areas for this program, specifically in Central Kalimantan Province [8]. Development here focuses on rice commodities managed by the Ministry of Agriculture and cassava commodities overseen by the Ministry of Defense [9], [10]. However, the implementation has faced several hydrological challenges, including an expansion of flood-prone areas [11]. Such flooding often results from land-use changes that alter the natural catchment characteristics [12].

In the context of flooding and agricultural productivity, water availability is a critical factor. Within the hydrological cycle, the water volume in a specific location is determined by the balance of inflows and outflows over time, a concept known as the water balance. According to Sosrodarsono and Takeda [13], water balance represents the fundamental relationship between inflow and outflow, which is an absolute necessity for plant physiological processes. This balance is influenced by precipitation, evapotranspiration, and soil physical characteristics, which collectively indicate periods of water surplus or deficit [14], [15]. A significant imbalance can lead to severe agricultural disruptions, such as seasonal shifts that cause delayed planting, altered harvesting patterns, and potential crop failure [16].

To assess the hydrological state of a region, precise water balance calculations are required. The Thornthwaite-Mather (TM) method is widely recognized by experts for this purpose. This method is preferred because it requires relatively minimal data inputs while maintaining high predictive accuracy [14], [17], [18]. Previous studies by Pramono and Adi [19], demonstrated that TM-based predictions align closely with empirical field measurements. Similarly, research in India confirmed that the TM method effectively predicts potential evapotranspiration (PET) across diverse observation stations [18]. Consequently, this method remains a robust tool for regional hydrological assessment in data-scarce environments [20]. This study analyzes the water balance conditions in Gunung Mas Regency to evaluate its suitability for the food estate program from a hydrological perspective. Specifically, the research examines groundwater availability and potential evapotranspiration values to determine the viability of various agricultural commodities.

2. RESEARCH METHOD

2.1. Study Area and Data Sources

The research was conducted in Gunung Mas Regency, Central Kalimantan Province. Geographically, the area is located between 0°18’00’’ – 01°40’30” S and 113°01’00″ – 114°01’00’’ E. The region is traversed by three major river branches, the Miri, Rungan, and Manuhing, all of which flow into the Kahayan River, with an estimated total surface flow of 90 billion m3/year [21].

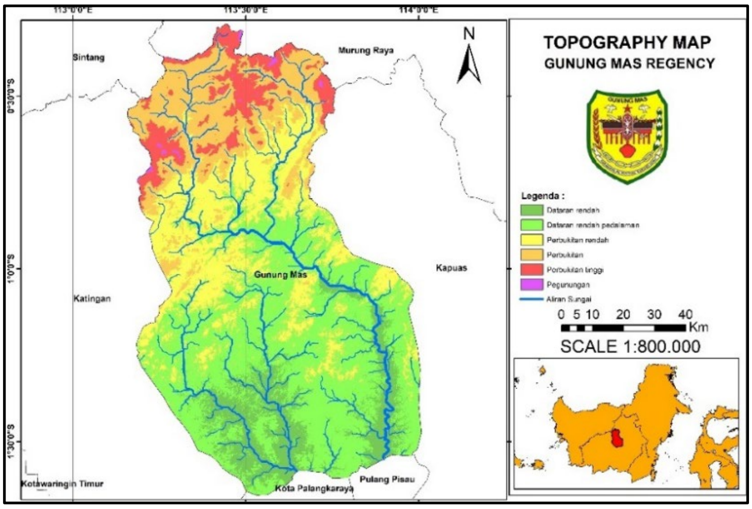

Fig. 1 Research the map area

This study utilized the following datasets:

a. Precipitation Data: Monthly reanalysis data (2004–2023) obtained from the Center for Hydrometeorology and Remote Sensing (CHRS) in TIFF format, with a spatial resolution of 0.04° x 0.04° (~4 km).
b. Air Temperature Data: Monthly reanalysis data (2004–2023) from Copernicus (ERA5-Land) in NetCDF format, with a spatial resolution of 0.1° x 0.1° (~11 km). The use of reanalysis data is justified in regions with limited ground-based observation stations [22].
c. Soil Properties: Field Capacity (FC) and Permanent Wilting Point (PWP) values were sourced from secondary data provided by the Water Resource Utilization Implementation [23]. For Gunung Mas, the FC is estimated at 74.2 and PWP at 20.4.
d. Crop Coefficients (Kc): The studied commodities (rice, corn, and cassava) were assigned Kc values of 1.13, 0.79, and 0.5, respectively [24], [25], [26].

2.2. Data Processing and Water Balance Modelling

The groundwater balance was modelled using the Thornthwaite-Mather method (1957) [27]. Air temperature data were used to calculate the Heat Index (I) and Potential Evapotranspiration (PET). The procedure involved the following stages:

a. Calculating Potential Evapotranspiration
   a) For average temperatures < 26.5 °C

$$ETP = 1{,}6\left(\frac{T}{I}\right)a \quad (1)$$

   b) For average temperatures ≥ 26.5 °C

$$ETP = -4{,}33 \times 10^{-2}\,T^2 + 3{,}2244\,T - 41{,}545 \quad (2)$$

   Notes:

$$a = 6{,}75 \times 10^{-7}\,I^3 - 7{,}71 \times 10^{-5}\,I^2 + 1{,}792 \times 10^{-2}\,I + 0{,}49239 \quad (3)$$

$$I\,(yearly\ heat\ index) = \sum_{i=1}^{12}\left(\frac{T_i}{5}\right)^{1{,}5114} \quad (4)$$

b. PET Correction

   The initial PET was adjusted based on the latitude and the number of days in each month to account for variations in day length [28].

$$ETP_{correction}(mm) = ETP\left(\frac{\theta}{30}\right)\left(\frac{h}{12}\right) \times 10 \quad (5)$$

c. Precipitation and PET Difference:

   The difference between precipitation (P) and PET (P - PET) was calculated to identify periods of moisture surplus or deficit.

d. Accumulated Potential Water Loss (APWL):
   a) If CH ≥ETP, then APWL = 0
   b) If CH < ETP, then APWL = ∑ (P-PET)

e. Groundwater Content (KAT):

   KAT is the maximum capacity of water that the soil can store. It is influenced by space capacity (the amount of water that stays in the soil after the water flows due to the earth's gravity and the dew point, when plants cannot extract water from the soil), empirically formulated by Mashudi [29].

   a) If APWL ≠ 0:

$$KAT = TLP \times \left[\left(1{,}00041 - \frac{1{,}07381}{AT}\right)\right]^{|APWL|} \times AT \quad (6)$$

   b) If APWL = 0

$$KAT_i = KAT_{i-1} + CH - ETP \quad (7)$$

   c) If KAT gas reached KL, then:

$$KAT = KL \quad (8)$$

f. Calculate dKAT with the formula:

$$dKAT = KAT_{i-1} - KAT_i \quad (9)$$

g. Calculate actual evapotranspiration (AET), with the formula:
   a) If P > ETP, then AET = ETP
   b) If P ≤ ETP, then AET = CH + |dKAT|

h. Calculate water balance surplus or deficits, with the formula:

$$surplus = CH - ETP + dKAT \quad (10)$$

$$deficit = ETP - AET \quad (11)$$

i. Calculate Groundwater Availability (ATS), with the formula:

$$ATS = \frac{KAT - TLP}{KL - TLP} \times 100\% \quad (12)$$

   ATS values are categorized into five (5) parts:
   a) Critically Low, if ATS < 10%
   b) Low, if 10% < ATS < 40%
   c) Moderate, if 40% < ATS < 60%
   d) Sufficient, if 60% < ATS < 90%
   e) Abundant, if ATS > 90%

2.3. Land Appropriation for Rice, Corn, and Cassava Commodities

The assessment of land appropriation for the Food Estate program requires a detailed understanding of the agro-climate requirements for rice, corn, and cassava. Rice remains the most strategic food commodity in Indonesia, serving as the primary staple for the majority of the population. This crop exhibits broad adaptability across altitudes ranging from 0 to 1,500 meters above sea level (masl). Most rice varieties thrive in high-humidity environments with consistent monthly precipitation exceeding 200 mm, ideally distributed over at least a four-month growing season. Furthermore, rice development requires ambient temperatures between 19°C and 27°C, with an optimal physiological threshold at 23°C [15]. Conversely, corn serves as a vital complementary carbohydrate source with a typical cultivation cycle of 80 to 150 days. Unlike rice, corn is better suited for drier environments and is susceptible to physiological stress under high-humidity conditions. The ideal precipitation for corn ranges from 85 to 200 mm per month with uniform distribution; moisture is particularly critical during the germination and flowering phases, which typically occur at the end of the rainy season, to ensure maximum solar radiation for fruit formation at an ideal temperature of 25°C [30].

Climate significantly dictates both the quantity and starch quality of cassava growth. During the initial 0 to 90 days, the ideal precipitation for this crop is 150–200 mm/month, which increases to 250–300 mm/month during the active growth phase (90 to 280 days), before tapering off to 100–150 mm/month as it approaches harvest [31]. In addition to requiring a minimum temperature of 10°C and optimal relative humidity of 60–65%, cassava is highly dependent on friable, non-clayey soil characteristics to support tuber expansion. Such soils must be rich in organic matter with an ideal pH of approximately 5.8, and the crop is best suited for altitudes between 10 and 500 masl [32]. Effective soil drainage is a critical limiting factor, as cassava is highly sensitive to waterlogged or anaerobic soil conditions. To determine the compatibility of the land with these commodities, this study employs the Oldeman and Frere climate classification [33], which is specifically designed for rain-fed agriculture. This system categorizes climates based on the frequency of consecutive Wet Months (WM), defined by rainfall > 200 mm, and Dry Months (DM), defined by rainfall < 100 mm. This methodology provides a robust framework for determining potential cropping intensity based on natural water availability in tropical regions [34].

Table 1. Oldeman climate classification

Main Type	WM Total
A	> 9
B	7 – 9
C	5 – 6
D	3 – 4
E	< 3

Sub-Division	DM Total
1	< 2
2	2 – 3
3	4 – 6
4	> 6

3. RESULT AND DISCUSSION

The comprehensive evaluation of the hydrological cycle in Gunung Mas Regency provides a fundamental baseline for assessing agricultural potential. As the water balance analysis consistently indicates a significant moisture surplus and high groundwater availability throughout the year, it is imperative to examine how these specific hydrological conditions align with the biological requirements of various food crops. Consequently, the following section evaluates the suitability of rice, corn, and cassava commodities within the context of the region's persistent water-rich environment and its implications for the proposed food estate development.

3.1. Water Balance Analysis

On the processing of precipitation data (CH) for 20 years (2004-2023), the average total CH of Gunung Mas Regency ranges from 147 to 556 mm/month. Global, regional, and local factors influence the magnitude of precipitation intensity at the research site. One is the valley/Gunungain wind because Gunung Mas Regency has a complex natural landscape from low to high plains. In addition, the research is located at the height of the river, resulting in the blockage of the movement of clouds by the mountains, which resulted in the accumulation of rain clouds due to wind movement. If this happens continuously, it will result in a high intensity of precipitation falling at the site of the study.

According to the Oldeman classification applied to the study site, there are nine wet months (BB) with CH ≥ 200mm, in January-May and September-December, accompanied by three wet months with 100 mm <

CH < 200 mm occurring in June-August. Evapotranspiration at the study site ranged from 112.1 mm to 128.5 mm, with the lowest total occurring in February and the highest in May. Precipitation and evaporation conditions in Gunung Mas Regency can be observed in the following table.

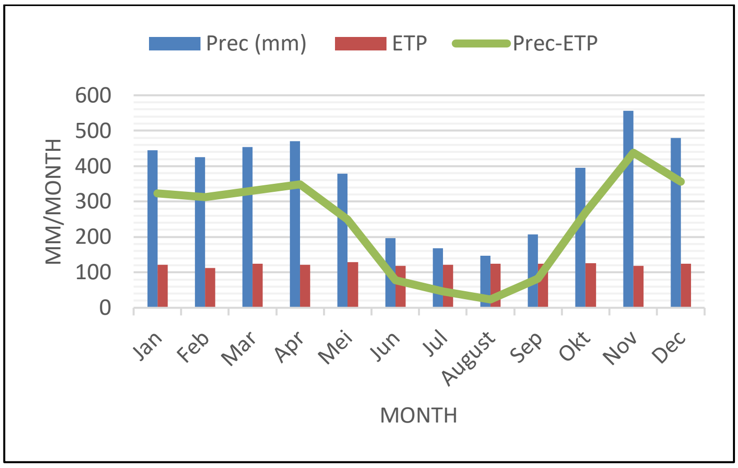

Fig. 2 Monthly ratio of precipitation, land evapotranspiration, and precipitation and land evaporation of Gunung Mas Regency in 2004-2023

The difference between soil evapotranspiration and precipitation was highest in November at 437.8 mm and lowest in August at 23.5 mm. In Table 2, there was no difference between the negative values of precipitation and evaporation of soil (in all CH> ETP months) during 2004-2023. The potential water loss for evaporation (APWL) in Gunung Mas Regency is relatively small and does not even occur. The amount of groundwater (AT) at the research site was obtained from the difference between the field's capacity and the plant's permanent dew point, which is 53.8 mm for Gunung Mas Regency.

This is due to more considerable precipitation when compared with the evapotranspiration of the soil, which occurred, so that the potential loss of water does not occur. This is in direct comparison with the value of dKAT, which is zero because KAT is the same each month. Since the amount of precipitation at the study site is greater than the potential evaporation at each month, then the actual value of evaporation is equal, so that ETP=ETA. This will be observed from the availability of groundwater (ATS), which reaches 100% each month, which indicates that water is sufficient to meet the land needs in Gunung Mas Regency each year.

Table 2. Oldeman climate classification

Month	P	ETP	P-ETP	APWL	KAT	dKAT	AET	Deficit	Surplus	ATS
Jan	445	122,1	323,2	0	74,2	0	122,1	0	323,2	100%
Feb	425	112,1	312,8	0	74,2	0	112,1	0	312,8	100%
Mar	454	123,9	329,9	0	74,2	0	123,9	0	329,9	100%
Apr	470	121,4	348,8	0	74,2	0	121,4	0	348,8	100%
Mei	378	128,5	249,6	0	74,2	0	128,5	0	249,6	100%
Jun	197	119	78,3	0	74,2	0	119	0	78,3	100%
Jul	168	121,3	46,5	0	74,2	0	121,3	0	46,5	100%
Agu	147	123,8	23,5	0	74,2	0	123,8	0	23,5	100%
Sep	207	125	81,6	0	74,2	0	125	0	81,6	100%
Okt	395	126,6	268,6	0	74,2	0	126,6	0	268,6	100%
Nov	556	118,3	437,8	0	74,2	0	118,3	0	437,8	100%
Dec	480	123,9	356,4	0	74,2	0	123,9	0	356,4	100%

3.2. Land Adequacy Analysis of Rice, Corn, and Cassava Commodities

Analysis of climatological data from 2004 to 2023 indicates that Gunung Mas Regency has a stable monthly air temperature range of 25.5°C to 26°C. The minimum thermal values were recorded in July, while the maximum peak occurred in September. Concurrently, the average monthly precipitation in the region varies significantly from 147 mm to 556 mm. According to the Oldeman climate classification, Gunung Mas Regency is categorized as Type B2 (based on 9 consecutive wet months). Within this agro-climatic framework, rice demonstrates high land suitability due to its tolerance for high moisture levels. Conversely, corn and cassava exhibit lower suitability levels. This is primarily due to persistent high-intensity rainfall throughout the year, which induces excessive soil moisture, a condition known to inhibit the physiological development of corn and the tuber formation of cassava, both of which require well-drained soil.

Table 3. Evapotranspiration values of soil and plants of rice, cassava, and corn

Month	Land ET_P	Rice ET_C	Cassava ET_C	Corn ET_C
January	122,1	138	61,1	96,5
February	112,1	126,6	56	88,5
March	123,9	140	62	97,9
April	121,4	137,2	60,7	95,9
May	128,5	145,2	64,3	101,5
June	119	134,4	59,5	94
July	121,3	137	60,6	95,8
August	123,8	139,9	61,9	97,8
September	125	141,3	62,5	98,8
Oktober	126,6	143	63,3	100
November	118,3	133,7	59,2	93,5
December	123,9	140	62	97,9

The calculation of crop-specific evapotranspiration (ETc) was performed by integrating potential evapotranspiration (ETp) with crop coefficients (ETc) derived from established literature [24], [26], [35]. As shown in Table 3, the ETc values for all three commodities reached their maximum in May, coinciding with the peak land ETp of 128.5 mm. During this peak period, the ETc for rice, cassava, and corn were 145.2 mm, 64.3 mm, and 101.5 mm, respectively. In contrast, the minimum ETc values occurred in February, corresponding to a land ETp of 112.1 mm, with ETc values of 126.6 mm for rice, 56 mm for cassava, and 88.5 mm for corn. These fluctuations underscore the significant influence of local meteorological parameters on the atmospheric water demand of each commodity.

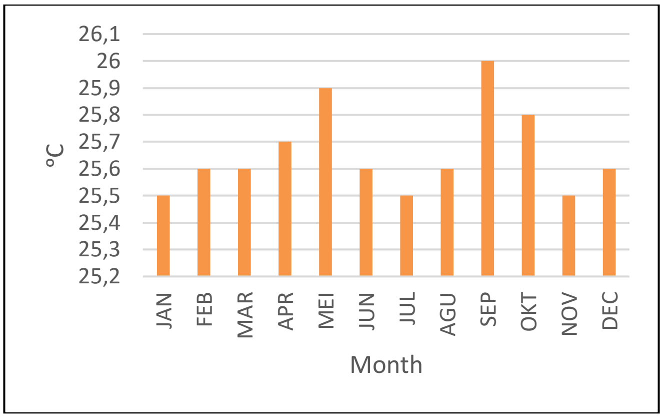

Fig. 3 Average monthly air temperature from 2004 to 2023

Figure 4 illustrates the monthly water surplus for each studied commodity alongside the general land water surplus. The analysis reveals that the surplus values for all crops follow a consistent seasonal pattern that aligns with the regional hydrological cycle. The maximum surplus for all commodities was observed in November, while the minimum occurred in August, coinciding with the peak and trough of the annual precipitation cycle. The higher surplus values for corn and cassava relative to their biological requirements are due to their lower water consumption (ETc) compared to wetland rice.

Regarding agricultural productivity, the persistent precipitation patterns in Gunung Mas Regency are highly suitable for wetland rice cultivation, as the continuous water availability ensures optimal irrigation throughout the growing season. However, for corn and cassava, the water availability is significantly over-abundant due to the region's high rainfall. This excessive moisture can lead to suboptimal growth conditions; for instance, over-saturated soils often result in root rot, reduced starch quality in tubers, and a higher prevalence of water-borne plant diseases. Consequently, while the region possesses a robust hydrological surplus, the cultivation of upland crops like corn and cassava requires strategic drainage management to mitigate the risks associated with excessive soil moisture.

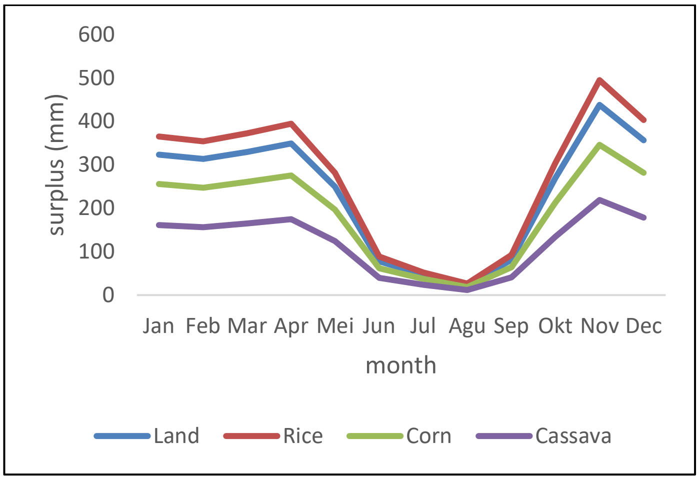

Fig. 4 Average monthly groundwater availability 2004-2023

4. CONCLUSION

Based on the hydrological analysis and water balance modeling, Gunung Mas Regency exhibits an abundant and persistent groundwater surplus, with availability consistently reaching 100% throughout the year. Remote sensing data indicate that monthly precipitation ranges from 147 mm to 556 mm, complemented by stable average temperatures between 25.5°C and 26°C. The region's complex topography further intensifies these hydrological characteristics, creating an environment that is highly conducive to wetland-based agriculture. Specifically, the hydrological profile of the study area is ideally suited for rice cultivation across all seasons, with the optimal planting window occurring from November to January.

In contrast, the persistent water surplus presents a significant limiting factor for upland crops such as corn and cassava. Corn cultivation is only deemed suitable during the transition at the end of the peak wet season (April–May), allowing the harvest to coincide with the relatively lower rainfall period from June to August. Cassava, however, is categorized as less suitable for large-scale development in this region due to its physiological intolerance to the high precipitation and saturated soil conditions identified in the water balance profile.

REFERENCE

[1] A. Nur Izzati, B. Liku Gustiawati, D. Rizal, and Y. Saputra, "Proyek Food Estate Pada Lahan Eks Pengembangan Lahan Gambut di Kalimantan Tengah: Perlu Atau Tidak?," *Ecoprofit: Sustainable and Environment Business*, vol. 1, no. 1, pp. 58–75, 2023, [Online]. Available: https://journal-iasssf.com/index.php/ECOPROFIT

[2] Y. Chadirin, S. K. Saptomo, . Rudiyanto, and K. Osawa, "Environmental Biophysics and CO2 Emission in Bare Peatland for Sustainable Biomass Production," *Jurnal Ilmu Pertanian Indonesia (JIPI)*, vol. 21, no. 2, pp. 146–151, Aug. 2016, doi: 10.18343/jipi.21.2.146.

[3] M. Anda *et al.*, "Revisiting Tropical Peatlands in Indonesia: Semi-Detailed Mapping, Extent and Depth Distribution Assessment," *Geoderma*, vol. 402, p. 115235, Feb. 2021, doi: https://doi.org/10.1016/j.geoderma.2021.115235.

[4] M. R. P. Maulana, H. Herawati, and K. Kartini, "Pengelolaan Lahan Gambut Secara Partisipatif Studi Kasus Desa Wajok Hilir," *JeLAST: Jurnal Teknik Kelautan, PWK, Sipil, dan Tambang*, vol. 8, no. 1, pp. 1–7, 2021, [Online]. Available: https://jurnal.untan.ac.id/index.php/JMHMS/article/view/45833

[5] J. H. M. Wösten and others, "Hydrology of tropical peatlands and its impact on land subsidence and greenhouse gas emissions," *J. Hydrol. (Amst).*, vol. 349, no. 1–2, pp. 108–117, 2008, doi: 10.1016/j.jhydrol.2007.10.051.

[6] A. Wirapranatha, Y. Sutrasna, and L. Simbolon, "Strategi Pengembangan Food Estate Dalam Pemulihan Ekonomi Nasional Food Estate Development Strategy in National Economic Recovery," *Jurnal Ekonomi Pertahanan*, vol. 8, no. 1, pp. 1–13, 2022.

[7] Kementerian Pertanian, *Buku Pintar Pengembangan Food Estate*. 2010.

[8] K. P. Ayu, "Kebijakan Perubahan Lahan Dalam Pembangunan Food Estate di Kalimantan Tengah," *JISPAR, Jurnal Ilmu Sosial, Politik dan Pemerintahan*, vol. 11, no. 1, pp. 24–36, 2022.

[9] L. Lasminingrat and D. Efriza, "The Development of National Food Estate: The Indonesian Food Crisis Anticipation Strategy," *Jurnal Pertahanan & Bela Negara*, vol. 10, no. 3, pp. 229–249, 2020, doi: https://doi.org/10.33172/jpbh.v10i3.1110.

[10] A. M. Surbakti, M. Rafli Gebrena, and L. M. Jannah, "Inefektivitas Program Food Estate Kabupaten Gunung Mas: Sebuah Analisis Diagram Pohon," *Jurnal Ilmiah Publiks*, vol. 9, no. 2, pp. 480–489, 2023.

[11] CNN Indonesia, "LBH: Food Estate Gunung Mas Kalteng berpotensi Perluas Wilayah banjir," Nasional. Accessed: Mar. 14, 2024. [Online]. Available: https://www.cnnindonesia.com/nasional/20211118184645-20-723161/lbh-food-estate-gunung-mas-kalteng-berpotensi-perluas-wilayah-banjir

[12] M. L. Tan and others, "Impacts of land use and land cover changes on hydrological processes in tropical river basins," *Environ. Earth Sci.*, vol. 74, pp. 5505–5524, 2015, doi: 10.1007/s12665-015-4562-y.

[13] S. Sosrodarsono and K. Takeda, *Hidrologi untuk Pengairan, Cetakan Kesepuluh*. Pradnya Paramita, Jakarta, 2006.

[14] A. A. Nasir and S. Effendy, "Konsep Neraca Air Untuk Penentuan Pola Tanam," *Kapita Selekta Agroklimat*, 2000.

[15] J. A. I. Paski, G. I. S. L. Faski, and D. A. S. Pertiwi, "Analisis Neraca Air Lahan untuk Tanaman Padi dan Jagung Di Kota Bengkulu," *Jurnal Ilmu Lingkungan*, vol. 15, no. 2, pp. 83–89, Jan. 2017, doi: 10.14710/jil.15.2.83-89.

[16] Musyadik, A. W. Nugroho, L. Sabaruddin, L. Baco Sudia, and M. Nur, "Spatial Analysis of Water Balance Distribution For Simulation of Timing and Patterns of Rice and Crop Planting in The Region of Type D Rainfall in The South Konawe Regency," *Desember*, vol. 35, no. 2, pp. 287–300, 2023, doi: https://doi.org/10.24246/agric.2023.v35.i2.p287-300.

[17] R. N. Adi, E. Savitri, P. B. Putra, and Y. Indrajaya, "Water Balance of Various Peatland Typologies in Central Kalimantan," in *IOP Conference Series: Earth and Environmental Science*, IOP Publishing Ltd, Oct. 2021, pp. 1–10. doi: 10.1088/1755-1315/874/1/012002.

[18] M. Khandelwal and V. Pandey, "Comparison of PET Computed by Various Methods in Different Agroclimatic Stations of Gujarat State," *Journal of Agrometeorology (Special issue-Part 2)*, pp. 439–443, 2008, Accessed: Mar. 14, 2024. [Online]. Available: https://www.researchgate.net/publication/278331664_Comparison_of_PET_Computed_by_Various_Methods_in_Different_Agroclimatic_Stations_of_Gujarat_State

[19] I. B. Pramono and R. N. Adi, "Perbandingan Hasil Estimasi Potensi Air Bulanan dan Hasil Pengukuran Langsung di Sub DAS Wuryantoro, Wonogiri," *Jurnal Penelitian Hutan dan ...*, 2010, doi: https://dx.doi.org/10.20886/jphka.2010.7.2.127-137.

[20] P. Dobriyal, A. Qureshi, R. Badola, and S. A. Hussain, "A review of the methods available for estimating soil moisture and its implications for water resource management," *J. Hydrol. (Amst).*, vol. 554, pp. 103–111, 2017, doi: 10.1016/j.jhydrol.2017.08.051.

[21] Dinas Pekerjaan Umum Kabupaten Gunung Mas, *Rencana Induk Pengembangan Sistem Penyediaan Air Minum Kabupaten Gunung Mas Provinsi Kalimantan Tengah Tahun 2015-2030*, no. 109. 2015.

[22] H. Hersbach *et al.*, "The ERA5 global reanalysis," *Quarterly Journal of the Royal Meteorological Society*, vol. 146, no. 730, pp. 1999–2049, 2020.

[23] M. A. Firmansyah, "Teori dan Praktik Analisis Neraca Air Untuk Menunjang Tugas Penyuluh Pertanian di Kalimantan Tengah," 2010.

[24] F. M. Barung and W. J. Pattipeilohy, "Neraca Air Lahan dan Tanaman Padi di Kabupaten Manokwari Selatan, Papua Barat pada Tahun 2019," *Buletin GAW Bariri (BGB)*, vol. 1, no. 1, pp. 29–36, 2020.

[25] S. Dwiratna and E. Suryadi, "Penjadwalan Irigasi Menggunakan Neraca Air Harian Pada Budidaya Ubi Jalar (Ipomea Batatas L.) Varietas Rancing," *Jurnal Agrotek Indonesia*, vol. 4, no. 1, Jan. 2019, doi: 10.33661/jai.v4i1.1857.

[26] Seeman and et al, "The Hydrology Cycle," in *Bahan Ajar Sekolah Tinggi Meteorologi Klimatologi dan Geofisika*, 1979.

[27] C. W. Thornthwaite and J. R. Mather, "Instructions and Tables for Computing Potential Evapotranspiration and The Water Balance," *Drexel Laboratory of Climatology Institute of Technology*, vol. X, no. 3, pp. 185–243, 1957.

[28] R. Rusnam and N. R. Yanti, "Potential Evapotranspiration Uses Thornthwaite Method to The Water Balance in Padang City," in *IOP Conference Series: Earth and Environmental Science*, IOP Publishing Ltd, May 2021, pp. 1–6. doi: 10.1088/1755-1315/757/1/012041.

[29] I. Mashudi, M. Anwar, and F. F. Adji, "Pemanfaatan Data Satelit Tropical Rainfall Measuring Mission (TRMM) Untuk Pemetaan Zona Agroklimat Neraca Air Lahan di Kalimantan Tengah," *Journal of Environment and Management*, vol. 2, no. 1, pp. 11–25, Feb. 2021, doi: 10.37304/jem.v2i1.2655.

[30] B. Rasyid, S. S. R. Samosir, and F. Sutomo, "Respon Tanaman Jagung (Zea mays) pada Berbagai Regim air Tanah dan Pemberian Pupuk Nitrogen," *Prosiding Pekan Serealia Nasional*, pp. 26–34, 2010.

[31] N. Saleh, D. Harnowo, and I. J. M. Mejaya, *Penyakit Penyakit Penting Pada Ubi Kayu: Deskripsi, Bioekologi dan Pengendaliannya*. 2016.

[32] E. Wahyurini and D. Sugandini, *Budidaya dan Aneka Olahan Singkong*. eprints.upnyk.ac.id, 2021. [Online]. Available: https://eprints.upnyk.ac.id/34905/1/BUKU%20Budidaya%20dan%20Aneka%20Olahan%20Singkong.pdf

[33] R. G. Risamasu, S. Laimeheriwa, E. L. Madubun, and M. Luhukay, "Analisis Perubahan Curah Hujan dan Pemetaan Zona Agroklimat Oldeman Pulau Seram Provinsi Maluku," *Innovative: Journal of Social Science Research*, vol. 3, no. 3, pp. 1010–1024, 2023.

[34] L. R. Oldeman, *An agro-climatic classification for evaluation of cropping systems in Southeast Asia*, no. 4. in IRRI Research Paper Series. Los Baños, Philippines: International Rice Research Institute (IRRI), 1975.

[35] D. N.P.S., G. Nawawi, and C. Asdak, "Analisis Curah Hujan dan Aplikasinya dalam Penetapan Jadwal dan Pola Tanam Pertanian Lahan Kering di Kabupaten Bandung," *Bionatura*, vol. 15, 2013, [Online]. Available: https://api.semanticscholar.org/CorpusID:87649324

Journal of Computation Physics and Earth Science
ISSN: 2776-2521 (online)
Volume 6, Number 1, April 2026, Page 52 - 58
https://journal.physan.org/index.php/jocpes/index

The Role of Geoelectrics in Landslide Mitigation Strategies in Malang City

Rayhan Irfan Hielmy[1], Muhammad Abdul Aziz[2], Bambang Sulistyo[3]
[1,2,3]Department of Geophysics, College of Meteorology Climatology and Geophysics

Article Info

Article history:

Received March 31, 2026
Revised April 5, 2026
Accepted April 8, 2026

Keywords:

Geoelectric resistivity,
Landslides,
Disaster mitigation,
Malang City

A B S T R A C T

The city of Malang faces a significant risk of landslides due to rapid population growth and increasingly dense residential development. To address this pressing issue, it is highly important to implement effective and integrated mitigation strategies. One reliable method that can be used in landslide disaster mitigation is the geoelectric resistivity method. The methodology employed in this research is a literature review, conducted by systematically collecting and analyzing data from various relevant sources. This paper comprehensively discusses the vital role of geoelectric methods in landslide mitigation strategies specifically in the city of Malang. The fundamental working principles of the geoelectric resistivity method are clearly explained, including the detailed analysis of geoelectric resistivity data. Additionally, this article also discusses practical landslide mitigation strategies and how using geoelectric methods can help identify potential landslide risks. In this study, geoelectric data collection was carried out at several locations in the city of Malang, and the results were directly used to plan effective disaster mitigation actions.

Corresponden Author:

Rayhan Irfan Hielmy,
Department of Geophysics, College of Meteorology Climatology and Geophysics
Tangerang, Indonesia
Email: rayhanirfanhielmy@stmkg.ac.id

1. INTRODUCTION

Malang City ranks 17th in population among the 94 registered cities in Indonesia [1]. The population in Malang City continues to grow, rising from 843,810 to 846,126 people between 2020 and 2022, based on demographic data from the Malang City Central Bureau of Statistics [2]. This significant population increase and the limited available land cause land prices in the city center to rise. The economic and social situation in Malang City makes low-income residents choose to settle in suburban areas, especially in regions close to riverbanks.

The geological structure in Malang City is very diverse, with a wide highland in the south, a fertile northern part, a highland in the east, and a very vast highland in the west [3]. Malang City also has four different soil types, namely blackish-gray alluvial, brown mediterranean, a reddish-brown latosol and greyish-brown association, and a brown and grey humus andosol association. This difference in geological structure provides a variety of environmental conditions in this city. Besides having a diverse geological structure, Malang City also faces challenges caused by population growth and increasingly dense settlements in riverbank areas.

This situation leads to a decrease in the availability of riverbank areas as conservation zones and open spaces, as well as an increase in environmental degradation and disaster risks, especially landslides [4]. Data from the Malang City BPBD Operations Control Center (Pusdalops) in 2017 showed that there were 74 landslide events during that year, causing significant losses in terms of both casualties and material damage. Therefore, understanding the geological structure and environmental conditions of Malang City is very important to overcome this challenge. Landslides can be defined as the displacement of slope-forming materials, whether original rocks or fill materials, that move downwards and outwards from the slope.

One factor that strongly influences the occurrence of landslides is the slip surface, which is the plane that becomes the base for soil mass movement. Therefore, the analysis of the slip surface and soil structure needs to be done as an initial step in landslide disaster mitigation. Identifying the characteristics of the subsurface slip surface using the geoelectric resistivity method has proven to be very effective in mapping landslide-prone zones with high precision at specific depths [5]. The slip surface itself is a watertight and slippery surface, generally consisting of clay layers [6].

To reduce the risk of landslide disasters, the community must take preparedness actions by understanding and implementing various available systems and measures. These preparedness actions include identifying available resources, early warning systems, rescue actions, community socialization, coordination with related agencies, and so on. The importance of this disaster education effort is supported by field evaluations proving that structured mitigation socialization can significantly improve students' cognitive values and understanding regarding emergency preparedness in the school environment [7]. Therefore, it is important to identify areas that are potentially exposed to landslide hazards as a disaster mitigation effort [8].

To understand the geological structure that includes different soil types, we can use the geoelectric method to obtain information about the rock resistivity characteristics in the area. The geoelectric method can also be used to identify subsurface structures that might be related to landslide risks or other geotechnical problems. By obtaining information about rock resistivity, we can find out the zones that have low stability and have the potential to cause soil movement. This can help in determining mitigation steps and protection against natural disaster risks.

In determining fast and precise geophysics-based mitigation steps, computational efficiency is highly needed, similar to the use of a Python-based numerical algorithm to speed up the calculation of disaster decay time [9]. The reliability of automated phase picking is also important to detect hazard parameters proactively and in real-time [10]. The geoelectric resistivity method is one of the geophysical techniques that can be applied to determine the soil layer structure and detect the slip surface by studying the characteristics of electrical flow in the earth. This technique involves measuring potential, current, and electromagnetic fields that occur naturally or are caused by sending electrical currents into the earth.

The basic principle of the geoelectric method is to send an electrical current into the ground surface through a pair of electrodes and measure the potential difference using another pair of electrodes. By measuring the potential difference and electrical current, the resistance value of the medium inside the earth being studied can be estimated. This method has the advantage of not damaging the environment, is relatively cheap, and is able to detect several meters of depth in the soil layer [11]. Another advantage of this method is its ability to map subsurface cross-sectional models in 2D and 3D, thus providing a comprehensive visualization regarding the weathered layer thickness that has the potential to become landslide material [12].

Previous research did not include landslide mitigation strategies, the principles of the geoelectric method, and the relationship between geological structures and landslides. In this paper, we combine various elements that were present in previous studies. The first objective of this writing is to find out the working principle of the geoelectric resistivity method in determining the soil layer structure and slip surface. The other objectives are to understand the benefits of this method in identifying potential landslide risks, planning effective mitigation, and understanding its potential and limitations as an alternative solution in Malang City.

2. RESEARCH METHOD

In the research regarding the geological characteristics of the area, geoelectric data collection was conducted by observing rock types at two different coordinates, namely 08°10'13.0" E 112°38'20.0" S and 08°10'14.6" E 112°38'18.2" S, with elevations of 367 and 368 meters above sea level, respectively, and recorded in Table 1 and Table 2. This observation was carried out by paying attention to the depth and rock resistivity in each of those layers. In addition, research was also conducted at a mini football field in Jatimulyo, Lowokwaru, Malang City, East Java, which has the coordinates 7°56'50.71" S 112°36'57.77" E. This mini football field has a size of 70m × 60m, but in this research, only a part of the field was used, namely five points with a distance of 10 meters between points.

Table 1. Observation data at coordinates 08°10'13.0" E 112°38'20.0" S, 368 MASL [13]

Depth (m)	Resistivity (Ωm)	Rock Type
0 – 2.57	36.96	Surface Soil
2.57 – 5.46	24.69	Tuff
5.46 – 8.19	17.90	Clay
8.19 – 29.37	92.79 – 109.17	Sand
29.37 – 63.74	15.76	Tuff
63.74 – 104.10	95.92	Sand

Table 2. Observation data at coordinates 08°10'14.6" E 112°38'18.2" S, 367 MASL [13]

Depth (m)	Resistivity (Ωm)	Rock Type
0 – 2.57	79.93	Surface Soil
2.50 – 11.44	23.94 – 46.35	Tuff
11.44 – 21.86	14.09	Clay
21.86 – 33.43	50.79	Sandy Silt
33.43 – 45.76	29.48	Tuff
45.76 – 91.92	294.97	Gravel

Table 3. Observation data at coordinates 7°56'50.46" S 112°36'56.41" E [14]

N	ρ (Rho)	h	d	Alt
1	9.698	0.9	0.9	-0.9
2	8.775	1.054	1.954	-1.9541
3	12.43	2.289	4.243	-4.2426
4	25.85	4.969	9.212	-9.2116
5	12.75	10.79	20	-20
6	21.42			

Table 4. Observation data at coordinates 7°56'50.27" S 112°36'56.60" E [14]

N	ρ (Rho)	h	d	Alt
1	10.46	0.9	0.9	-0.9
2	8.738	1.054	1.954	-1.9541
3	15.07	2.289	4.243	-4.2426
4	15.58	4.969	9.212	-9.2116
5	17.1	10.79	20	-20
6	19.84			

Table 5. Observation data at coordinates 7°56'50.05" S 112°36'56.82" E [14]

N	ρ (Rho)	h	d	Alt
1	10.52	0.9	0.9	-0.9
2	8.528	1.054	1.954	-1.9541
3	15.86	2.289	4.243	-4.2426
4	14.92	4.969	9.212	-9.2116
5	17.62	10.79	20	-20
6	19.53			

Table 6. Observation data at coordinates 7°56'49.83" S 112°36'57.00" E [14]

N	ρ (Rho)	h	d	Alt
1	9.845	0.9	0.9	-0.9
2	7.901	1.054	1.954	-1.9541
3	12.61	2.289	4.243	-4.2426
4	18.35	4.969	9.212	-9.2116
5	14.95	10.79	20	-20
6	10.1			

Table 7. Observation data at coordinates 7°56'49.57" S 112°36'57.21" E [14]

N	ρ (Rho)	h	d	Alt
1	9.825	0.9	0.9	-0.9
2	7.941	1.054	1.954	-1.9541
3	12.59	2.289	4.243	-4.2426
4	17.87	4.969	9.212	-9.2116
5	16.45	10.79	20	-20
6	9.095			

The methodology used in this research is a literature review. The research was conducted by collecting and analyzing data from various literature sources relevant to the research topic. The literature sources used include scientific journals, articles, books, and publications related to landslide mitigation, geological structures, and the geoelectric resistivity method. The first step in this methodology is identifying the research topic and understanding the background of the problem regarding the role of geoelectrics in landslide mitigation strategies in Malang City.

Then, the authors conducted a literature search using scientific databases and digital libraries to gather relevant sources. After collecting sufficient literature, the authors performed reading and analysis of each literature source. The data obtained from the literature were recorded and organized according to relevant subtopics, such as the working principles of the geoelectric resistivity method, geoelectric resistivity data analysis, and landslide mitigation strategies. Next, the authors evaluated and synthesized information from the collected literature to compile the discussion.

In this discussion, the authors explain in detail the working principle of the geoelectric resistivity method, including the use of tools and measurement techniques. In addition, the authors also analyze the geoelectric resistivity data obtained from previous research and explain how these data can be used to identify potential landslide risks. The results and discussion also include a discussion regarding landslide mitigation strategies in Malang City. The authors identify actions that can be taken in landslide disaster mitigation, including the identification of areas potentially affected by landslide hazards, early warning, and coordination with related agencies.

The authors also explain how the use of the geoelectric resistivity method can be an alternative solution in overcoming the landslide problem in Malang City. Finally, the authors conclude the relevant discussion results based on findings from the literature review. The authors also include a bibliography which contains the literature sources used in this research. The working principle of the geoelectric method is by studying the electrical flow in the earth based on the electrical properties of rocks.

Examples of these properties are specific resistance, conductivity, dielectric constant, and the ability to generate self-electric potential. The way this method works is by inserting an electric current through two current electrodes and measuring the resulting potential distribution using potential electrodes on the earth's surface. The geoelectric method is used in subsurface natural exploration [15]. The tools used in this research include a geoelectric device used to measure rock resistivity at the research location and a GPS system to determine the coordinates of the geoelectric measurement points.

Measurements are carried out with computed direct current to prevent polarization and using a resistivity meter to measure the potential difference. This tool must be used in completely dry conditions to provide accurate results. The use of certain configurations, such as the Wenner configuration, is often applied specifically to analyze resistivity contrast in areas with critical slope inclinations as an initial step to identify potential ground movement [16]. The geoelectric data from the measurement results are used as a reference to determine the landslide point in the data collection area, and information regarding the resistivity value and the stretch length from the geoelectric method can provide a picture of the subsurface conditions [13].

3. RESULT AND DISCUSSION

3.1. Geoelectric Resistivity Data Analysis

In a certain area, if the soil has a rough and loosely bound structure or texture, such as sand and gravel, and contains excessive water that reduces the adhesion between soil grains, then the area can be considered prone to landslides. Based on Table 1, it is known that at a depth of 5.46-8.19 meters there is a clay layer, at 8.19-29.37 meters there is a sand layer, at 63.74-104.10 meters there is a sand layer, and at 104.10-110 meters there is a gravel layer. At a depth of 63.74-104.10 meters, there is groundwater with a resistivity of 95.92 Ωm. This indicates that the first observation location is an area vulnerable to landslides, starting from a depth of 5.46 meters, with the most vulnerable area located at a depth of 63.74-104.10 meters.

Based on Table 2, it is known that at a depth of 11.44-21.86 meters there is a clay layer, at 21.86-33.43 meters there is a sandy silt layer, at 45.76-91.92 meters there is a gravel layer, at 91.92-121.56 meters there is a sand layer, and at 121.56-150 meters there is a gravel layer. At depths of 33.43-45.76 meters and 91.92-121.56 meters, there is groundwater with resistivities of 29.48 Ωm and 93.03 Ωm, respectively. This shows that the second observation location is also a landslide-prone area, starting from a depth of 11.44 meters, with the most vulnerable area located at a depth of 91.92-121.56 meters. Based on the processing results of the subsurface material resistivity cross-section data at the Jatimulyo mini football field, Lowokwaru, Malang City, it can be seen that at a depth of 0-5.179 meters, there is a clay layer with a resistivity value range of 8.859-11.2 Ωm.

At a depth of 5.179-10 meters, there is a sandy clay layer with a resistivity value range of 11.29-12.59 Ωm. At a depth of 10-37.28 meters, there is a sand layer with a resistivity value range of 12.74-15.85 Ωm. At a depth of 11.5-37.28 meters, there is an alluvial layer with a resistivity value range of 16.24-18.33 Ωm. At a depth of 13.89-37.28 meters, there is a rocky sand layer with a resistivity value range of 19-20.69 Ωm.

Furthermore, from the results of the data processing, it can also be seen that each research point has material layers of different lengths and thicknesses. The top layer at each point contains a clay layer with an average thickness of 5.179 meters. The second layer at each point contains a sandy clay layer with an average thickness of 4.821 meters. The third layer at each point contains a sand layer with varying thicknesses at each respective point.

The fourth layer is only found at points 1, 2, and 3 with an average length of about 30 meters and a relatively similar thickness in each layer, which is 25.78 meters. The fifth or bottom layer is found at points 1, 2, and 3 with an average length of 30 meters and varying thicknesses at each point. In relation to landslides, the results of this data processing can be used as a basis to determine locations prone to landslides, especially in material layers with varying thicknesses at each point and in sand layers whose resistivity value range is between 12.74-15.85 Ωm. In addition, an understanding of the stratigraphy of the research area is also important to determine how the distribution and characteristics of subsurface materials can affect slope stability and construction feasibility in the area.

3.2. Landslide Mitigation Strategies

Landslides are natural disasters that can occur in various regions, including Malang City. To overcome this disaster, it is necessary to implement an integrated mitigation strategy. Based on the provided information, there are two landslide-prone sample locations in Malang City, namely the first location at a depth of 5.46 meters and the second location at a depth of 11.44 meters. One of the mitigation strategies to reduce landslide risks in Malang City is the mapping and identification of landslide-prone areas, which can be done using the geoelectric method.

The concept of spatial hazard mapping is an essential pillar in integrated mitigation strategies, and its principles are also widely adopted in mapping other geological disaster vulnerabilities, such as seismic hazard probability and maximum ground acceleration for regional spatial evaluation [17], [18], [19]. This method studies the flow of electricity in the earth based on the electrical properties of rocks, such as specific resistance, conductivity, dielectric constant, and the ability to generate self-electric potential. The results of the geoelectric method can provide an overview of subsurface conditions and can be used as a reference to determine landslide points in the data collection area. Land use control is an effective mitigation strategy to reduce landslide risks, which includes regulating development in landslide-prone areas, managing agricultural land, and regulating human activities in those areas.

Increasing public awareness of landslide hazards is very important in reducing the risk of this disaster. Socialization campaigns that educate the public about landslide hazards, early symptoms of landslides, and how to avoid landslide-prone areas need to be carried out regularly. Infrastructure development, such as HIPPAM networks and business cooperatives, can help reduce the risk of landslides. The HIPPAM (Public Hydrant for Firefighting) network can be used to extinguish fires that appear after a landslide, while business cooperatives can help improve the local community's economy so they can be more financially stable and prepared to face natural disasters.

Structural mitigation is carried out by building structures that can withstand or reduce landslide forces, such as installing fences or retaining walls on landslide-prone slopes. The selection of structural mitigation, such as dredging landslide material or building retaining walls, must be adapted to the type of landslide and slope geometry that has been previously mapped [20]. Non-structural mitigation includes efforts that do not involve building structures, such as training, forming volunteer forums, socialization, and disaster simulations. The implementation of disaster simulations in educational institutions has proven to be very crucial for training psychomotor skills and self-rescue instincts, although its implementation must consider environmental factors and heat stress so that participants' concentration levels remain optimally maintained [21].

The implementation of mitigation strategies, both structural and non-structural, must be carried out in an integrated manner to ensure success in reducing landslide risks. In implementing mitigation strategies, good coordination and cooperation are needed among the government, the community, non-governmental organizations, and other related parties. In addition, periodic evaluation and monitoring also need to be carried out to assess the effectiveness of the mitigation strategies that have been implemented and provide input for future improvements. This evaluation process is highly ideal when combined with statistical data modeling to predict the duration of recovery or the decay of post-disaster alert status, similar to the application of Omori and Mogi statistical models relied upon by mitigation authorities to determine the estimated recovery time of the post-earthquake crisis phase [22].

By applying the right and integrated mitigation strategies, it is hoped that it can reduce the risk of landslides in Malang City and increase community resilience to natural disasters. The geoelectric resistivity method has potential as an alternative solution in overcoming landslide problems in Malang City because it can provide information regarding resistivity values and stretch lengths below the ground surface. This method can help identify landslide-prone areas and determine landslide points in the data collection area. Furthermore, the use of the geoelectric resistivity method can provide accurate results if carried out in completely dry conditions.

However, there are several limitations to the use of the geoelectric resistivity method, the first of which is that it can only measure the electrical properties of rocks and cannot provide information on soil strength and stability. Second, utilizing the geoelectric resistivity method requires fairly expensive equipment and demands specific expertise for its operation. Third, this method also possesses limitations regarding measurement depth, meaning it cannot be utilized to measure the electrical properties of rocks in deeper layers. Therefore, the geoelectric resistivity method must be combined with other methods to acquire more comprehensive information, such as integrating wide-scale non-seismic anomaly extractions like satellite gravity or double-difference relocation methods used as comparisons in applied geophysics [23], [24], [25].

4. CONCLUSION

The geoelectric resistivity method studies the electrical flow in the earth by inserting an electric current through two current electrodes and measuring the resulting potential distribution using potential electrodes on the earth's surface. A geoelectric device is utilized to measure rock resistivity at the research location, and a GPS is used to accurately determine the coordinates of the measurement points. Geoelectric data from the measurement results are then used to determine landslide points in the data collection area and provide a general overview of subsurface conditions. There are several mitigation strategies to reduce landslide risks in Malang City, including mapping and identifying landslide-prone areas, increasing public awareness, infrastructure development, and structural and non-structural mitigation.

The geoelectric resistivity method can be used as an alternative solution in overcoming landslide problems in Malang City, which is in line with modern geophysical studies confirming that electrical resistivity tomography is a reliable instrument for the early identification of slip surfaces within the disaster mitigation framework [26]. This method can provide information regarding resistivity values and subsurface stretch lengths, thereby helping to determine specific landslide points in the data collection area. However, this method has several limitations, such as needing to be carried out in completely dry conditions to provide accurate results, while also requiring quite expensive equipment and specific operational expertise. Therefore, the use of the geoelectric resistivity method must be considered carefully and compared with other methods before being used as an alternative solution in overcoming landslide problems in Malang City.

REFERENCE

[1] D. S. Seruni, M. T. Furqon, and R. C. Wihandika, "Sistem Prediksi Pertumbuhan Jumlah Penduduk Kota Malang menggunakan Metode K-Nearest Neighbor Regression," *J. Pengemb. Teknol. Inf. dan Ilmu Komput.*, vol. 4, no. 4, pp. 1075–1082, 2020, [Online]. Available: http://j-ptiik.ub.ac.id

[2] R. Imandasari, Afifuddin, and H. Anadza, "Efektivitas program pemberdayaan masyarakat miskin melalui kelompok usaha bersama di Kota Malang," *Respon Publik*, vol. 16, no. 4, pp. 63–68, 2022.

[3] M. H. S. Hariyanto, F. Ramdani, and M. C. Saputra, "Sistem Informasi Geografis Kesesuaian Lahan Perumahan di Kota Malang menggunakan Metode MCE," *J. Pengemb. Teknol. Inf. dan Ilmu Komput. Univ. Brawijaya*, vol. 2, no. 1, pp. 263–272, 2018.

[4] Salsabila, T. A. Rachmawati, and F. Usman, "Mitigasi Bencana Tanah Longsor di Kawasan Sempadan Sungai Brantas Pada Kampung Tematik Kota Malang," *Plan. Urban Reg. Environ.*, vol. 10, no. April, pp. 141–148, 2021.

[5] H. Fauzana and E. L. Namigo, "Identifikasi bidang gelincir zona rawan longsor di kawasan wisata Puncak Taruko Kabupaten Agam menggunakan metode geolistrik resistivitas," *J. Fis. Unand*, vol. 13, no. 5, pp. 644–650, 2024, doi: 10.25077/jfu.13.5.644-650.2024.

[6] M. Udin, A. Susilo, and A. M. Juwono, "Studi bidang gelincir sebagai langkah awal mitigasi bencana longsor di Kampung Ledok Kecamatan Sumberpucung Kabupaten Malang menggunakan metode geolistrik konfigurasi dipol-dipol," Brawijaya University.

[7] R. I. Hielmy *et al.*, "Sosialisasi Mitigasi Bencana Gempa Bumi , Tsunami , dan Hidrometeorologi di SMAN 6," *To Maega | J. Pengabdi. Masy.*, vol. 8, no. 3, pp. 607–616, 2025.

[8] A. Nusantoro, "Analisis mitigasi bencana tanah longsor berbasis kearifan lokal di Purworejo," in *The 11th University Research Colloquium 2020*, 2020.

[9] R. I. Hielmy and S. T. Gustono, "Estimation of Jayapura 2023 Aftershock Decay Time Using Python-Based Secant Algorithm," *J. Comput. Phys. Earth Sci.*, vol. 5, no. 2, pp. 180–188, 2026.

[10] R. I. Hielmy, B. Pranata, Wijayanto, and Daryono, "Performance Evaluation of Automated and Manual Seismic Phase Picking for Rapid Earthquake Parameter Determination in the Indonesian BMKG Network," vol. 26, no. 2, pp. 89–107, 2025.

[11] A. Wijaya, "Aplikasi Metode Geolistrik Resistivitas Konfigurasi WennerUntuk Menentukan Struktur Tanah di Halaman Belakang SCC ITS Surabaya," *J. Fis. Indones.*, vol. 19, no. 55, pp. 1–5, 2015.

[12] M. Arif, D. Pujiastuti, and A. F. Pohan, "Pemodelan 3D bidang gelincir tanah longsor menggunakan metode geolistrik di Bukit Nobita Padang," *J. Fis. Unand*, vol. 13, no. 1, pp. 15–21, 2024, doi: 10.25077/jfu.13.1.15-21.2024.

[13] A. A. Darmawan, C. Saleh, E. Setyono, and A. S. Amal, "Analisa Model Struktur Geologi Untuk Menduga Air Tanah Dengan Menggunakan Metode Geolistrik," *J. Ilm. Univ. Batanghari Jambi*, vol. 21, no. 1, p. 289, 2021, doi: 10.33087/jiubj.v21i1.1261.

[14] G. A. Gautama, Y. Firmansah, and L. A. Grestika, "Identifikasi bawah permukaan di lapangan sepakbola mini, Jatimulyo, Lowokwaru, Kota Malang dengan menggunakan metode geolistrik," *J. Qua Tek.*, vol. 12, no. 1, pp. 58–81, 2022.

[15] D. Sedana, A. As'ari, and A. Tanauma, "Pemetaan Akuifer Air Tanah Di Jalan Ringroad Kelurahan Malendeng Dengan Menggunakan Metode Geolistrik Tahanan Jenis," *J. Ilm. Sains*, vol. 15, no. 1, p. 33, 2015, doi: 10.35799/jis.15.1.2015.6778.

[16] S. Ulfah and A. Winardi, "Analisis daerah potensi longsor Kalijaga Selatan menggunakan geolistrik Wenner," *SainsTech Innov. J.*, vol. 8, no. 2, pp. 554–559, 2025.

[17] R. I. Hielmy, "Perbandingan Metode Davenport, Milne, dan McGuirre dalam Penentuan Nilai Percepatan Tanah Maksimum di Pulau Bali," *Bul. Meteorol. Klimatologi, dan Geofis.*, vol. 5, no. 5, pp. 9–16, 2024.

[18] R. I. Hielmy, "Deterministic Seismic Hazard Analysis (DSHA) and Peak Ground Acceleration Mapping in West Java (2018–2024)," *J. Comput. Phys. Earth Sci.*, vol. 5, no. 2, pp. 227–231, 2026.

[19] R. I. Hielmy and M. L. Rajagukguk, "Analisis probabilistik bahaya seismik di denpasar dan sekitarnya berdasarkan pendekatan psha," *J. Online Phys.*, vol. 11, no. 1, pp. 21–28, 2025.

[20] S. Indriati, S. Sultan, and B. Azikin, "Kajian mitigasi pada zona rawan tanah longsor berdasarkan tipe longsoran di Kecamatan Kokalukuna dan Kecamatan Bungi, Kota Baubau Provinsi Sulawesi Tenggara," *J. Ecosolum*, vol. 12, no. 1, pp. 72–85, 2023, doi: 10.20956/ecosolum.v12i1.26732.

[21] R. I. Hielmy *et al.*, "Evaluasi Efektivitas Simulasi Mitigasi Bencana Gempa Bumi di Sekolah An-Nisaa' Izada, Tangerang Selatan," *To Maega | J. Pengabdi. Masy.*, vol. 9, no. 1, pp. 1–12, 2026.

[22] M. L. Rajagukguk and R. I. Hielmy, "Estimating Aftershock Termination Time Using Statistical Decay Models: A Case Study of the March 22, 2024 Bawean Earthquake," *J. Comput. Phys. Earth Sci.*, vol. 5, no. 2, pp. 210–216, 2026.

[23] R. I. Hielmy, "Subsurface Structure of Palu-Koro Fault Zone Using TOPEX Satellite Gravity Data and Regional-Residual Anomaly Separation," *J. Comput. Phys. Earth Sci.*, vol. 5, no. 2, pp. 217–226, 2026.

[24] R. I. Hielmy, "Subsurface Structural Identification and Seismicity Correlation in West Java Using EMAG2 Geomagnetic Data," *J. Comput. Phys. Earth Sci.*, vol. 5, no. 2, pp. 202–209, 2026.

[25] R. I. Hielmy, "Revealing the Subsurface Geometry of the 2023 Sumedang Earthquake Sequence Using Double-Difference Relocation and Cross-Section Analysis," *J. Comput. Phys. Earth Sci.*, vol. 5, no. 2, pp. 173–179, 2026.

[26] A. Tohari, D. D. Wardhana, S. Feranie, and G. A. Salsabila, "Identification of sliding surface using electrical-resistivity tomography for landslide mitigation: A case study of the Cibitung landslide," *IOP Conf. Ser. Earth Environ. Sci.*, vol. 1314, no. 1, p. 12030, 2024, doi: 10.1088/1755-1315/1314/1/012030.